THE CALCIUM PHOSPHATE COATING OF SOY LECITHIN NANOEMULSION

WITH PERFORMANCE IN STABILITY AND AS AN OXYGEN CARRIER

by

Kyu B. Han

A dissertation submitted to the faculty of
The University of Utah
in partial fulfillment of the requirements for the degree of

Doctor of Philosophy

Department of Materials Science and Engineering

The University of Utah

May 2015

The University of Utah Graduate School

STATEMENT OF DISSERTATION APPROVAL

The dissertation of   **Kyu B. Han**

has been approved by the following supervisory committee members:

Agnes Ostafin	, Chair	**11/24/2014**
		Date Approved
Reaz Chaudhuri	, Member	**11/24/2014**
		Date Approved
Ling Zang	, Member	**11/24/2014**
		Date Approved
Ashutosh Tiwari	, Member	**11/24/2014**
		Date Approved
Michael Granger	, Member	**11/24/2014**
		Date Approved

and by   **Feng Liu**   , Chair/Dean of

the Department/College/School of   **Materials Science and Engineering**

and by David B. Kieda, Dean of The Graduate School.

ABSTRACT

This work studied the relationship between surfactant, oil, and water, by building ternary phase diagrams, the goal of which was to identify the oil-in-water phase composition. The resulting nano-sized emulsion was coated with dicalcium phosphate by utilizing the ionic affinity between calcium ions and the emulsion surface. Since the desired function of the particle is as an oxygen carrier, the particle stability, oxygen capacity, and oxygen release rate were investigated. The first step in the process was to construct ternary phase diagrams with 1,2-dioleoyl-sn-glycero-3-phosphate (DOPA) and soy derived lecithin. The results showed that the lecithin surfactant formed an oil-in-water phase region that was 36 times greater than that of DOPA. With the desired phase composition set, the lecithin emulsion was extruded, resulting in a well-dispersed nanosized particle. A pH titration study of the emulsion found an optimized calcium phosphate coating condition at pH 8.8, at which, the calcium ion had a greater affinity for the emulsion surface than phosphate. A Hill plot was used to show calcium cooperativeness on the emulsion surface which suggested one calcium ion binds to one lecithin molecule. The lecithin emulsion particles were then coated with calcium phosphate using a layering technique that allowed for careful control of the coating thickness. The overall particle hydrodynamic radius was consistent with the growth of the calcium phosphate coating, from 8 nm to 28 nm. This observation was further supported with cryo-TEM measurements. The stability of the coated emulsion was tested

in conditions that simulate practical thermal, physical, and time-dependent conditions. Throughout the tests, the coated emulsion exhibited a constant mono-dispersed particle size, while the uncoated emulsion size fluctuated greatly and exhibited increased polydispersion. The fast mixing method with the stopped-flow apparatus was employed to test the product as an oxygen carrier, and it was shown that particles with thicker calcium phosphate coatings released smaller amounts of oxygen in a given timeframe.

This study proved the hypothesis by showing a fundamental understanding of emulsion science, coating the flexible emulsion surface with a biocompatible material, and a strong particle performance with regard to stability and as an oxygen carrier.

TABLE OF CONTENTS

LIST OF TABLES

LIST OF FIGURES

ACKNOWLEDGEMENTS

Even though the following dissertation is an individual work, I could never have reached this height, or explored the depths of the work without the help, support, guidance, and efforts of many other people. First of all, I would like to deeply thank my advisor, Dr. Agnes Ostafin, who always supports me as a great mentor and academic advisor. She has instilled, in me, the necessary qualities for being a good scientist and engineer. Her passion as an educator, and researcher, has been a major motivation through my graduate career at the University of Utah. I would also like to express my appreciation to Dr. Hiroshi Mizukami for his guidance over the years. I also would like to thank to my committee members, Dr. Eyring, Dr. Tiwari, Dr. Chardri, Dr. Zang, and Dr. Mike Granger. Especially Dr. Eyring, who has provided great advice as someone who has had a very accomplished life and career. Curtis Takagi is not only my great friend, but also a colleague at work. I would also like to thank Jerry Wu, Max Chen, and Michael Batenjany as great colleagues. Also, I would like to take this opportunity to thank all my teachers at Gilmour Academy and the University of Utah.

Finally, a very special thank you to my grandmother and parents. Without their support, I could not accomplish what I have. They always showed me the true worth of hard work. I maintained confidence in my abilities, and my future, with the advice of my dad, Sung-Shin Han. My mom, Mi-Soo Chung, has always shown strong faith in me. My thanks also go out to my older brother, Joon-Bum Han, who showed me what genuine courage is in life.

CHAPTER 1

INTRODUCTION

1.1 Overview

Blood donations have been declining, while the need for blood has been increasing. The amount of donations has been decreasing annually by 3 percent, but the demand is growing by 6 percent [1]. This shortage is due, in part, to the greater number of complex therapies such as chemotherapy, organ transplants, and heart surgeries, which require large amounts of blood and blood products[1].

In order to increase the stability from the current perfluorocarbon-based oxygen carrier while maintaining the function as an oxygen delivery, this study investigated the use of a calcium phosphate (brushite, $CaHPO_4$) surface encapsulation of an oil-in-water emulsion and how it may improve the stability of the blood substitute without changing its function as an oxygen carrier. This theory hinges on the idea that the rigid surface of nanoemulsion will remain constant, regardless of any external force applied, while the porous brushite will allow for the diffusion of oxygen molecules.

In order to achieve this goal, this study focused on finding the desired phase of emulsion by constructing a ternary phase diagram. Then, the emulsion was coated with calcium phosphate. Finally, this study tested the stability and oxygen release from the coated emulsion.

<u>1.2 Background of Oxygen Carrier as a Blood Substitute</u>

Blood substitutes are designed to fulfill particular functions normally performed by red blood cells (RBC). One of these functions is the delivery of oxygen. The history of blood transfusion and the development of red blood substitutes has been complementary. William Harvey theoretically described the circulation of blood in 1628 [2]. Blood transfusions were first practiced in 1665 from one animal to another by Richard Lower and Edward King [3]; they used the quills of bird feathers to puncture arteries and blood was collected in an animal bladder. The first blood substitute was a cow's milk (1878), used in the case of Asiatic cholera because the milk was thought to regenerate white blood cells [2, 4], but when the milk was injected into two patients, they died after a few hours. Since 1628, scientists have studied blood substitutes in search of a product suitable for the human body (Figure 1-1). There have been two predominant methods for the oxygen carrier, cell-free hemoglobin and perfluorocarbon-based. The literature review will focus on these two materials (see Table 1-1).

1.2.1 Hemoglobin-based Oxygen Carrier (HbOC)

Hemoglobin is the metalloprotein found in the red blood cells that transports oxygen and carbon dioxide between the lungs and the rest of the body. Hemoglobin's oxygen-binding capacity is 1.34 mL of oxygen per gram [5] and because hemoglobin is a natural oxygen carrier and purifier that can be directly extracted from red blood cells, it was the first product to be used as a blood substitute oxygen carrier [6].

The first hemoglobin-based blood substitute caused side effects such as hypertension, bradycardia, oliguria, and anaphylaxis [7]. Even though the product was modified by identifying and eliminating the rapid breakdown of methemoglobin, the

hemoglobin-based substitute still had extremely high levels of toxicity in the kidney because the kidney was not able to filter the formed dimers in the crosslinked hemoglobin [8]. Hemoglobin has a high affinity for binding oxygen, which prevented the cell-free hemoglobin from releasing all of its oxygen into the tissues. In order to solve this problem, the affinity of the hemoglobin was reduced by modifying and increasing the stability of its tetrameric structure, extending the vascular retention by applying the agent pyridoxal 5'-phosphate (PLP) [9, 10]. Later, by removing stroma from red cell hemolysates, the hemoglobin study was expanded to a larger scale for experimental use and human trials [11-22]; however, there were many failures during the trials.

Another approach to preventing toxic side effects of the cell-free hemoglobin was to encapsulate it within a liposome, simulating the hemoglobin in a red blood cell. This encapsulation mimicked the structure of a red blood cell as the hemoglobin was packed inside a membrane. This approach seemed to solve the existing problems, but caused other problems such as reticuloendothelial, macrophage stimulation, difficulty in maintaing sterility, endotoxin contamination, cumbersome production, and high cost [23-27].

1.2.2 Perfluorocarbon-based Oxygen Carriers (PFBOC)

In 1966, Clark and Gollen made perfluorocarbon well known by immersing a laboratory mouse in butyltetrahydrofuran (FC-80) [3]. The mouse survived in the solution for two hours. This chemical is inert, similar to Teflon, and insoluble in water, so a large proportion of oxygen can be dissolved in solution – around 38-50 vol.% at 37°C [28]. A perfluorocarbon solution was added to emulsifier, so it would become soluble in water

[29]. The water-soluble emulsion was then tested in the blood of rats; the results showed that the animals could survive in an atmosphere of 90-100% oxygen [29, 30].

Currently, many developers have been concentrating on this emulsion form, using a high concentration of dissolved oxygen. Fluosol-DA (Green Cross Co., Japan), for example, contained a 20 wt.% perfluorocarbon emulsion [28]. However, the efficacy of the emulsion in current research is limited by its low stability, making it difficult to package as it easily flocculates and coalesces during the process.

PFBOCs have one unique benefit compared to HbOCs: the predictable side effects. Because HbOCs are based on a biological material, their side effects are sometimes difficult to anticipate when they are injected into the blood. Since PFBOCs are synthetic, they yield more predictable reactions when applied both *in vivo* and *in vitro*. However, toxicity problems and unstable emulsifiers still cause problems for clinical trials. Systematic optimization of stability and function is needed to overcome these problems.

Researchers have tried to improve the stability of PFBOCs by adding small amounts of co-surfactants, but they have struggled to achieve acceptable stability and functionality [31-34]. There are two problems. The first is the method used to construct the ternary phase diagrams, of perfluorocarbon solutions, constructed objectively with visual observations rather than by specific characterizations. Typically, studies have constructed the diagrams by observing the phase separation with visual cues, which led to inconsistencies. The diagrams with perfluorocarbon solution demonstrated Winsor Type I and II [35-38] phase characteristics; the Winsor system differentiates phase behavior when oil, water, and surfactant form an emulsion (a more detailed background on Winsor systems can be found in section 1.3.2.2). In other works, the lack of a consistent

classification method makes it insufficient to specify Winsor system [35-38]. Another problem is the methodology used to measure oxygen in PFBOCs. Currently, oxygen is measured by transferring oxygen from the purged oxygen gas to the PFBOC. This procedure requires the researcher to make many assumptions in order to estimate the oxygen content, which affects the accuracy of the measurement.

1.3 Development of a Ternary Phase Diagram for Oil/Water/Surfactant

1.3.1 Significance of Developing the Ternary Phase Diagram

The ternary phase diagram is a compositional map of three different materials. This map is an empirically developed depiction of the possible forms a three-component mixture may have. Figure 1-2 shows a typical ternary phase diagram of oil/water/surfactant. Generally, when the amount of surfactant comprises the majority of the emulsion solution, it forms a liquid crystal, as shown in the right corner of Figure 1-2. The normal micelle is formed at the corner of water and surfactant, while the reverse micelle is typically found at the corner of oil and surfactant in the ternary diagram. The emulsion, which forms a spherical shape of a certain size range, is called a microemulsion and usually requires a small amount of surfactant. If the region of the microemulsion is close to mostly water, it is an oil-in-water emulsion. If the region is close to mostly oil, it is a water-in-oil emulsion. The rest of the regions are complicated by the fact that various structures and phases coexist, and therefore it is difficult to distinctly classify [39-41].

The conditions under which the microemulsion forms can be altered by the type of surfactant, as well as experimental conditions such as pressure, temperature, pH, and the presence of a counter ion. The regions at the corners of the ternary diagram are generally less sensitive to the type of surfactant and conditions, whereas the rest of the regions are

more unpredictable. Therefore, it is difficult to theoretically predict the stability of a microemulsion using the ternary phase diagram. It is relatively easy to construct the diagram empirically using a titration method or combining the components in various amounts to make the samples.

1.3.2 Review of the Foundational Concepts Guiding the Diagram

1.3.2.1 Phase Rule

It is important to refer to the phase rule in order to understand the fundamental principle of the ternary phase diagram. Generally, the rule represents the anticipated phase with a given number of components. The rule is expressed as follows:

$$P = C + 2 - F$$

<div align="right">Eq. 1-1</div>

where P is the number of phases at equilibrium, C is the number of components, and F is the number of degrees of freedom (DOF). If using three components for the emulsion system, F can include up to four variables: temperature, pressure, and two chemical potentials, which are independent of composition. For example, all four DOF variables should be fixed to obtain a single phase (P = 1), and only one of the three compositions is free to obtain two phases (P = 2) at constant temperature and pressure.

The ternary phase diagram is a visual representation of the phase rule. Typical diagrams should be constructed at constant temperature and pressure to prevent phase discrepancies that can arise due to changes in these variables. The ternary phase diagram presents the phase behavior of oil/water/surfactant at equilibrium with a reduction in Gibb's free energy (G < 0). The Winsor system presents the relationship between phase behavior and the different components of the oil/water/surfactant.

1.3.2.2 Winsor System

The ternary phase diagram is utilized to recognize the types of phases by exploring the possible combinations of the three added materials. In order to construct the diagram, the Winsor system classifies the phases [42] into three different types (I, II, and III) based on visual observation (Figure 1-3). The Winsor system is also related to the distribution of phase regions in the diagram. Winsor Type I and II are identical in the diagram, but visual observation reveals the difference between the two by the separation of excess liquid. The Winsor system has been in use for about 60 years, and it is still an excellent method that quickly constructs ternary phase diagrams.

The additional methodology used to circumvent the subjective nature of the Winsor system is the shear stress and strain of the emulsion system [43] using the property of a colloid suspension. The surface tension of a colloid changes depending on the rheological behavior because the phase change is related to viscosity and surface tension. This method allows for a better understanding of the phase behavior change and a more accurate map of the ternary phase diagram.

Even though these methods have been utilized to construct ternary phase diagrams, additional measurements are still needed to distinguish between subphases. The additional methodologies utilized buoyant density, fluorescence quenching, Fourier transform infrared spectroscopy, and cryogenic transmission electron microscopy [44-47]. These methodologies helped to determine the emulsion phase behavior by further characterizing its chemical behavior.

1.3.3 Review Formulation for Oil-in-water Emulsion

1.3.3.1 Micelle

It is important to review the differences between the micelle and the emulsion in order to understand the ternary phase diagram. The difference is that the micelle has a smaller size. The micelle structure is determined by the self-assembly of the surfactant, which has a hydrophilic head group and a hydrophobic tail. It can also have various sizes of head groups and lengths of tail lengths. The micelle structure is estimated by the surfactant packing parameter (g) as follows [48]:

$$g = \frac{v}{a_0 l}$$ Eq. 1-2

where v is the volume of hydrocarbon chain, a_0 is the area of the head group, and l is the length of the hydrocarbon chain of the surfactant monomer. The value of g determines which micelle structure is more likely to form. If the value is equal to or less than 1/3, for example, the surfactant would form a spherical micelle. If the value is between 1/3 and 1/2, it is more likely that a rod-like micelle will be formed. If the value of g equals 1, the micelle structure is most likely a bilayer. If it is greater than 1, the micelle forms in reverse (Figure 1-4).

1.3.3.2 Microemulsion

It is also important to clarify the classification of spherical emulsions according to their size: micelle (< 50 nm), microemulsion (from 50 nm to 3 μm), and macroemulsion (> 3 μm) [43]. This study focuses on microemulsion because it has previously been used as an oxygen carrier. Negative side effects have occurred when the emulsion particle size is too large (a micron), so emulsions for oxygen carriers are generally synthesized at a

size smaller than 1 um in diameter [26]. Even though microemulsions seem to have similar structures to micelles, they differ in the size of their particles, and have large liquid cores filled with either oil or water.

Due to the difference in size, the packing parameter in microemulsions also changes the curvature of the particle's surface. A microemulsion demonstrates a small degree of polydispersity, even though the majority consists of micron-sized particles. This small degree of polydispersity phenomenon results from a microemulsion built by the micelle-swelling mechanism [49], which eventually influences the packing parameter. Instead of four different classifications of the packing parameter, microemulsions only have three. When the value of g is less than 1, microemulsions can easily form oil-in-water. When g is greater than 1, the emulsion favored is a water-in-oil emulsion. When g is equal to 1, the emulsion forms a bicontinuous microemulsion (Figure 1-5).

1.3.3.3 Influence of Charged Surfactants on the Formulation

The head groups of surfactants can be classified into anionic, cationic, nonionic, and zwitterionic. Anionic heads and cationic heads indicate negatively and positively charged groups, respectively. Examples of these groups include sodium dodecylsulfate (SDS), an anionic surfactant, and cetyltrimethylammonium bromide (CTAB), a cationic surfactant. Nonionic head groups do not contain a charge, for example, Triton X-100. Zwitterionic heads have both negatively and positively charged groups; an example is L-α-phosphatidylcholine (soy lecithin), as shown in Table 1-2.

As described above, a_o, v, and l values of the surfactants are used to estimate the most probable micelle structure. It is not only the structure of the surfactants that determines the packing parameter, but also the ionic charge of head group. The ionic

charge's influence is due to the balancing between the repulsive and attractive forces of the surfactants during self-assembly. For example, anion or cation surfactants have strong repulsive forces between the head groups, causing greater separation between them. If a_o becomes greater than the structural estimation due to the repulsive force, the packing parameter is reduced, so it is possible for surfactants with an ionically charged head group to form spheres. However, because a repulsive force increases a_o, fewer surfactant molecules are required to form an emulsion or micelle than without that force. As a result, the region of oil-in-water in the ternary phase diagram will be smaller than the surfactant without a repulsive force such as soy lecithin.

1.3.3.4 Instability of the Emulsion

Synthesizing a well-dispersed emulsion system is essential for improving the stability of the emulsion. Once the emulsion particles are broken down, there can be creaming, sedimentation, flocculation, Ostwald ripening, coalescence, and phase inversion (Figure 1-6), which all contribute to lowered stability [50]. Flocculation is the aggregation of the particles without any change in their initial size. The process is governed by the van der Waals attraction force, which is found in all colloid systems. If the repulsive force is weaker than the attractive force, the particles flocculate.

Coalescence is the process that thins and disrupts the liquid film between particles. The result is two or more particles that fuse together to form a larger particle, which can only occur when the particles are closely packed. This can happen naturally via flocculation, or with an external force like centrifugation.

Phase inversion indicates a phase exchange between the continuous and the dispersion phases. This occurs when various types of emulsions coexist in the solution,

and Ostwald ripening generally manifests itself over time. The emulsion system is, generally, a polydisperse system with smaller and larger sized particles. The small particles are fairly evenly dispersed throughout the suspension as compared to the large particles. The small particles, however, diffuse between large particles, becoming the bulk. This phenomenon happens naturally, and over time a more thermodynamically stable condition is reached with a minimized surface to area ratio.

1.3.4 Technical Challenges of Constructing the Ternary Phase Diagram

Constructing the ternary phase diagram is critical to the mapping of the possible emulsion phases in a given set of experimental conditions. Visual inspection is commonly used in this methodology along with shear stress testing and cryogenic transmission electron microscopy. These techniques aim to further define the phase boundaries and the molecular structures of the different phases. This section discusses the methodologies used for constructing the diagram.

1.3.4.1 Current Methods for Constructing Ternary Phase Diagrams

1.3.4.1.1 Visual Inspection

Generally, the phase boundaries in the ternary diagram are determined using visual inspection [37, 39-41, 51-53]. It is fast and easy, but it is the least accurate method because it is subjective. Still, visual observation is essential for developing the general diagram. Other tools are needed to subdivide the general diagram into more defined regions such as contiguous particle size, morphology, dispersion of particle, and emulsifier concentration because the stability behavior of the emulsion system is sensitive to these.

1.3.4.1.2 Shear Stress and Strain

There may be ranges of particle size, morphology, dispersion of particle, and emulsifier concentration that yield functionally and physically identical material. The challenge is to find regions in the phase diagram that have significant differences in behavior, not just size, morphology or dispersion. In this work, phase boundaries are determined by monitoring the change of fluid behavior. The emulsion system's overall properties are strongly determined by its rheological properties, and they often have unique stress and strain characteristics. Newtonian fluid presents a linear relationship between shear stress and strain, while non-Newtonian fluids do not. For example, the low viscosity of an emulsion system generally implies that the emulsion particles are well dispersed in the solution [34, 54]. However, when the emulsion system is complex, containing a bicontinuous phase and emulsion particles, it transforms into a non-Newtonian fluid and the viscosity changes with applied stress and strain [55, 56]. Increasing emulsifier, the interfacial film strength increases. This implies an increase in the viscosity of oil and water. The viscosity of the whole system is dependent on interfacial viscosity. The adsorption of surfactants immobilizes the surface. When particles are small in a concentrated system, tangential shear stresses are opposed by surface tension gradients.

1.3.4.1.3 Transmission Electron Microscopy (TEM)

TEM provides a direct picture of the emulsion characteristics but is susceptible to variations in specimen preparation and drying [43, 54, 57]. The fundamental mechanism of TEM is similar to optical microscopy, but the incident source in TEM is an electron beam transmitted through a thin specimen, while in optical microscopy it is light. In TEM,

as the beam is imaged onto a fluorescence screen, the degree of transmittance differs with the crystal face and defects of the specimen. However, due to the high vacuum and high-accelerated voltage, TEM requires either special sample preparation, such as cryogenic temperature, or the negative staining of the emulsion.

Cryogenic transmission electron microscopy (cryo-TEM) is a useful technique for emulsion samples that are fragile under TEM conditions (electron beam and high vacuum). Instead, cryo-TEM studies the samples at cryogenic temperatures, providing high-quality images with powerful magnification showing surface features and shape. Even though it is an expensive technique and the sample preparation is a delicate procedure, cryo-TEM is still used extensively to characterize and understand the morphology of emulsion systems.

The technique of negatively staining samples is also effective for emulsion samples, especially since the sample preparation is easy and fast. Negative stains are ammonium molybdate, uranyl acetate, uranyl formate, osmium ferricyanide, and phosphotungstic acid. These materials scatter electrons efficiently, while absorbing emulsion and biological samples. However, the disadvantage of this technique is that the preparation does not allow for high resolution or structural artifacts to be included in the image.

1.3.4.2 Potential Methods for Constructing Ternary Phase Diagram

1.3.4.2.1 Buoyant Density

The density is the value of mass per volume. Generally, solid forms have a high density because the molecules are tightly organized. In liquid, the distance between molecules is relatively greater than in solids. Therefore, molecules in liquid form take up

more volume than they would in solid form. Gas takes up an even greater volume than liquid, meaning that the density of gas is the lowest, and because the density is related to the dispersion of molecules, it is also related to temperature and viscosity. Buoyancy is the force created by the displacement of fluid, for example, a bubble rising to the surface. It is the force that helps prevent the particles from sedimenting.

Archimedes' principle is used to measure buoyancy density. Generally, an insoluble powder is added to a known volume of liquid. The density of the product, including the solvent and the powder, is then measured by using a pycnometer. This principle was applied to a powdered emulsion sample that showed emulsions with the high-density oil were heavier than those without the oil [58].

1.3.4.2.2 Fluorescence Quenching

Fluorescence quenching is the process of decreased fluorescence intensity due to molecular interactions such as excited-state reaction, molecular rearrangement, energy transfer, and collisional quenching. The most common interaction is collisional quenching, which requires the fluorescent molecule to come in contact with the quencher during the excited state. In this process, the fluorescence returns to the ground state without emission of a photon; collisional quenching is described by the Stern-Volmer equation [59]:

$$\frac{F_0}{F} = 1 + K_D[Q] \hspace{3cm} \text{Eq. 1-3}$$

where F_0 and F are the fluorescence intensities before and after quenching, K_D is the Stern-Volmer quenching constant, and $[Q]$ is the concentration of quencher. K_D can be

15

described by biomolecular quenching constant (k_q) and lifetime of fluorophore (τ_0); $K_D = k_q \times \tau_0$.

Pyrene ($C_{16}H_{10}$) is one of the fluorescence probe molecules that is widely used in biological applications [60]. It is not only easily obtained commercially, but has a high quantum yield and lifetime [61]. The fluorescence emission is sensitive to solvent polarity, and potassium iodide (KI) is commonly used as a quencher [60]. In collisional quenching, the excited fluorophore such as pyrene comes into contact with a molecule such as KI, easing nonradiative transitions to the ground state.

Using this mechanism, fluorescence dye molecules can be employed to understand the types of emulsion phases such as oil-in-water, water-in-oil, and bicontinuous. If the quencher is selected carefully, as only being soluble in water, the fluorescent intensity can differ between the various phases. If the dye molecules, dissolved in oil, are encapsulated inside the emulsion particles, the membrane protects the molecules from the quencher.

1.3.4.2.3 Fourier Transform Infrared Spectroscopy (FT-IR)

FT-IR makes it possible to obtain the infrared spectrum of absorption of a solid, liquid, and gas from the bond vibration. The intensity of an absorption band relies on the changes in the dipole moment of the bond due to the bond length and charge difference between two atoms. The molecule absorbs specific frequencies, which are characteristics of the structure. The frequency of the absorbed radiation matches the transition energy of the bond that vibrates [62]. As a result, their unique vibrations can identify molecules. Since the dipole moment is related to the bond distance, the relationship is expressed as follows [63]:

$$\frac{\partial \mu}{\partial x} \neq 0 \qquad\qquad\qquad \text{Eq. 1-4}$$

where $\partial\mu$ is the change in dipole moment, and ∂x is the change in bond distance. In order for absorption to occur, Eq. 1-4 should be nonzero since infrared spectroscopy (IR) monitors the change in energy after emitting a photon to the molecule.

There are two factors that affect the absorption intensity: 1) the molecule and 2) the concentration of molecules. Eq. 1-4 calculates the first factor, so that each molecule has its own absorption. The second factor is based on Beer's law [63]. The molar absorptivity is a constant value, only depending on $(\partial\mu/\partial x)^2$. Therefore, the absorption and the concentration should be balanced by maintaining the absorptivity as a constant. Beer's law is as follows:

$$A = \varepsilon l c \qquad\qquad\qquad \text{Eq. 1-5}$$

where A is the absorption intensity, ε is the absorptivity, l is the path length, and c is the concentration of molecule.

Attenuated total reflectance (ATR) is a commonly used sampling technique in infrared spectroscopy (IR). The incident light undergoes multiple internal reflections in diamond, which creates an evanescent wave that interacts with the sample up to 2 um. A spectrum is recorded with the least amount of effort in sample preparation. Such cells are utilized in various applications related to soft matter material, liquid, powder, and polymer film. The presence of oil can be quantitatively estimated by using Beer's Law.

1.3 Sizing of the Oil-in-water Emulsion

1.3.1 Manufacturing Challenge for Emulsions

The size of the particles is a critical factor in their dispersion. When the particle size is small, ranging between 0.05 and 0.3 um, the emulsion is stable up to a year [64, 65]. Prior research classified emulsions based on their size, micelle (< 50 nm), microemulsion (from 50 nm to 3 um), and macroemulsion (> 3 um) [43]. However, researchers who explore the field of emulsion have easily confused the definitions of microemulsion and nanoemulsion. Since the particle size of nanoemulsion is described as roughly below 200 nm, the word choice obscures the definition. Mainly, there are two factors that determine the difference between nanoemulsion and microemulsion in morphology and stability. First, the spherical structure of a nanoemulsion distinguishes it from a microemulsion. The nanoemulsion is formed by mechanical shear stress, such as ultrasonication, while the microemulsion is formed by self-assembly. Second, the emulsions differ in their stability because they are shaped by distinctive processes; the nanoemulsion is metastable, but the microemulsion is in a steady-state [66]. Even though both of the emulsions consist of oil, water, and surfactants, thermodynamics influences the state of nanoemulsions more efficiently. In general, steady-state microemulsions have low surface tension due to self-assembly, but the metastable nanoemulsion has a relatively high surface tension between the oil and water phases, and the surfactant is mostly soluble only in a continuous phase, not in a dispersed phase. Due to these differences, previous patents of microemulsions are reviewed here in order to improve upon the method for synthesizing nanoemulsions. This review is categorized into three general methods of nanoemulsion synthesis: high external shear stress, ultrasonic agitation, and cyclic phase inversion temperature.

Applied shear stress is one method to manufacture a nanoscale ($<1\mu$m) emulsion system. A Newtonian fluid presents a linear relation between shear rate and viscosity. The viscosity of distilled water is 0.68 cP at 37 °C and the viscosity of olive oil is 43.3 cP. The shear rate of olive oil is about 63 times lower than that of water, and with the reduced shear rate, it is possible to break down a microemulsion into the nanoscale using a common blender. However, one of the common methods for breaking down the microemulsion has been high-pressure homogenization. Pressure is applied at 100 psi, but a piston amplifies it to nearly 30,000 psi in the sample chamber [67]. The process simply applied high pressure to a three-component mixture forced through a carefully chosen microchannel. The extreme shear flow creates a uniform particle size and has been widely used for highly viscous emulsions [68, 69]. Generally, the procedure recirculates several times in order to obtain a homogenous product. The advantage of this technique is that a high volume of emulsions can be produced with a tightly distributed particle size using high shear rates.

A second method for producing nanoemulsions is the ultrasonic agitation of a premixed microscale emulsion [70]. The main principle is to utilize ultrasonic frequencies (~20 kHz or higher) to rupture the microemulsion with extremely high shear [57, 71, 72]. For example, the emulsifier solution is sonicated for 30 seconds at a frequency of 20 kHz, amplitude of 40 %, and a duty cycle of 0.5 % in order to disperse the surfactants [73]. The advantage of this method is that it is a simple method with a short processing time. This technique is widely used in nanotechnology for dispersing nanoparticles in a liquid medium. The disadvantage of this method is that it does not provide a uniform size distribution. In order to overcome this shortcoming, the emulsion solution should be re-circulated many times, but this ends up taking more time than the homogenization.

The last method is temperature inversion, which is simply heating the sample to a high temperature followed by rapid cooling. Shinoda and Ogawa, and Saito and Shinoda demonstrated the concept of phase inversion temperature (PIT) with the solubilization of nonionic emulsifiers or surfactants [31, 74]. The PIT caused the emulsifiers in oil-in-water systems to change their preferential solubility from water to oil. When the temperature was near the PIT, the structure of the surfactant phase was composed of lamellae due to highly reinforced solubilization [74]. In other words, the surfactant formed a continuous structure at the PIT. When temperatures were cycled by lower and higher than the PIT, the amounts of surfactant were minimized to acquire the isotropic solution [74]. The phenomena confuse the emulsion systems as they change between two different metastable states. Then, shear stress is applied to rupture the micron size particles into smaller emulsion. The advantage of this method is the uniqueness of the particle dispersion. The disadvantages are that the procedure requires a high working temperature, increasing the risk of the operation, and a broader size distribution than high pressure homogenization. Due to the cycle of the extreme temperature change, the operation should be extended in order to achieve the desired size.

In short, high-pressure homogenization, sonication, and phase inversion temperature were reviewed as methods to fabricate nanoemulsions. The properties of the two immiscible solutions determine which one of these methods would be most efficient. If there is little density difference between the two solutions (soybean oil and water), then all three methods are recommended. However, if there is a large density difference, like that between perfluorocarbon and water, then the extreme shear stress method is recommended because high Laplace pressure makes it thermodynamically difficult to rupture emulsions. The focus of this review is on the different ways particles can be

fabricated when using immiscible liquids with a large density gap. The larger the density gap, the more difficult it is to obtain a narrow size distribution due to the equilibrium of Laplace pressure. In order to solve this difficulty, an adequate combination of emulsifier assists in preventing the growth, and coalescence of droplets. Once the three components (oil, water, and emulsifier) are mixed sufficiently to enable the manufacturing of micro-scale droplets, it only takes a little more energy to break them down into a nanosized particle.

1.4.2 Theory of Extrusion

During extrusion the size of vesicles is reduced by passing them through a filter membrane with a known pore size. As the emulsion system flows through the membrane, the particles are constricted down to a value near the pore size of the membrane. The flow rate can be described by Darcy's law [75]:

$$\eta Q = K\left(\frac{\Delta P}{\Delta L}\right) \qquad\qquad \text{Eq. 1-6}$$

where ηQ is the viscosity-corrected flow rate independent of temperature, K is the permeability of the filter, and ΔL and ΔP are the length and the pressure difference between the ends of the channel, respectively. The formation of vesicles by extrusion is described in Figure 1-7. If one of the pores in the extrusion membrane is treated like a capillary, the liquid phase will form a cylinder with dimensions equal to the diameter of the pore and width of the membrane. When it reaches the ends of the pore, the phase is randomly broken up. If a surfactant is added to this system, however, the cylindrical structure formed within the pore pinches off into droplets as it exists, due to perturbation

within the stream. This is mainly caused by the lowered surface tension from the emulsifier, a theory which is based on Plateau-Rayleigh instability [76]. Besides the components such as concentration of salt, surfactant, oil, and water, the applied pressure also plays a role in sizing the particle, and it should be constant in order to obtain uniformity within the system.

1.5 Design of Surface Coating on the Emulsion Particle

1.5.1 Significance of the Surface Coating

Various materials have been used to coat the surface of particles such as noble metal cored silica [77-80], iron oxide cored silica [81, 82], metal cored polymer [83, 84], and liposome template silica [85-88]. The purpose of coating these particles is mainly to protect the body from the encapsulated material, however, the primary function of the coating on the emulsion particle is to provide stability.

The first advantage of coating the surface is the prevention of structural changes. Since the emulsion is in a metastable state, it is sensitive to temperature, pressure, and time. Eventually, the emulsion will be applied *in vivo* as an oxygen carrier, so it must be locked into a stable state to prevent any undesired side effect as evidenced by the many emulsion products that still struggle to make the particles stable in blood vessels [89-94]. Secondly, the surface coating should allow the particle to function as an oxygen carrier, even after coating it with a rigid material. The surface coating should not interrupt the particle's original function as an oxygen carrier while it protects the core from unwanted interactions.

1.5.2 Review of Current Surface Coatings on Nanoparticles

1.5.2.1 Properties of Silica as a Surface Coating

Silica has long been utilized as a coating on solid core particles in chemical and biological applications because the reactions on the surface can be easily characterized and the particle is electrostatically stable in an aqueous solution [95-97]. The pH plays an essential role in silica. If the pH is acidic, silica tends to fuse together and becomes a gel. If the pH is basic, the particles separate from each other by yielding to the negative surface charge. Additionally, silica resists biodegradation and is only dissolved in a strong base. Silica also has the porosity for reactants to diffuse in and out when it is utilized for the surface coating. These properties have made silica useful in many applications [98-100], as a biomarker by protecting the fluorescence molecules inside of the particles [101, 102], and for drug delivery using the same mechanism as the biomarkers [103-107]. However, where silica falls short, is when biodegradability is desired; if this is the case then silica should not be used, as it is not readily biodegradable.

1.5.2.2 Properties of Polymer as a Surface Coating

Several popular polymers used for surface coatings are latex, polystyrene, polyanaline, polypyrrole, and polymethylmethacrylate [32, 108-113]. These polymers act similarly to lipids and are easily adaptable to liposomes, bilayer structures that have the same phase on the inside and outside of the barrier. They are often used to as drug delivery vehicles for water soluble drugs due to the stability a bilayer offers [114, 115]. Examples of other types of polymeric material are polyethylene glycol, polypropylene glycol, polyacrylic acid, polycopralactone, and cellulose acetate. These are biodegradable and are better situated to deliver hydrophobic drugs. However, the disadvantages of these

materials are that some require an unfriendly organic solvent during fabrication, and it is possible to cause damage to the drug and surrounding tissues.

1.5.2.3 Surface Coating for the Emulsion using Silica and Polymers

An emulsion is beneficial for drug delivery since its core can be either hydrophobic or hydrophilic. By synthesizing the oil-in-water emulsion with a hydrophobic core, drugs normally insoluble in the body can be dissolved in the core and loaded into the body until they reach their destination. In order to have long-term stability *in vivo*, the previous studies showed silica and polymers have been used to coat the surface. Nonetheless, using these materials for the surface coating of the emulsion should be avoided due to the disadvantages described in the previous sections.

1.5.3 Coating Material and Principles in This Work

1.5.3.1 Significance of Calcium Phosphate as the Coating Material

Calcium phosphate is a suitable coating in this application because 1) it is biocompatible, 2) has good fracture toughness, and 3) is porous. Calcium phosphate (CaP) is biocompatible because human bone consists of a very similar material. CaP is also biodegradable, eventually succumbing to physicochemical dissolution. The fracture toughness of CaP is as strong as human bone (1.2 MPa $m^{1/2}$), which greatly improves its stability properties [116]. The final advantage is its porosity, which varies according to the crystalline structure. For example, hydroxyapatite (HAp) generally has high porosity (65-77%), while tricalcium phosphate has 60-65% porosity, and dicalcium phosphate has about 50% [117]. Porosity is important for drug delivery and release because these are the channels that allow the drug to be released into the body.

1.5.3.2 Dicalcium Phosphate for the Surface Coating Material

Calcium-based ceramic materials have been utilized in biological applications because of their biocompatibility and biodegradability. Calcium phosphate, in particular, is the material that forms and maintains human bone and teeth. It can exist in several different solid phases, depending on the molar ratio between calcium and phosphate (Table 1-3). One of these structures is dicalcium phosphate (DCPA, $CaHPO_4$), known as brushite, which is produced by mixing calcium chloride ($CaCl_2$) and phosphoric acid (H_3PO_4) [118]. The molar ratio between calcium and phosphate in DCPA is 1.0, and because DCPA forms stable colloids, the precipitation of DCPA was used in the nanosized pores of another material [119]. Hollow shells of DCPA with a thickness of 10-40 nm, for example, were formed on the surface of a nano-liposome [120, 121]. Moreover, spherical hollow shells of calcium phosphate were synthesized using polymeric nanotemplates [122, 123]. The dicalcium phosphate was used for the surface coating in a colloidal solution because it is stable in liquid form, has a simple molar ratio between calcium and phosphate for the synthesis, and is easier to control than other types of calcium phosphate crystallines.

1.5.3.3 Technical Concepts for Surface Coating

1.5.3.3.1 Surface Charge of Oil-in-water Emulsion Particle

Emulsions respond to environmental factors such as temperature, pressure, and free ions because of their dynamic surface. Therefore, since emulsion droplets are electrically charged due to the head group of emulsifiers, it is essential to understand the ionic interaction on the emulsion's surface. The most basic factor for evaluating ionic interaction is pH. The pH can strongly influence the emulsion and even affects the type

that is formed. Generally, water-in-oil (W/O) emulsions form at a low pH and oil-in-water (O/W) emulsions form at a high pH [33, 124-126]. This tendency implies that O/W emulsions are more stable at a high pH and vice versa.

Monitoring pH is not the only method that can be used to understand the surface properties. Zeta (ζ)-potential is another method used to monitor the surface properties. It is the electric potential that exists between the emulsion surface and dispersion medium; it is used as an indicator for the stability of the emulsion by quantifying the repulsive force among emulsion particles (Figure 1-8). Generally, for example, emulsion particles coagulate or flocculate between +/-5 mV, so the greater ζ-potential would create more separation between particles, increasing the overall stability [127].

1.5.3.3.2 Calcium Selective Electrode for the Emulsion Surface Coating

The calcium ion selective electrode (ISE) is a polymeric membrane type electrode that has great selectivity and a quick response time, and a convenient way of determining the free calcium concentration. The ISE converts the activity of a specific ion dissolved in a solution into electrical potential, determined by the Nernst equation [128]:

$$E = E_0 + S \cdot \log A \qquad\qquad \text{Eq. 1-7}$$

where E is the measured electrode potential, E_o is the reference potential, S is the electrode slope, and A is the calcium ion activity level in the solution. The membrane used for the calcium ISE is polyvinyl chloride (PVC), which is generally used for measuring nitrate, calcium, ammonium ions because it is impermeable to water [128]. The membrane has interference ions that interrupt the exchange of the selected ions by binding to the membrane, but the phosphate does not interfere in the ion exchange [128].

1.5.3.3.3 Binding Coefficient for the Emulsion Surface Coating

It is important to calculate the number of ions binding to the emulsion surface because it determines the quantity of added ions in a given concentration of the emulsion particles. The Hill equation can be used to solve this issue. If the calcium and phosphate ions exceed the amount needed to coat the surface of the emulsion particle, a calcium phosphate crystalline forms. By determining the amount of ions binding to the emulsion particle's surface, the quantity of ions that need to be added can be determined.

The Hill equation has been used in biochemistry to describe average energy of interaction per binding site in cooperative ligand binding, in this case the binding of oxygen to hemoglobin [129]. The equation is the fraction of the macromolecule saturated by ligand as a function of the ligand concentration, plotted as $\log \theta$ versus $\log$ [39] where [L] indicates the concentration of ligand. In this study, soy lecithin was modeled as the receptor and the calcium ion as the ligand [130]. The θ is expressed as follows:

$$\theta = \frac{Y}{1-Y}$$ Eq. 1-8

where Y is the fractional saturation of the protein (or the emulsion in this case). The equation describes the number of bound ligands divided by the total number of binding sites. If one ion binds to one surfactant molecule, it is a single site binding, and the Hill equation is as follows [130]:

$$\log \theta = \log K_D + n \cdot \log [L]$$ Eq. 1-9

where K_D is the dissociation constant. The Hill plot will be a straight line with slope (n). For infinite cooperatives, the Hill coefficient, which is the slope of the Hill plot, equals the number of binding sites. In fact, empirically, the coefficient is slightly less than or

equal to the number of binding sites due to the limitation of detection [130-132]. The relationship between the dissociation (K_D) and association (K_A) constants is descibred by $\log K_A = -\log K_D$ because the single site binding condition refers to $\theta = K_A[L]$.

The slope, known as the Hill coefficient (n), also describes the degree of cooperativeness between the ligand and binding receptor. When the Hill coefficient is greater than 1, the ligand binding is positively binding, meaning that the affinity for other ligand molecules increases when one ligand molecule is bound to the receptor. When the Hill coefficient is equal to 1, the ligand binding is noncooperative binding. The affinity of the receptor for a ligand molecule does not depend on other ligand molecules that are already bound. When the Hill coefficient is less than 1, the ligand binding is negatively binding, meaning that the affinity for other ligand molecules decreases when one ligand molecule is bound to the receptor.

1.5.3.3.4 Tangential Flow Filtration (TFF) for Concentration

TFF is a rapid and efficient method for the removal of water and ions from a sample. It is a simple method that easily scales to industrial levels without damaging the particles in suspension. The reason TFF is so much more effective than dead-end filtration, is because the flow of the suspension runs parallel to the membrane, through a hollow fiber (HFM) (Figure 1-9). This prevents the accumulation of particles on the HFM, allowing the water to transfer quickly and easily. This is the reason TFF is so popular in industry; it effectively removes water, concentrating the target particle, while maintaining its flux rate through several cycles.

1.6 Design of the Oxygen Release Measurement from Nanoparticle

1.6.1 Significance of the Fast Mixing Method for Oxygen Determination

The fast mixing method uses a stopped-flow apparatus in which the reaction velocity of two solutions is measured. The solutions are forced through a mixing chamber where they react and are detected. This method is used to monitor the chemical kinetics of a reaction with a given set of conditions. This method is the simplest for a quick measurement as it only takes a few seconds. Other methods used for measuring drug release can take anywhere from a few minutes to several hours. Besides the technical convenience, this method can be used to estimate the oxygen release from the sample particle by simulating the oxygen uptake to deoxygenated hemoglobin.

1.6.2 Oxygen Measurement in This Work

1.6.2.1 Significance of Usage of Hemoglobin

Hemoglobin has been utilized as a cell-free oxygen transporter. The oxygen capacity of cell-free hemoglobin is similar to that of blood [26]. Cell-free hemoglobin is free of biological regulatory mechanisms that might cause unexpected side effects and accurately conducts the reaction of binding oxygen by flow and transport. The oxygen released from the particles can be efficiently evaluated by using hemoglobin as the measurement tool.

1.6.2.2 Chemical Reaction and Kinetics of Hemoglobin with Oxygen

Understanding the principle of the hemoglobin reaction with oxygen is crucial to this measurement. Hemoglobin is a metalloprotein consisting of four iron-containing heme groups. It transports oxygen and carbon dioxide while residing in the red blood cell.

The oxygen capacity of hemoglobin is 1.34 mL oxygen per gram of hemoglobin [133]. The most common type of hemoglobin in humans is the tetramer consisting of four heme groups. Because hemoglobin has four heme groups, one hemoglobin protein enables the uptake of four oxygen molecules. The iron in the heme group absorbs and releases the oxygen molecules (Figure 1-10).

The oxygen binding of hemoglobin is determined with ultraviolet-visible spectroscopy (Figure 1-11). When oxygen is bound to hemoglobin, the absorption spectra show two peak positions at 541 nm and 577 nm; the local minimum position is at 560 nm. When the hemoglobin releases the oxygen, there is one peak at 550 nm. The amount of oxygenated hemoglobin can be estimated by observing the absorbance intensity at 550 nm according to Beer's law. If the absorbance intensity drops from its initial level at 550 nm, for example, the deoxygenated hemoglobin binds oxygen proportionally.

The oxygen capacity of the particle can be estimated when hemoglobin absorbs the oxygen released from the particle. Even though hemoglobin takes four oxygen molecules, this study is only concerned with the first oxygen molecule associated. Since oxygen uptake does not occur linearly, it is difficult to identify each oxygen uptake for the four heme groups. The reaction is described as follows:

$$Hb + O_2 \xrightarrow{k_{a_1}} HbO_2 \qquad\qquad \text{Eq. 1-10}$$

where Hb is the deoxygenated hemoglobin, O_2 is oxygen, HbO_2 is the oxygen uptake by the hemoglobin, and k_{a_1} is the rate associated with the constant of the first reaction. Even though hemoglobin has four order reactions with oxygen, this study is only concerned

with the first reaction for kinetics. Therefore, it named the pseudo-first order reaction in

this study. The reaction is as follows:

$$-\frac{d[HbO_2]}{dt} = k_{a_1}[HbO_2] \qquad \text{Eq. 1-11}$$

$$-\int_{[HbO_2]_0}^{[HbO_2]_t} \frac{d[HbO_2]}{[HbO_2]} = \int_0^t k_{a_1} dt \qquad \text{Eq. 1-12}$$

$$[HbO_2]_t = [HbO_2]_0 e^{-k_{a_1}t} \qquad \text{Eq. 1-13}$$

$$Abs_t = Abs_0 e^{-k_{a_1}t} \qquad \text{Eq. 1-14}$$

$$\ln(Abs_t) = \ln(Abs_0) - k_{a_1}t \qquad \text{Eq. 1-15}$$

$$\ln\left(\frac{Abs_t}{Abs_0}\right) = -k_{a_1}t \quad \text{or} \quad \log\left(\frac{Abs_t}{Abs_0}\right) = \log Y = -2.3k_{a_1}t \qquad \text{Eq. 1-16}$$

This derivative starts from Eq. 1-11 and ends at Eq. 1-16. Once the concentration of

oxygenated hemoglobin [HbO_2] at time t is obtained using Eq. 1-11, the [HbO_2] at time

zero and t can be measured using the absorption value and Beer's law (Eq. 1-13). By the

natural logarithm or logarithm, the fraction of the concentration of oxygenated

hemoglobin (Y) is linearly related to time. The slope is k_{a1} in the natural logarithm and

$2.3k_{a1}$ in the logarithm (Eq. 1-16).

1.6.3.3 Technical Concepts in This Work

1.6.3.3.1 Transport Phenomena of Drug Release with Hixson-Crowell

Equation

Mass transport, the study of the net movement of a body from location to another, is used in drug delivery applications to describe the diffusion of molecules; more specifically, it refers to the diffusive transport of a species due to concentration gradients. Fick's first law describes this mechanism as follows:

$$J = -D\frac{\partial \phi}{\partial x}$$

Eq. 1-17

where J is the diffusive flux, D is the diffusion coefficient, Φ is the concentration, and x is the position. The flux indicates the amount of substance per unit area per unit time. It assumes a steady state and postulates that the flux moves from high to low concentration proportional to the concentration gradient.

Applying this concept, Hixson-Crowell's cube root law has been utilized in the estimation of drug release, and it assumes that the drug is a spherical solid particle that is smaller than 500 um in diameter. The schematics in Figure 1-12 help to illustrate the concept of the equation for drug release; the modified equation for drug release estimation is as follows:

$$t = \frac{\rho \cdot r_0^2}{2 \cdot D \cdot C_s}$$

Eq. 1-18

where r_0 is the radius of particle, t is the taken time to be, r = 0 is the density, D is the diffusion coefficient, and C_s is the dissolved concentration. Though this model assumes

that the diameter of a drug "capsule" decreases, we have applied it to a rigid, non-dissolving shelled system. The validity of this assumption is based on a solid particle.

1.6.3.3.2 Measurement of Deoxygenated Hemoglobin by Clark Type
Electrode

Once hemoglobin is obtained from the red blood cells, it was purged with nitrogen gas in an isolated chamber, causing it to deoxygenate. In order to measure the dissolved oxygen in the hemoglobin solution, the Clark electrode is employed. The Clark electrode, used in this study, is a polarographic sensor consisting of a silver anode and a platinum cathode with a potassium chloride electrolyte. It is covered with a polytetrafluoroethylene (PTFE) membrane (5 um thickness) that allows for oxygen transport. The electrochemical reaction is described as follows:

- Anode reaction: $4Ag + 4Cl^- \rightarrow 4AgCl + 4e^-$

- Cathode reaction: $O_2 + 2H_2O + 4e^- \rightarrow 4OH^-$

- Overall reaction: $O_2 + 2H_2O + 4Ag + 4KCl \rightarrow 4AgCl + 4KOH$

The difference with this sensor is that the potential holds constant at 0.67 V. The sensor detects the changes in current caused by the pressure of oxygen. The greater the partial pressure of oxygen, the greater the current generated.

1.6.3.3.3 Stopped-flow Apparatus and Dead Time for
Hemoglobin Reaction

A stopped-flow apparatus was used to observe the reaction rate between oxygen and deoxygenated-hemoglobin. It works by mixing two solutions in a mixing chamber via simultaneous injection. The dead time is the amount of time that separates the mixing of

the solutions, and the first observed measurement. It is very significant and can often limit

the quality of data for a fast chemical reaction like the oxygen uptake by hemoglobin. The

dead time (t_d) is estimated as follows:

$$t_d = \frac{V}{U}$$
Eq. 1-19

where V is the volume contained between the points of mixing and observation, and U is

the flow velocity. This study uses 0.03 mL as volume and a 14 mL/sec as flow velocity.

Therefore, the t_d is 2.1 milliseconds, and because the first oxygen uptake by hemoglobin

takes 5 milliseconds [134], the t_d should be shorter than in the first reaction.

1.6.3.3.4 Relationship from Transmittance to Absorbance

In this study, a photometer was used to measure the transmittance of light

intensity of the solutions. Transmittance is the fraction of incident light at a specific

wavelength (550 nm in this study), and since Beer's law relies on absorption, the

measured transmittance was converted to absorption. The relationship is as follows:

$$\mathbf{T} = \frac{I}{I_0}$$
Eq. 1-20

$$Abs = -\log(T)$$
Eq. 1-21

where T is transmittance, I_0 is the incident light intensity, I is the intensity of the radiation

from the sample, and Abs is the absorption.

1.7 The Work in This Dissertation

The work in this study is a nanosized emulsion particle system coated with a biocompatible material, calcium phosphate, in which various thecknesses are produced. Due to the rigid nature of the coating, the product will be stable in practical conditions, withstanding long-term storage, thermal sterilization via autoclave, and physical impact of delivery from one location to another. This particle will release oxygen as fast as products without coating.

In order to produce this particle system, the phase behavior of surfactant, oil, and water was studied by creating a ternary phase diagram. This fundamental approach focused on the oil-in-water region, which enabled the coating of the particles' surface through ionic interaction. By understanding the ionic interaction of the emulsion's surface, the system was optimized for pH, calcium, and phosphate.

The coated emulsion product was tested for stability and performance in terms of oxygen release. The stability was tested by simulating practical conditions, such as delivering the product from the manufacturer to the destination, long-term storage in a dark place, and autoclave to eliminate the bacteria. The amount of released oxygen from the product was determined using the fast mixing method. The coated particle increased the stability by about 5 times, and the oxygen release amount in a given time was decreased to 70 % due to the calcium phosphate coating thickness. The different methodologies for constructing ternary phase diagrams is compared in Table 1-4.

Table 1-1 The advantages and disadvantages of oxygen carrier products (cell-free hemoglobin (HbOC)), perfluorocarbon-based emulsion (PFBOC), and calcium phosphate coated perfluorocarbon emulsion) with the potential advantages of the calcium phosphate coated emulsion.

Oxygen carrier products	Advantages	Problems
Cell-free hemoglobin (includes free, liposomal and crosslinked hemoglobins) (HbOC)	• Material is close to natural blood • Oxygen release is close to hemoglobin in red blood cells • High efficiency at atmospheric oxygen pressure	• Unexpected side-effects • Expensive procedure • Poor stability • Unstable oxygen release
Perfluorocarbon-based emulsion (PFBOC)	• Simple and less expensive procedure • Linear oxygen solubility • Synthetic product so the side effects can be anticipated	• Some toxicities are unknown • Stable in blood for only a short period of time • No construction of ternary diagram with scientific characterization
Calcium phosphate coated perfluorocarbon emulsion	• All advantages of perfluorocarbon-based emulsions • Potential to be in powder form for convenience of delivery • Potential to be stable in blood over a longer period of time • Potential to be easily separated from blood	• Unproven

Table 1-2 Examples of the types of surfactants according to charged head groups, modified from [135-138].
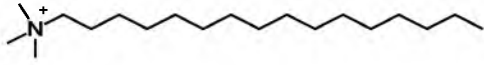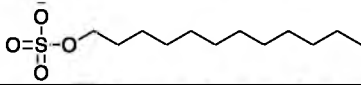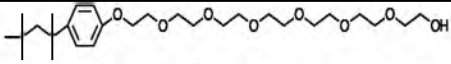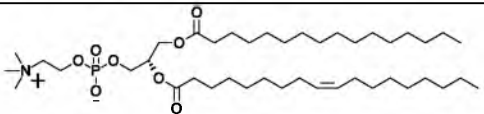
Types of surfactants by charged head groups	Names	Chemical structures
Cationic	cetyltrimethylammonium bromide	
Anionic	sodium dodecylsulfate	
Nonionic	Triton X-100	
Zwitterionic	L-α-phosphatidylcholine	

Table 1-3 The types of calcium phosphate formulation with the molar ratio between calcium and phosphate; data source [139]. Ca and P indicate calcium and phosphate.

Type of calcium phosphate	Chemical structure	Solubility at 25°C, -log K_S	Molar ratio (Ca/P)
Monocalcium phosphate monohydrate (MCPM)	$Ca(H_2PO_4)\ 2H_2O$	1.14	0.5
Dicalcium phosphate (DCPA)	$CaHPO_4$	6.90	1.0
Tricalcium phosphate (TCP)	$Ca_3(PO_4)_2$	25.5 for α 28.9 for β	1.5
Amorphous calcium phosphate (ACP)	$Ca_xH_y(PO_4)_z$	25-32[a]	1.5
Hydroxyapatite (HAp)	$Ca_{10}(PO_4)_6(OH)_2$	116.8	1.67
Tetracalcium phosphate (TTCP)	$Ca_4(PO_4)_2O$	38-44	2.0

[a] The solubility cannot be measured precisely. The solubility varies depending on pH.

Table 1-4 A comparison between the different methodologies for constructing ternary phase diagrams.

Current methodologies

Methods	What do they measure?	Advantages	Disadvantages
Visual inspection	• Phase separation	• Fast and east	• Inaccuracy
Shear stress and strain	• Surface tension of rheological behavior	• Mapping the ternary phase diagram by accurately understanding the phase behavior	• Specialized tools required • Takes a long time for performance
Cryogenic transmission electron microscopy	• Morphology of emulsion in image	• Actual image	• Requires special technique • Expensive equipment and tools

Potential methodologies

Methods	What do they measure?	Advantages	Disadvantages
Buoyant density	• Oil encapsulation by comparing the measured and estimated weights	• Fast and easy	• Inaccuracy
Fluorescence quenching	• Morphology of emulsion by monitoring chemical reaction	• Cheaper than TEM	• Requires special sample holder
Fourier transform infrared spectroscopy	• Oil content by monitoring chemical functions	• Fast and easy to handle • Sensitive • Inexpensive • Spectra are information rich	• Some molecules cannot be detected
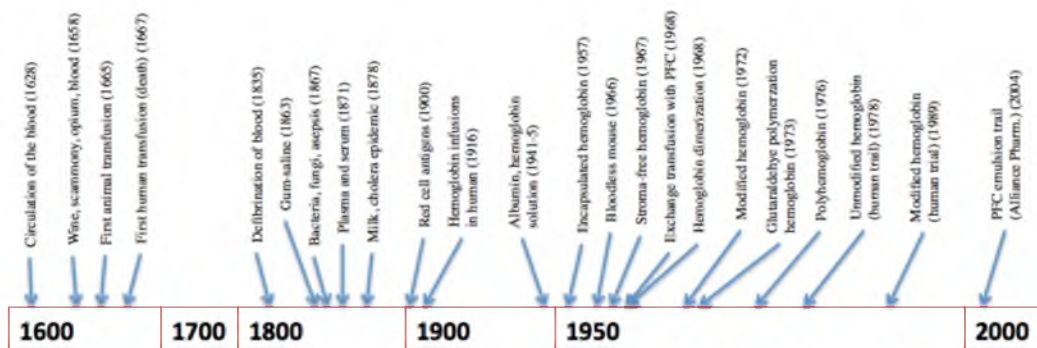
Figure 1-1 The history of oxygen therapeutics (blood substitute), adapted from [3]. The perfluorocarbon research has been investigated since 1950s.
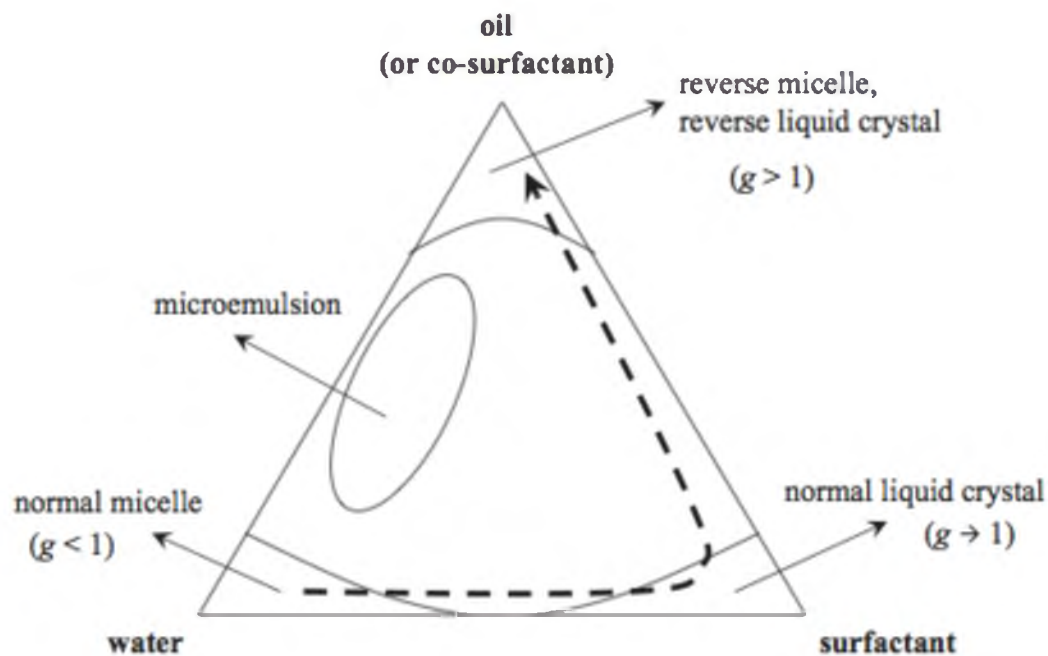
Figure 1-2 The typical ternary phase diagram of oil/water/surfactant. Each apex forms a type of emulsion, governed by the majority component. The normal micelle is formed at the corner dominated by water, the reverse micelle at the corner dominated by oil, and liquid crystal at the point dominated by surfactant. This is largely the result of organization of surfactant molecules among themselves to form bilayers and multilamellar structures. g represents the packing parameter, estimating the micelle structures.
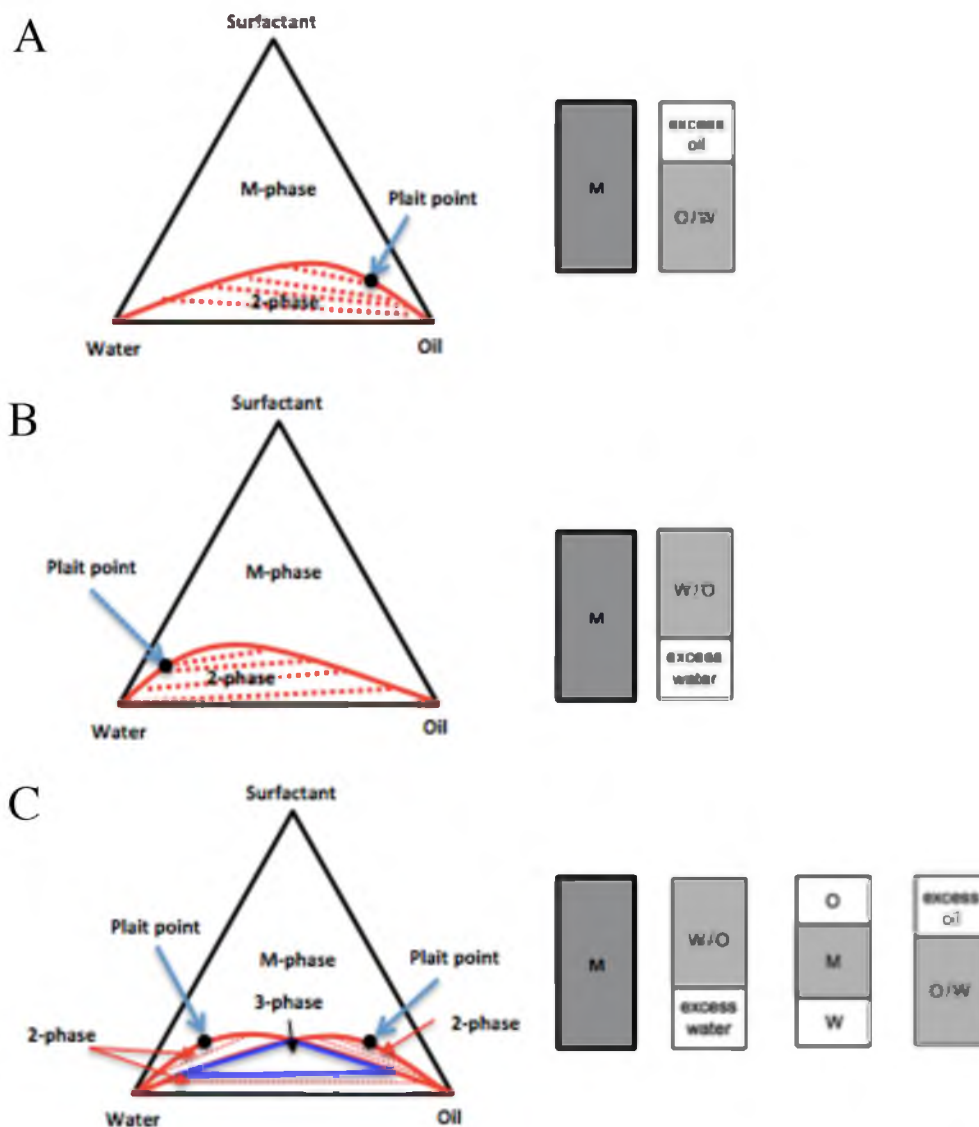
Figure 1-3 The visual phase separation classified by Winsor Type and ternary phase diagrams with Winsor system assuming the density of oil is less than water. The phase separation proceeds along tie lines. Tie lines connect compositions of two immiscible liquids in equilibrium [42]. Any mixture with an overall composition along a tie line provides the same two immiscible liquid compositions. The amounts of two liquids change only as the overall composition changes from one liquid side of the bimodal curve to another one. Plait point is a critical point at which two liquid phases are identical. A) Winsor Type I has two possible phases: 1) emulsion-formation phase (1-phase), and 2) 2-phase, containing oil-in-water phase (O/W) with excess water. B) Winsor Type II has two possible phases: 1) emulsion-formation phase (1-phase), and 2) 2-phase, water-in-oil phase (W/O) with excess oil. C) Winsor Type III has four possible phase: 1) emulsion-formation phase (1-phase), 2) 2-phase, locating to water-side, O/W phase with excess water, 3) 3-phase: emulsion-formation phase (M) excess oil (O) and water (W), and 4) 2-phase, locating to oil-side, W/O phase with excess oil.
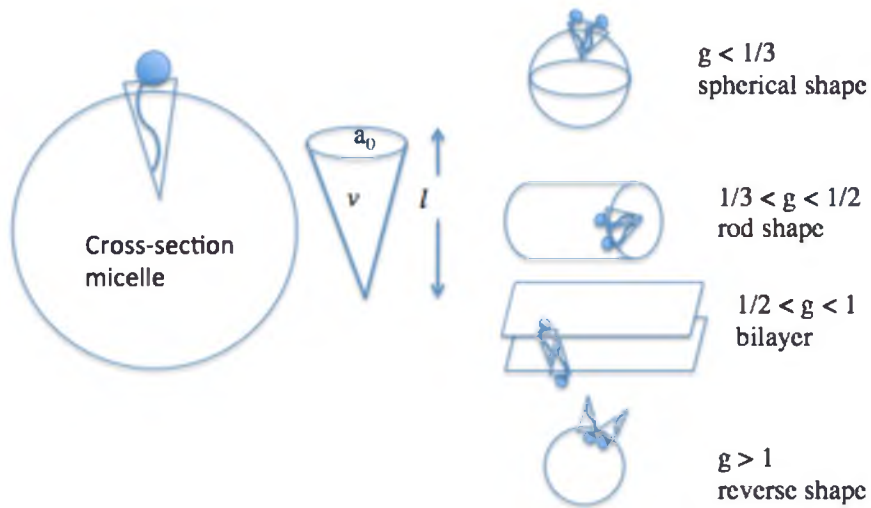
Figure 1-4 The schematics of micelle formation, adapted from [49]. a_0 is the area of the head group of the surfactant, l is the length of the hydrocarbon chain, and v is the volume of the hydrocarbon chain. As seen in the cross-section, the micelle is formed by an aggregate of surfactant. The packing parameter (g) estimates the micelle structure: spherical, rodlike, bilayer, or reverse.
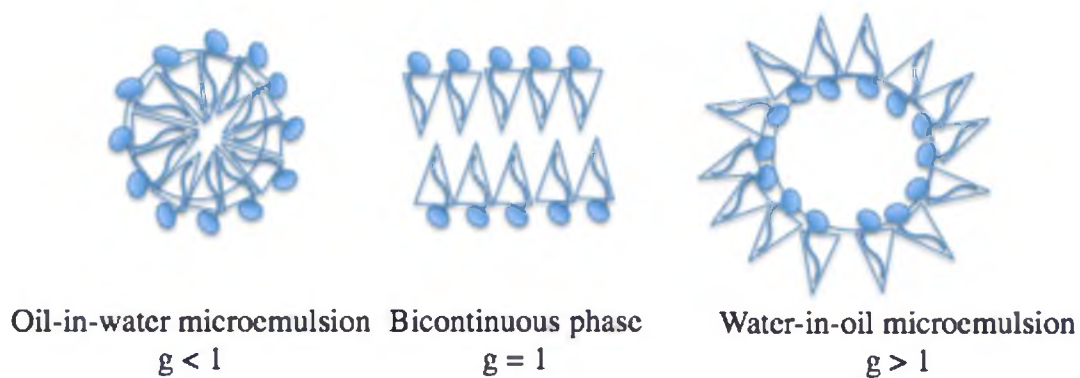
Figure 1-5 The schematics of microemulsion relying on the packing parameter (g), adapted from [49]. When g is less than 1, the emulsion forms an oil-in-water (O/W) microemulsion. When g is equal to 1, it is bicontinuous. When g is greater than 1, it is a water-in-oil (W/O) microemulsion
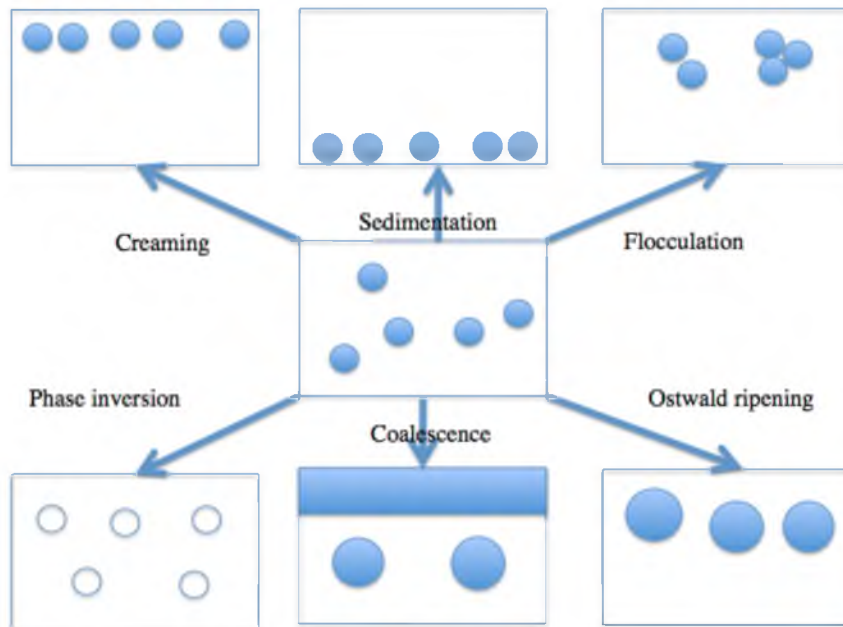
Figure 1-6 The schematics of breakdown processes in emulsion, adapted from [49].
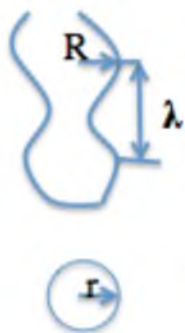
Figure 1-7 The Plateau-Rayleigh instability, adapted from [75]. A column of fluid of radius (R) experiences perturbation of wavelength (λ) in the stream and is broken up into droplets in radius (r).

A: negative surface charged particle
B: Stern layer
C: Slipping plane
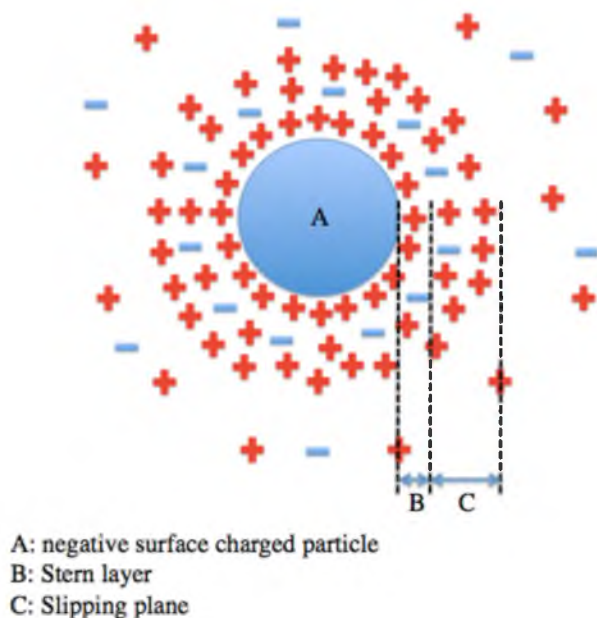
Figure 1-8 The schematics of a particle with ionic potential difference as a function of the distance from the charged surface of the particle, adapted from [140]. The particle surface, negatively charged, attracts positive ions. The first region is called Stern potential. The second region of potential is less influenced by the charge on the particle's surface. Therefore, few negatively charged ions are attracted to the particle due to the Stern potential. This region is called the zeta potential.
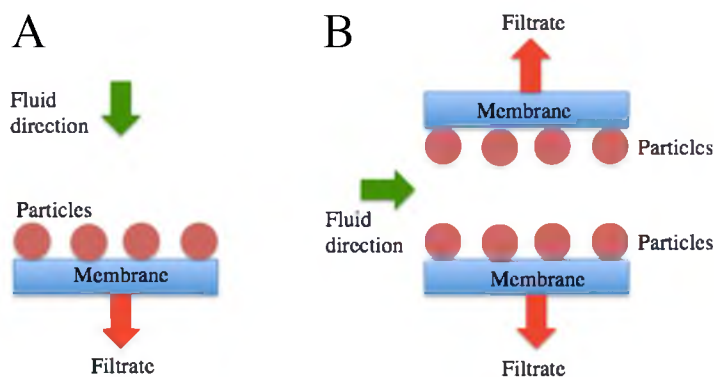
Figure 1-9 The schematics of direct and tangential flow filtration, adapted from [141]. A) Direct flow filtration: the particles flow perpendicularly on the membrane's surface. The particles larger than the pore size of the membrane block the membrane's surface, slowing down the flow rate. B) Tangential flow filtration: the smaller particles pass through the membrane in parallel. Since the larger particles keep circulating in the system, the flow rate does not slow down.
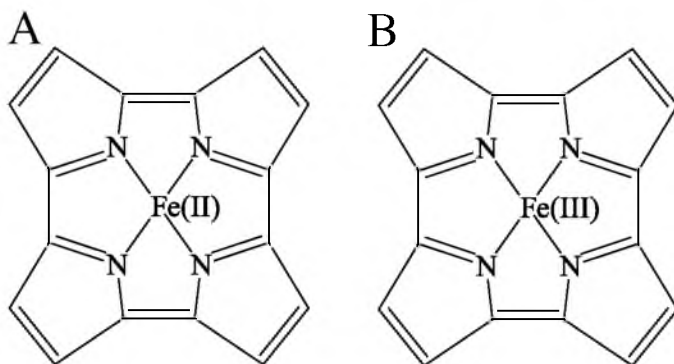
Figure 1-10 The schematics of hemoglobin and heme groups, adapted from [143]. When the heme reacts with oxygen, iron (Fe) changes from A) Fe (II) to B) Fe (III).
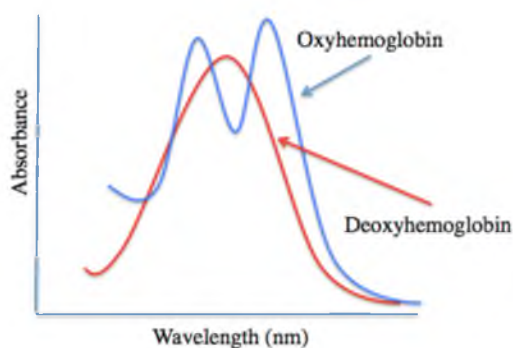
Figure 1-11 The absorbance of oxy (red) and deoxyhemoglobin (blue) as a function of wavelength, adapted from [144]. The peak positions of oxyhemoglobin are at 541 nm and 577 nm and deoxyhemoglobin is at 550nm. The local minimum peak of oxygehemoglobin is at 560 nm.
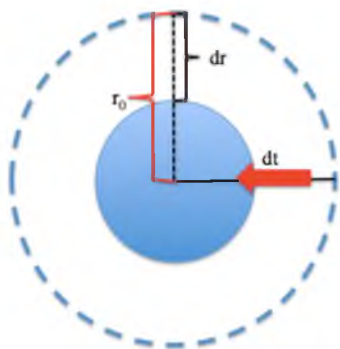
Figure 1-12 A schematic showing the radius change over time as drug release. The r_0 indicates the initial radius of the particle, and dr is the change in radius in change of time (dt). The assumption is that the solid particle dissolves in a solution; the particle size becomes smaller as a function of time.

CHAPTER 2

DEVELOPMENT OF TERNARY PHASE DIAGRAMS FOR THE

OIL-IN-WATER PHASE: DOPA/PFOB/WATER AND SOY

LECITHIN/PFOB/WATER

2.1 Abstract

Phase studies are essential for understanding the potential behavior and

formulation properties of an emulsion system. Phase diagrams for emulsions are

challenging to understand due to the complex equilibrium formed by its three

components: a surfactant and two immiscible liquids. This chapter focuses on the

investigation of two phase diagrams, one system with an anionic surfactant (1,2-dioleoyl-

sn-glycero-3-phosphate (DOPA), and the other with a zwitterionic surfactant (soy

lecithin). The primary objective was to find the optimal conditions for the oil-in-water

phase in both systems with the same immiscible liquids: perfluorooctyl bromide (PFOB)

and water. Phase transition boundaries were determined by five different characterization

methods: 1) A general approximation of the ternary diagrams were constructed by a

visual classification of the phases; 2) the buoyant density was utilized to determine how

efficiently the liquids were incorporated into the emulsion; 3) the oil-in-water phase was

confirmed by observing its fluorescent quenching affect; 4) FT-IR quantitatively

determined the amount of PFOB effectively encapsulated by the surfactants; and 5) cryo-

TEM was used to visualize the phases present. The soy lecithin system had an oil-in-water region that was 36 times greater than that of DOPA. In conclusion, the conditions for proper oil-in-water phase formation are less restrictive for the soy lecithin system when compared with DOPA, allowing for greater variability in the components to achieve the same phase characteristics.

2.2 Introduction

Ternary diagrams are frequently used in the cosmetics, drug delivery, and food science industries to describe not only the formation of the emulsion, but also its stability and the role of the surfactant architecture. They allow product developers to predict certain characteristics such as shapes, sizes, and properties of the emulsions, while streamlining the scheme and helping achieve an overall understanding of the system. The ternary diagrams presented in this study have been classified by the visual appearance of the samples, and then verified for consistency against other well-known systems like the Winsor system. The obvious demerit of this method is that the classification process is completely subjective, and dependent on the judgment of the observer, so a more detailed and in depth analysis is needed to properly identify the desired phases.

In the emulsion monolayer, the packing structure of the phospholipids greatly influences the physical and chemical properties of the particle. To understand the degree of variability due to the headgroup, two surfactants were chosen: an anionic phospholipid called 1,2-dioleoyl-sn-glycero-3-phosphate (DOPA), and a zwitterionic phospholipid named L-α-phosphatidylcholine (soy lecithin). With a zwitterionic lipid, it was expected that the packing density would be greater than that of the anionic DOPA due to the force balance between the repulsive and attractive forces of the adjacent headgroups. In

addition, larger packing densities were anticipated to coincide with structural phase region properties, which is the main focus of this study.

This chapter presents the observations and analysis of both the physical (i.e., number of separated layers and buoyant density) and chemical interactions (FT-IR and fluorescence quenching) of the oil-in-water (O/W) phase. A small O/W phase region for the DOPA system results in greater variability in phase properties, but reproducibility becomes a genuine concern. For this reason a comparison study, designated by five tests (Figure 2-1), was essential to determine the sensitivity of the two systems, DOPA and soy lecithin, and their respective component ratios.

In order to further understand the system behavior, five methodologies (Table 2-1) were employed to characterize the types of emulsions in the systems. The first of which was visual observation, where each of the samples was surveyed, without any visual aid, to determine if an obvious phase separation had occurred. The second approach was to measure the buoyant density, thus taking advantage of the difference in density between water and perfluorooctyl bromide (PFOB, specific gravity: 1.93 [53]) to identify a phase. The third approach was Fourier transform-infrared spectroscopy (FT-IR), which, through Beer's law, was used to determine the concentration of PFOB in the sample, as it is proportionally related to the absorption intensity at a given peak position. This is more sensitive than the buoyant density so it further refined the criteria of an O/W emulsion. The fourth approach was fluorescent quenching, which was the result of mixing pyrene (Py) dye in PFOB and the corresponding quencher (potassium iodide, KI) in water. Upon encapsulation the dye would be quenched and a decrease in fluorescence monitored. For instance, when the morphology of the emulsion is openly continuous, the Py can freely move across the oil and water interface and quenching results. Finally, the

morphology of the emulsion was observed by cryogenic transmission electron microscopy (cryo-TEM). Freezing the emulsion in liquid nitrogen causes the emulsion to instantly become suspended in a thin ice film, protecting the volatile sample from vaporization while under the electron beam.

2.3 Materials and Methods

2.3.1 Construction of the Ternary Phase Diagrams

For this experiment, two types of emulsion were prepared, each with a different type of surfactant: 1) An anionic surfactant, 1,2-dioleoyl-*sn*-glycero-3-phosphate (DOPA, $C_{39}H_{72}O_8Na$ from Avanti Polar Lipids, Inc., Alabaster, AL), and 2) a zwitterionic surfactant was L-α-phosphatidylcholine (soy lecithin, $C_{42}H_{80}NO_8P$ from Avanti Polar Lipids, Inc., Alabaster, AL). The same oil and 18.2 mΩ-cm water (pH 7) were used in both ternary diagrams: perfluorooctyl bromide (PFOB, C_8BrF_{17} from Oakwood Product, Inc., West Columbia, SC), and all experiments were conducted at room temperature.

To make the many points required for construction of the ternary diagram the titration method [41, 145, 146] was employed. The surfactant and oil were first added to a 20 mL glass vial. The mixture was stirred at 300 rpm using a magnetic stir bar (Teflon, ¾"). After 1 minute, the mixture was diluted with deionized (DI) water (18.2 mΩ-cm, pH 7) dropwise within a 10 second time frame. The emulsion mixture was stirred at 1200 rpm for an additional 30 minutes, after which it was removed from the plate and allowed to relax for 6 hours to ensure equilibrium [51]. The phases were then visually counted and identified, and the process was repeated until the composition reached the end of the tie line, shown as the blue dashed lines in the ternary diagram (Figure 2-2).

2.3.2 Measurement of the Buoyant Density

The density of each phase was measured individually to estimate the effective usage of PFOB and water in forming the emulsion. The effective usage was defined, in this experiment, as the amount of PFOB associated with surfactant. One region was chosen to represent the buoyant density of each phase region in the ternary diagram of DOPA, for a total of six samples. The selected regions ran along lines parallel to the water and surfactant axes as shown in Figure 2-3. The detailed weight fractions for each region are described in Table 2-2. For the soy lecithin system, the same six weight ratio values were made allowing for a direct comparison between the two surfactants.

To prepare the sample, the surfactant and oil were added to a 20 mL glass vial, while keeping the total added volume of the PFOB and the water at a constant 10mL. The weight of the surfactants was measured with a calibrated digital scale (OHAUS Explorer with the readability 0.0001 gram from OHAUS Co., Parsippany, NJ). The six samples in Table 2-2 were all synthesized in 5mL aliquots; however, for the buoyant density measurement the pycnometer only requires 3.5 mL, allowing for accurate volume measurements.

A cylindrical shape vial (3.5 mL; height: 2.0 cm, diameter: 1.5 cm) with an open top was used as a pycnometer to consistently measure the weight of the various phases. The vial made working with the gels and gel-like samples easier, and it was calibrated to obtain the buoyancy error. The correction factor is dependent on the true mass (m), and measured mass (m'), and is shown by the Buoyancy equation [45].

$$\frac{m}{m'} = \frac{\left(1 - \frac{d_a}{d_w}\right)}{\left(1 - \frac{d_a}{d}\right)}$$

Eq. 2-1

In Eq. 2-1, d_a is the density of air with the altitude (0.0010 g/mL at 20 $^{\circ}$C at 4400 ft. [147]), d_w is the density of the calibration weight (7.8 g/mL for the stainless steel pan [45]), and d is the density of the objective weighed. Using DI water at 20 $^{\circ}$C, the measured density (d) was 0.9896 g/mL. As a result, the error was 0.09 % less than the actual mass. The measured density (ρ) of the phases was calculated by follows:

$$\rho = \frac{mass}{volume} = \frac{W_F - W_E}{V} \qquad \text{Eq. 2-2}$$

where W_F is the weight of the cylinder filled with the sample, W_E is the weight of the empty cylinder, and V is the volume of the vial.

2.3.3 Fluorescence Spectrometry

In the material selection, pyrene (Py) was selected as the fluorescent dye because it is soluble in both PFOB and water [148], and is easily quenched with potassium iodide (KI) which is only soluble in water [60]. There were two quenching control experiments: 1) pyrene in PFOB, and 2) pyrene in water. In the first control experiment, the pyrene was dissolved in PFOB at a saturated concentration of 4.51 x 10^{-4} mM [148]. The mixture was stirred at 300 rpm until the pyrene was totally dissolved in the PFOB, then the mixture was titrated by 10 mM KI. After each titration, the mixture was vortexed for 15 seconds, and the fluorescent intensity of the mixture was measured immediately after by fluorescence spectroscopy (Cary Eclipse, Varian, Palo Alto, CA). The second control experiment followed the same procedure as the first, with the same concentration of pyrene dissolved in water, and again, potassium iodide was titrated to the mixture. The excitation wavelength of pyrene was 337 nm [149], and the collected wavelength range

was from 360 nm to 450 nm. The photomultiplier (PMT) detection voltage was 500 volts, with an integration time of 0.1 seconds. The mechanism of this system is as follows:

$$Py^* + Q \rightarrow Py + Q \qquad \text{Eq. 2-3}$$

where Py is the pyrene, Q is the quencher, potassium iodide (KI), and * designates an excited state. Three peaks at 373 nm, 385 nm, and 393 nm dominate the emission of pyrene. The 373 nm and 393 nm peaks are difficult to differentiate from water, so the 385 nm peak became the focal point of the investigation. The peak distributions vary because the excited state of the nonplanar structure differs from that of the original ground state.

Before synthesizing the samples, a stock solution of 4.51×10^{-4} mM pyrene was made in PFOB and a 2.24 mM KI solution in water. These concentrations were chosen because in the control tests, it was this combination that showed the greatest decrease in fluorescence intensity at 24 % when combined, see Figure 2-4. A small volume of the sample was extracted for the measurement and placed in a customized sample holder for the front face accessory of the fluorescence spectrometer. Based on the cylindrical dimensions of the customized holder it was estimated that it had a 22 uL capacity (Figure 2-5). The front-face accessory (Accessory Solid Sample Holder, Varian, Palo Alto, CA) with an angle of 62° is useful for opaque samples because the exciting and emitted light pass through the same face (Figure 2-6) [46]. This allows the sample to be measured without further dilution, which would undoubtedly alter the phase and quenching characteristics that were being measured.

2.3.4 Fourier Transform Infrared Spectroscopy (FT-IR)

The same samples made for buoyant density measurements were further analyzed

with FT-IR (Varian 3100 FT-IR, Varian Inc., Palo Alto, CA), and the attenuated total

reflectance (ATR) (MIRacle™ Single Reflectance ATR, Pike Technologies, Medison,

WI) accessory. As seen in Figure 2-7, the dimension of the crystal surface on the ATR

was 2.2 mm × 3.0 mm [150], and the penetration depth was 2.0 um [150]. Using this

information, the minimum required volume for the ATR was 2.9×10^{-2} uL for a reliable

measurement. For each measurement, 10 uL of the sample was dropped on the ATR

crystal surface using a pipette. The FT-IR was set up at a resolution of 4 cm^{-1} and the

number of scans to 150.

2.3.5 Cryogenic Transmission Electron Microscopy (cryo-TEM)

Cryo-TEM imaging allows nearest to native views of aqueous specimens, which

are notoriously difficult to view due to the free mobility of the particles, not to mention

the incompatibility of liquid samples with the electron beam and high vacuum system of

conventional TEM. So, In order to preserve liquid and biological samples they are frozen

into a thin film with liquid nitrogen.

For low viscosity samples 3 uL was dropped onto a carbon grid with a pipette, but

because the highly viscous samples (i.e., gel-like emulsion) are not compatible with

pipettes, the samples were smeared onto the TEM carbon grids using a pipette tip and

blotted for 3 seconds using Vitrobot (FEI, Hillsboro, OR). After the sample was mounted,

the blotted grid was submerged in liquid nitrogen and observed under a FEI Tecnai™

TEM (FEI, Hillsboro, OR) at 120 keV. The procedure of the cryo-TEM is summarized in

Figure 2-8.

<u>2.4 Results and Discussion</u>

2.4.1 Construction of the Ternary Phase Diagrams

The goal of the experiment was to observe the phases and boundaries in the given materials. The phases of the emulsion were classified using three factors: number of layers, layer color, and viscosity. The number of layers is important because it is a good indicator of the number of phase types present, such as O/W, W/O, and bicontinuous [42]. Second, the emulsion was categorized by the relative amounts of visual turbidity, which can also suggest phase type [151]. Third, the viscosity is also related to the formulation of the emulsion phase, because the packing of the particles plays a significant role in determining the viscosity of the system [152]. If the emulsion, for example, has a cross-link structure like gels, then this system would be expected to be more viscous than a dispersed particle system.

The ternary diagram of the DOPA emulsion system had six phases while the soy lecithin system only had four. First, in the DOPA system, all two-layer phases had a boundary at the water axis. Phase E and F were opaque while the rest were semi-transparent; Phase C and D demonstrated more transparency than A and B. Phase A and B had the lowest viscosities, while Phase C and D became more gel-like, and Phase E and F were sticky-gels. Thus, for the DOPA emulsion system, similar samples properties grouped A and B (blue), C and D (yellow), and E and F (red) in Figure 2-9. The soy lecithin system also showed the two-layer phase was bound the water axis, similar to the DOPA system. Furthermore, the phases were opaque. Phases A and B were the least viscous while Phase C and D were sticky gels. It should be noted that this system did not have a gel-like phase. Based on similar observations, the soy lecithin system was grouped into two types, as in Figure 2-10 Phase A and B (blue) and Phase C and D (yellow).

The established Winsor system has three types of the emulsion ternary diagrams depending on the number of layers in Figure 1-3 [153]. Winsor Type I and II exhibited two layers, located in near the oil-water side [153]. Even though the Winsor Type II also showed the two-layer region on the same side in the ternary diagram, the difference was the value of Winsor R, which is the ratio of the total interaction energies per unit area of the surfactant for the oil and water phase. It is expressed as follows [154]:

$$R = \frac{c_{LO}}{c_{HW}}$$

Eq. 2-4

where, by counting the number of carbons in the surfactant molecule: C_{LO} is the lipophilic portion of surfactant in the oil and C_{HW} is the hydrophilic portion in the water. The R value of Winsor Type I is less than 1 while Winsor Type II is greater than 1. Because the Winsor R values of DOPA and soy lecithin were 1/5 and 1/3, both ternary diagrams were classified as Winsor Type I.

In conclusion, according to the ternary diagram the area of the one phase system with DOPA (regions A, C, and E) is roughly 1.5 times smaller than the one phase region of the soy lecithin system (regions A and C) in Figure 2-11. This implied that more soy lecithin molecules were required to form the emulsion, which could be due to the net neutral charge of the head group on the lipid, which is made of positive and negative charges from the amine and phosphate groups, respectively, while DOPA has only the negative charge of the phosphate group. Due to the repellent force by the ionic charge on the head group of DOPA, the area of the occupation per head group on the emulsion surface is greater than soy lecithin, therefore the number of the lipid molecules required to form an emulsion particle of the same size is less for DOPA.

2.4.2 Buoyant Density for the Dispersion of Liquids

The goal of this experiment was to estimate how the oil and water were dispersed in the emulsion. In the buoyant density, the one-layer region expressed a density close to that of water. Even though the added amount of PFOB varied, the density of the turbid layer in the two-layer phase was close to water and the transparent layer was similar to PFOB. These phenomena were observed in both DOPA and soy lecithin systems (Figure 1-3).

Since the specific gravity of PFOB is known, a simple calculation with the Rule of Mixtures equation can provide an ideal density for a certain ratio of PFOB to water. This value is then compared to an experimentally measured value to derive the approximate amount of PFOB that is suspended as an emulsion. The density of PFOB is 1.93 g/mL while water is 0.9982 g/mL at 20 $^{\circ}$C, so the density of the emulsion is primarily determined by the amount of PFOB. The expected density was calculated as follows:

$$\rho_f = \frac{(\rho_1 \times V_1) + (\rho_2 \times V_2)}{V_1 + V_2} \qquad \text{Eq. 2-5}$$

where ρ_1 and ρ_2 are the densities of the liquids (PFOB 1.93 g/mL [28] and water 0.9982 g/mL at 20 $^{\circ}$C [155]), and V_1 and V_2 are the added volume of the mixed liquids.

In conclusion, the difference between the measured and the calculated densities indicates the degree to which the oil and water are used in forming the emulsion (Table 2-3). When compared to the calculated densities of the suspensions the DOPA system showed that more than 90 % of the combined liquids were used to form the emulsion in Region **a**, **c**, and **e**, whereas Region **f** suggested poor integration

(Figure 2-12). In the soy lecithin system, Region **a**, **c**, and **e** also showed high efficiency formation while Region **f** was the lowest. Region **a**, **c**, and **e** were the single-layer phase; this comparison indicated that the single-layer phase was most efficient at forming emulsions with a given amount of PFOB.

2.4.3 Quantitive Analysis of PFOB by FT-IR

The goal of the experiment was to quantitatively determine the amount of oil employed to form the emulsion. The Fourier transform infrared spectroscopy (FT-IR) spectra of the control samples were performed and can be seen in Figure 2-13 and Figure 2-14. Figures 2-16 and 2-17 show the FT-IR spectra for the different phases of the DOPA and soy lecithin emulsions, respectively. There are two factors that determine the intensity of the IR spectrum. First, different functional groups have different vibrations, which yields various wavenumber absorbances because of changes in dipole moment and bond distance. The second factor is the concentration of molecules in the sample; this is determined by following Beer's law, which directly relates the concentration with the intensity. In the control experiment, each material was characterized by FT-IR to establish a reference for each raw material of the emulsion. The peak positions suggested the presence of a hydroxyl group (-OH) in water that had a wide range between 3000 - 3600 cm^{-1} (stretching) and at 1640 cm^{-1} (bending). The difluromethylene (CF_2) in PFOB displayed the strongest intensity at 1200 cm^{-1} and 1140 cm^{-1}. Both DOPA and soy lecithin showed a phosphate peak (P=O) at 1170 cm^{-1}, and soy lecithin had an additional amine peak (C-N stretching) at 1250 cm^{-1}.

The emulsion samples of DOPA and soy lecithin were monitored using the reference peak positions from the control experiments. The primary goal in monitoring

the difluromethylene peak was to determine the amount of PFOB. In the DOPA and soy lecithin emulsion systems, inspection of the line **a, c,** and **e,** suggested that as the amount of surfactant increased in the system (with PFOB held constant), the FT-IR spectra came to resemble the pure surfactant reference plots.

The next set of samples were made by keeping the amount of lipid constant, while increasing the amount of PFOB as in line **b**, **d**, and **f**. Unlike the surfactant experiment explained above, the FT-IR peak intensity of the PFOB did not increase as more PFOB was added to the system. In order to properly determine the amount of PFOB encapsulated in the emulsion, it was necessary to do a careful examination of the spectra. The carbon bond (–C-C-C) at 1064 cm^{-1} was analyzed to ensure the presence of surfactants. A direct analysis of peak intensity between the $-CF_2$ (1200 cm^{-1}) and $-P=O$ (1170 cm^{-1}) peaks was not viable due to the overlap in the region. An encapsulation rate of greater than 50% was arbitrarily defined as a system that efficiently used surfactants to create an oil-in-water phase because at this region it is possible to conclude that a majority of the liquids were employed. With this definition it was concluded that Region **a** and **c** were the optimal regions for our desired emulsion system. The detailed calculations are provided in Appendix A. The results of the DOPA and soy lecithin emulsion systems are shown in Figure 2-17.

In conclusion, the soy lecithin system had a broader region for the oil-in-water phase than DOPA (Figure 2-17 (C) and (D)), making it more effective. This is thought to be a result of tighter packing of soy lecithin due to the neutral net charge of head group.

2.4.4 Fluorescent Quenching

The goal of this measurement was to support the classification of the proposed oil-in-water phase. Before conducting the quenching experiments it was important to first consider the conceivable mass transport mechanisms for the encapsulation system. This greatly depends on the solubility of species in a solvent, as well as interface environments. In Figure 2-18 (A), if the pyrene is encapsulated inside an O/W emulsion, assuming it is soluble in both polar and nonpolar solvents, it can readily diffuse across the lipid monolayer. In Figure 2-18 (B), the reverse situation is shown, where the KI is encapsulated in a W/O emulsion; however, KI is only soluble in aqueous environments. Knowing this, it was hypothesized that the KI would remain inside of the W/O emulsion even though it has a high interior concentration. In Figure 2-18 (C), if the emulsion is an open system where molecules are free to roam from one preferred solvent to another, then Py and KI have a greater chance of reacting.

In order to better understand the type of phase, an experiment was designed to take advantage of the sensitivity of fluorescence spectroscopy to monitor quenching effects. Due to the fact that KI (the quencher) is only soluble in water, a decrease in the fluorescence intensity of pyrene was only expected for the aqueous phase. In the initial control experiments pyrene was dissolved in water (4.51×10^{-4} mM) and titrated with KI (2.24 mM) while monitoring the fluorescence intensity. The result (shown in Figure 2-4) supported the notion that adding KI to pyrene quenched the emitted light, upon further analysis it was found that the decrease in emission intensity was linearly dependent on the concentration of KI. This experiment was repeated with the pyrene dissolved in PFOB, which showed that there was no significant decrease in emission intensity.

Based on the concepts of the initial idea described above, the regions with maximal and minimal fluorescence extinctions would be respectively classified as the bicontinuous and W/O phases; examination of the data, presented in Figure 2-19, suggested Regions **b** and **d** for both the DOPA and soy lecithin systems. For the DOPA coordination (Figure 2-20), Region **a** proved to be the second most resilient to quenching, a characteristic observed in Regions **a** and **c** of the soy lecithin experiment (Figure 2-21). This secondary region was significant because it indicated an environment that would be consistent with the initial proposal and an oil-in-water phase. In conclusion, Region **b** suggested a bicontinuous phase in both DOPA and lecithin systems because the fluorescence dye was the most efficiently quenched at this composition. Region **d** was the water-in-oil phase of both systems since the quencher did not affect the dye. However, the rest of the compositions (**a**, **c**, **e**, and **f**) required the quantitive analysis of PFOB by FT-IR for their identification.

2.4.5 Observation of Morphology by cryo-TEM

In the previous characterizations, the regional compositions of the desired phase (oil-in-water) were established; 1) the visual inspection showed the possible phases and helped to determine the boundaries in the ternary diagram, 2) the buoyant density was used to estimate the efficiency of the emulsification by dispersing oil and water in the emulsion system, 3) the fluorescence quenching helped to differentiate between bicontinuous and water-in-oil phases, and 4) FT-IR quantified the efficiency of the used oil to form the emulsion. Even though these characterizations helped to further define the oil-in-water phase, one more step was required to finalize the definition of the O/W phase morphology.

To better understand the morphology of the emulsion system, the synthesized DOPA and soy lecithin emulsions were viewed under cryo-TEM (Figures 2-22 and Figure 2-23). In the micrographs a darker feature is consistent with higher density or thickness when compared to the surroundings [44], and because of the relatively high density of PFOB, an oil-in-water emulsion would appear as a black circle. If the particle were formed as a liposome, containing a water core, there would be little contrast between the inner and outer regions of the lipid layer. In both systems, DOPA and soy lecithin, Regions **c** to **f** were too viscous for a drop wise application, so they were smeared onto the grids with a pipette tip before blotting.

As indicated in Table 2-4, Region a in both DOPA and soy lecithin emulsion systems exhibited a spherical morphology containing a darker core which, as explained previously, is indicative of an O/W phase. There were a wide variety of shapes in Regions **b**, **c**, and **d** of both systems and the lack of contrast between multiple layers suggested the formation of a liposome and an excess of lipid. Regions **b**, **c**, and **d** in the DOPA trial showed structures expected of empty liposomes. Meanwhile, in the soy lecithin system Regions **b** and **c** revealed few particles containing PFOB and Region **d** did not have any such structure. Even though the added amount of PFOB in Region **b** was greater than that of a in the soy lecithin system, only some of the particles contained oil. In the case of soy lecithin the amount of PFOB in Region **c** was identical with Region **a**, but Region **c** showed a greater number of particles with the oil core. The images of Region **d** show a W/O phase when taking into consideration the ternary diagram and visual observations. Region **e** and **f** in both systems displayed a wave-pattern, which implied a bicontinuous phase. Finally, a spherical morphology was observed by cryo-TEM, which is also consistent with the expected O/W emulsion (Figure 2-22 and Figure 2-23).

The results from the five characterization methods are summarized in Figure 2-24 and Figure 2-25; a follow-up to the questions proposed in Figure 2-1. After all of the information had been collectively analyzed, this summary concluded that Phase A, in both the DOPA and soy lecithin emulsion systems, was the oil-in-water phase. There was no apparent excess liquid PFOB. The measured buoyant density was similar to the theoretical calculation (Figure 2-12). FT-IR spectra demonstrated the encapsulation rate for PFOB (Figure 2-17). The quenching effect showed that pyrene was trapped in PFOB reservoirs by preventing the quenching of pyrene by potassium iodide (Figure 2-21).

From the soy lecithin ternary diagram it was observed that Phase A is 36 times larger than the same phase in the DOPA case. This implied that soy lecithin was better at forming the oil-in-water when compared to DOPA. This is most likely attributed to soy lecithin's amphiphilic head group in contrast with anionic DOPA. Because soy lecithin does not express a repelling force between like charges, more of the molecules are required to form the emulsion. When looking at Region b of the soy lecithin system it was discovered that it is most qualified, from the five characterization tests, to be the bicontinuous phase. This implication was confirmed by wave-like patterns observed via cryo-TEM (Figure 2-23, B). When analyzed from a broader perspective it was concluded that this bicontinuous phase could be the transition phase, which co-exists between both the oil-in-water, and other phases [156].

The ternary diagram of soy lecithin was revised by answering the questions in Figure 2-26. The phase boundaries in the ternary diagram of DOPA were unchanged when compared with the visually developed ternary diagram (Figure 2-26 (C)). This is due to the charge differences between the DOPA and soy lecithin molecules. This bicontinuous region was missed with a visual observation. Addressing the specific set of

questions in Figure 2-25 revealed this transitional phase. The revised diagram (Figure 2-26 (D)) contains an additional bicontinuous phase where there is a transition from oil-in-water to water-in-oil.

In order to form the bicontinuous phase, a greater number of surfactant molecules, in comparison to oil-in-water, are required [52]. A charged head group, such as DOPA, has a smaller packing factor than its neutral counterpart. Therefore, DOPA reached its bicontinuous phase with a lower amount of surfactant than soy lecithin, which has a net zero charge on the head group. This proposal was further supported by the results of the visual inspection that showed a clear separation between two phases, while the soy lecithin system had no distinct boundary. Without a clearly defined boundary, further characterization, with more complex methods, was necessary for this study. After further testing with buoyant density, FT-IR, fluorescence quenching, and TEM, a bicontinuous phase was discovered in the soy lecithin system, labeled as AB in Figure 2-26 (D). Due to the packing factor theory [52], the differences between the phase behavior of DOPA and soy lecithin are displayed in Figure 2-26 (C) and (D), which showed a region 36 times broader for oil-in-water in the soy lecithin system.

2.5 Summary

The O/W phase was surveyed in this study. Even though the samples had the visual appearance of being suitable for the synthesis, testing various regions revealed that they did not meet the criteria: i.e., 1) does not contain excess liquid for efficiency, 2) efficiently uses immiscible liquids, 3) efficiently encapsulates oil, 4) protects from the surroundings, and 5) has a spherical shape). Even though the ternary diagrams demonstrated that the DOPA and soy lecithin emulsion systems had different numbers of

phases, both DOPA and soy lecithin systems showed one workable phase. The zwitterionic surfactant soy lecithin had a greater workable region for the oil-in-water phase than DOPA, which implies that soy lecithin is a more reproducible system and can be used for a product that is easily stable.

Table 2-1 The summary of the techniques with the purposes and methodology.

Techniques	Purpose	Method
Visual inspection	To observe the phases and boundaries in the given materials	The emulsion was synthesized via titration method and the number of layers in the samples was determined visually.
Buoyant density	To estimate how the oil and water are dispersed in the emulsion.	The weight of the emulsion was measured in a custom pycnometer designed to handle all phases, including gel and gel-like samples, easily.
Fluorescence quenching	To further support and disprove the proposed phase	The quenching effect of the fluorescence dye was monitored by fluorescence spectroscopy. Py dye was dissolved in PFOB, and KI in water, and the amount of quenching gives insight into the phase configuration
Fourier transform infrared spectroscopy	To quantitatively determine the amount of oil employed to form the emulsion	The amount of the oil in the emulsion was measured by infrared spectroscopy using the attenuated total reflectance sampling technique. From Beer's law the concentration of oil can be determined from the absorbance data. The amount of PFOB associated with emulsion was estimated by comparing the absorbance with that of pure oil.
Cryogenic transmission electron microscopy	To observe the morphology of the emulsion in each phase	The samples in each phase were frozen to form a thin ice film, which was observed by electron microscopy.

Table 2-2 The summary of the added materials to synthesize the various types of the emulsions.

Regions	Surfactant (w/w)	PFOB (w/w)	Water (w/w)
a	0.050	0.050	0.900
b	0.025	0.225	0.750
c	0.250	0.150	0.600
d	0.100	0.500	0.400
e	0.200	0.700	0.100
f	0.600	0.200	0.200

Table 2-3 Summary of the experimentally measured and the calculated densities. The results demonstrated how effectively the liquids were used in the emulsion formation.

Region	Composition (wt./wt.)			Measured density (g/mL)		Calculated density (g/mL)	Efficiency: formulation of emulsion (%)	
	Surfactant	PFOB	Water	DOPA	Soy lecithin		DOPA	Soy lecithin
a	0.025	0.025	0.950	0.998	0.999	1.010	98.4	98.2
b	0.025	0.225	0.750	1.003	1.007	1.123	89.3	89.7
c	0.375	0.025	0.600	1.002	1.005	1.017	98.5	98.8
d	0.025	0.575	0.400	1.125	1.180	1.395	80.6	84.6
e	0.875	0.025	0.100	1.006	1.101	1.105	91.0	99.6
f	0.025	0.875	0.100	1.156	1.004	1.761	65.7	57.0

Table 2-4 The summary of the shape characteristics found in the cryo-TEM micrographs. This table describes the types of shapes and the acceptance of the morphology according to the requirement of an encapsulated ring shape.

Synthesized regions	DOPA		Soy lecithin	
	Description	Acceptance	Description	Acceptance
Region a	Encapsulated ring shape with the consistent size	Yes	Encapsulated ring shape with the consistent size	Yes
Region b	Encapsulated ring shape; partially random shapes	Yes	Encapsulated ring shape; partially other shapes	Yes
Region c	Random shapes	No	Random shapes; Encapsulated ring shape	Yes
Region d	Random shapes	No	Encapsulated ring shape	No
Region e	Shape of a wave	No	Shape of a wave	No
Region f	Shape of a wave	No	Shape of a wave	No
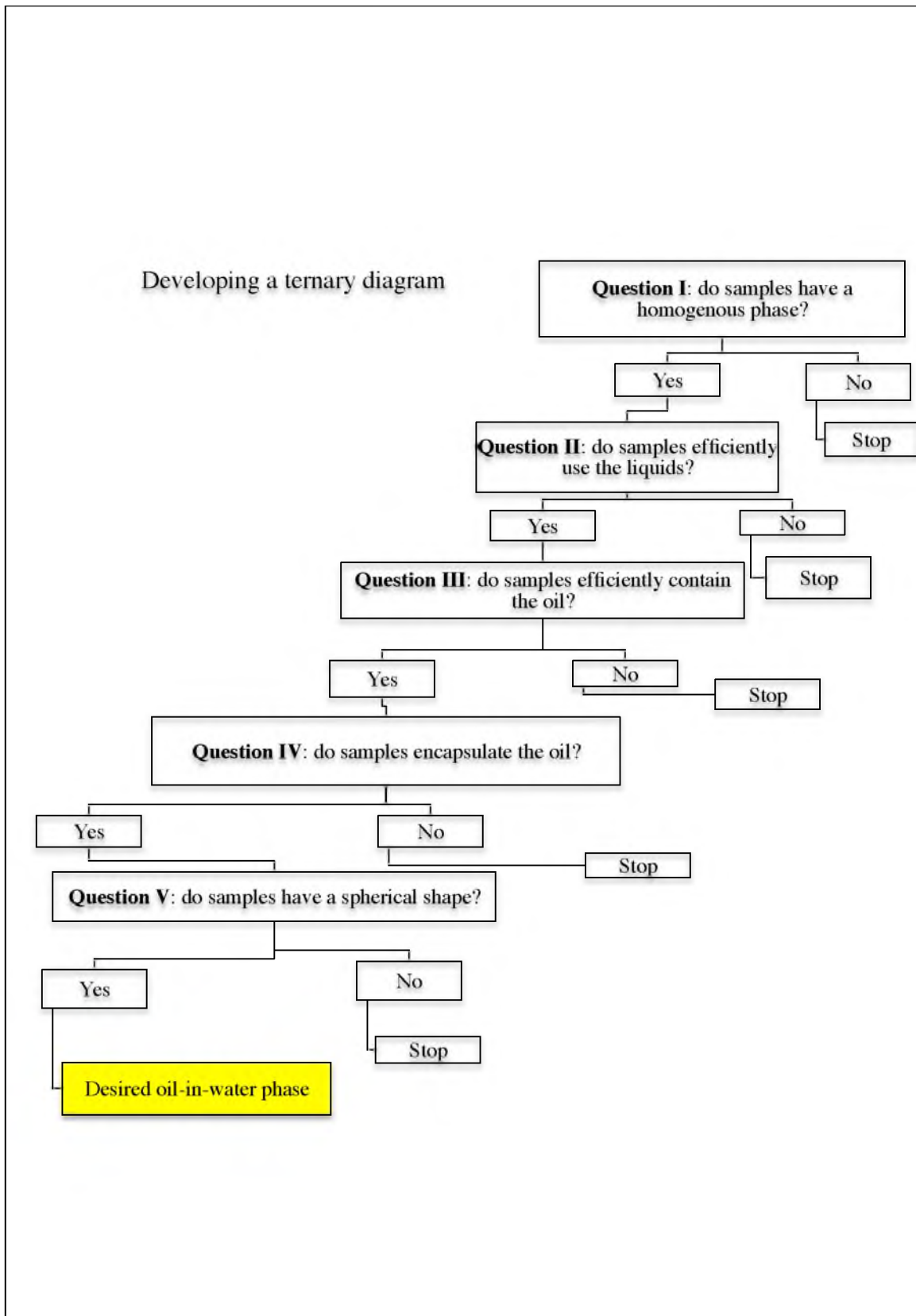
Figure 2-1 The flow chart to identify the desired oil-in-water phase.
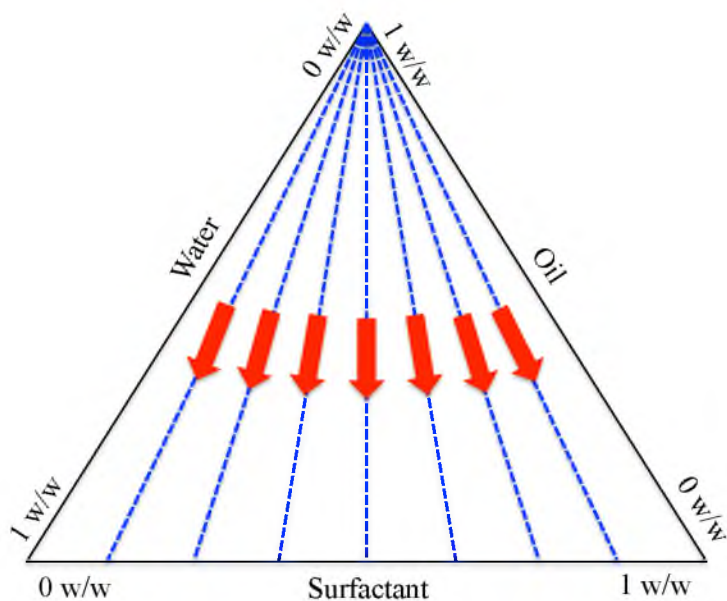
Figure 2-2 A schematic of the titration methods represents to construct the ternary diagram with the tie line (blue dash). Each side represents the respective element composition in weight fractions, which was increased from 0 to 1 w/w. For example, for a water titration the samples were synthesized by following the direction (red arrows) of low weight fraction of water to high.
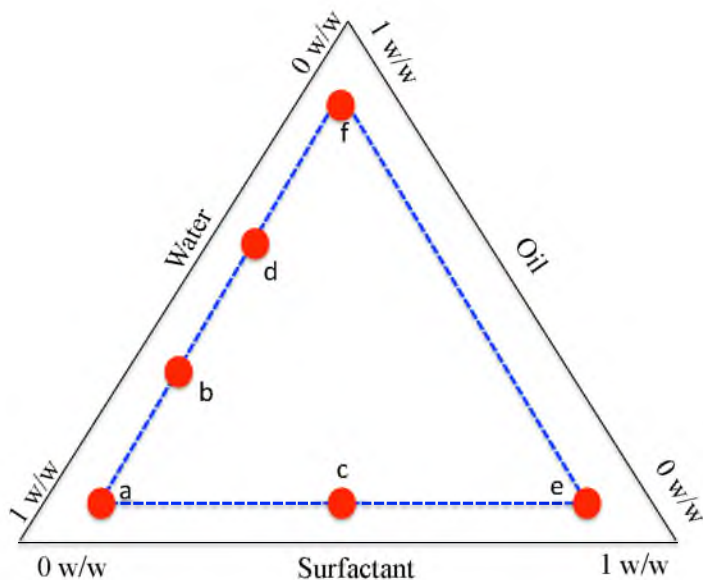
Figure 2-3 The ternary diagram with the selected regions (red dots) for characterization including buoyant density, fluorescence quenching, FT-IR, and cryo-EM. The line **a**, **c**, and **e** was parallel to the surfactant axis, and line **a**, **b**, **d**, and **f** was parallel to the water axis; the line formed by **e** and **f** were parallel to the oil.
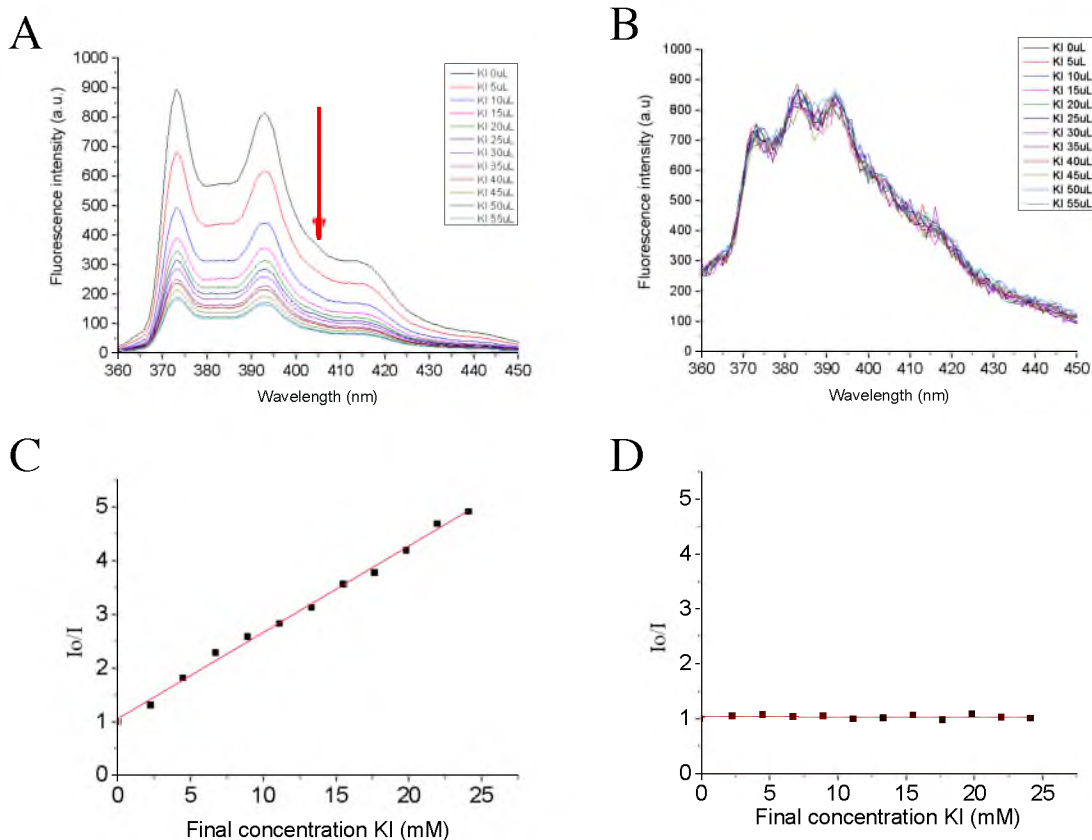
Figure 2-4 The raw data of the fluorescence by the pyrene. A) The pyrene (4.5 X 10^{-4} mM) was quenched by the quencher, KI, in water while B) it was not in the oil, PFOB. The wavenumber at 385 nm indicates the pyrene dissolved in PFOB. C, D) figures demonstrating that the pyrene in water was gradually quenched by KI while the oil had a constant fluorescence intensity. R-squared values for C) 0.9949 and D) 0.0045. Wavelengths analyzed C) 373 nm and D) 385 nm.
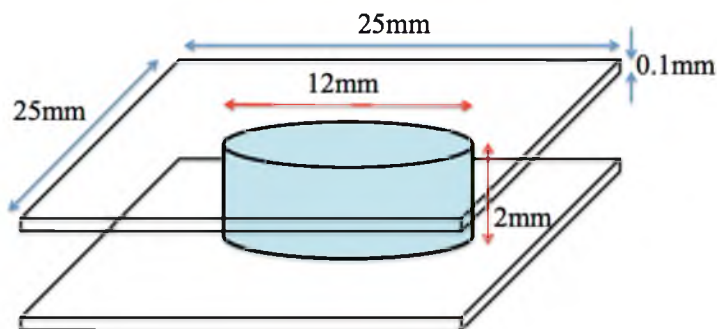
Figure 2-5 The schematics of the sample holder for the fluorescent measurement. The cylindrical shape holder (blue) was a rubber O-ring, and the ring was sealed with glass covers on both bottom and top.
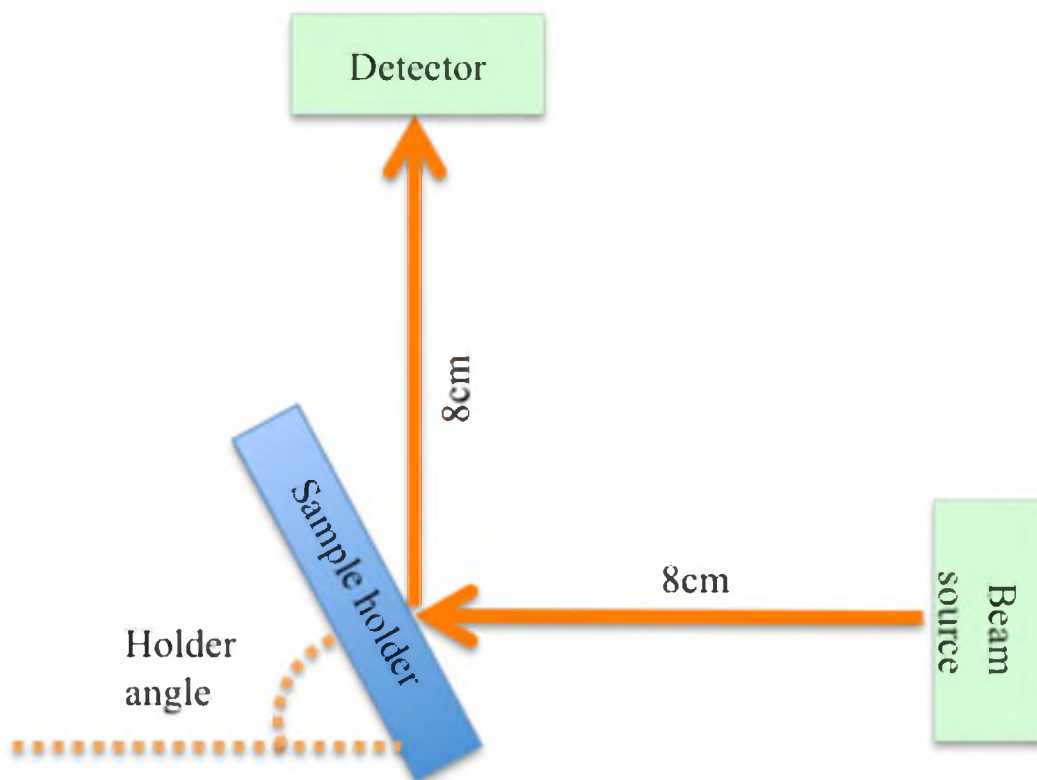
Figure 2-6 The block diagram of the front-face accessary position in the fluorescence spectrometer. The distance between the sample holder and the beam source was 8 cm. The angle of the sample holder was 62°.
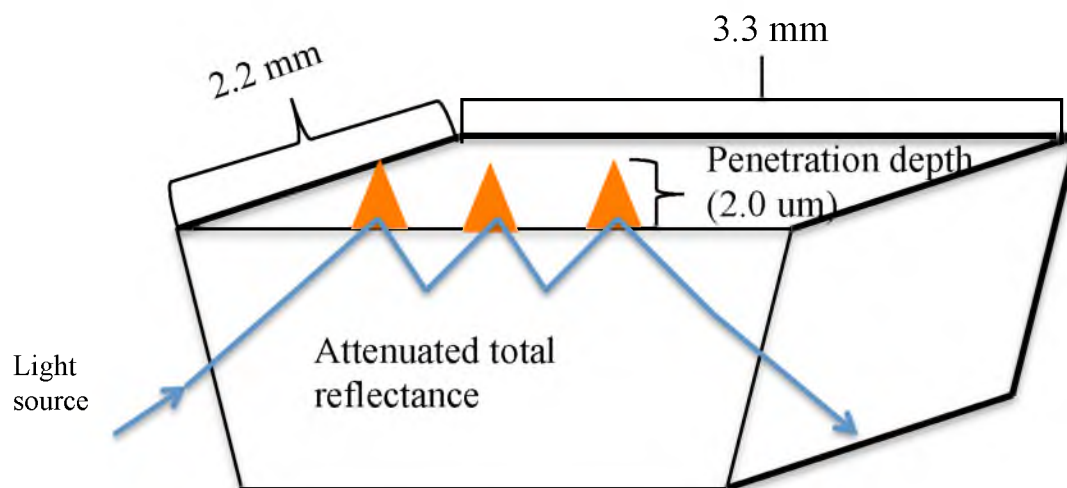
Figure 2-7 The schematics of the ATR cell. The dimension of the cell surface was 2.2 mm x 3.3 mm, and the penetration depth was 2.0 um [150].
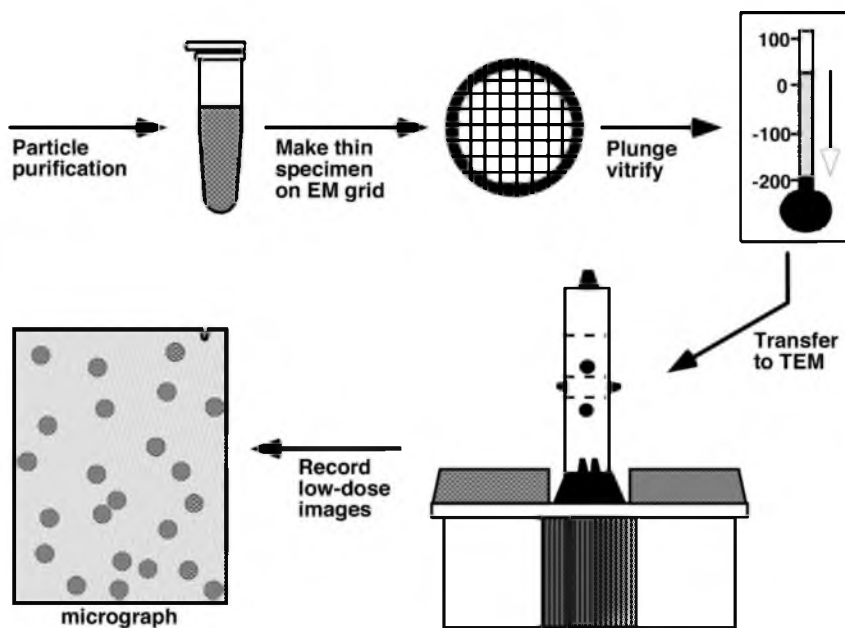
Figure 2-8 The schematics of the procedure: Cryo-TEM, adapted from [44]. The emulsion sample on the carbon grid was frozen in the thin ice by liquid nitrogen. The frozen sample was observed using the transmission electron microscopy.
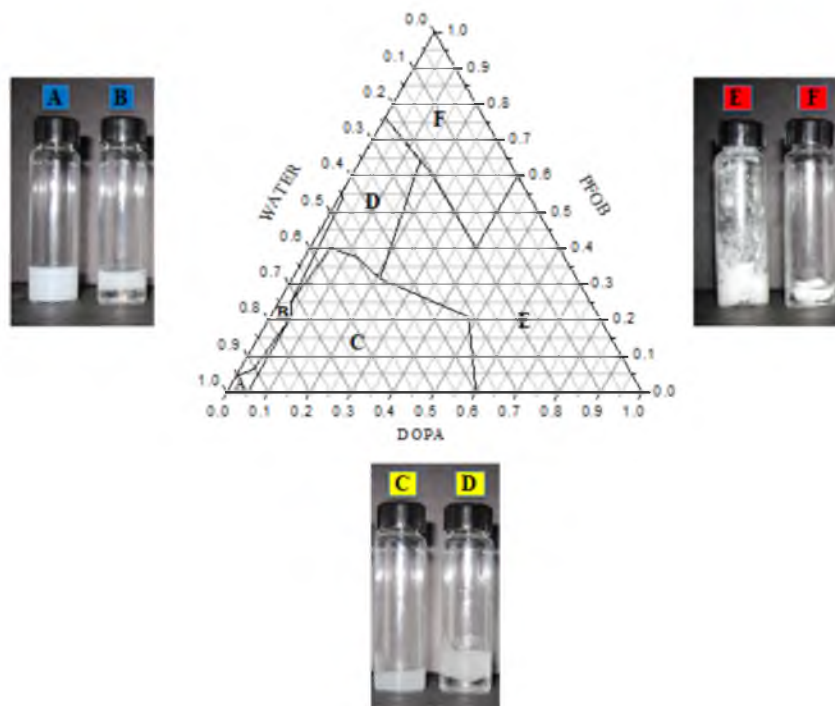
Figure 2-9 The ternary diagram of DOPA/PFOB/water. There were 6 various phases. The color of the samples was turbid or white, and some samples were viscous or had the excess liquid.
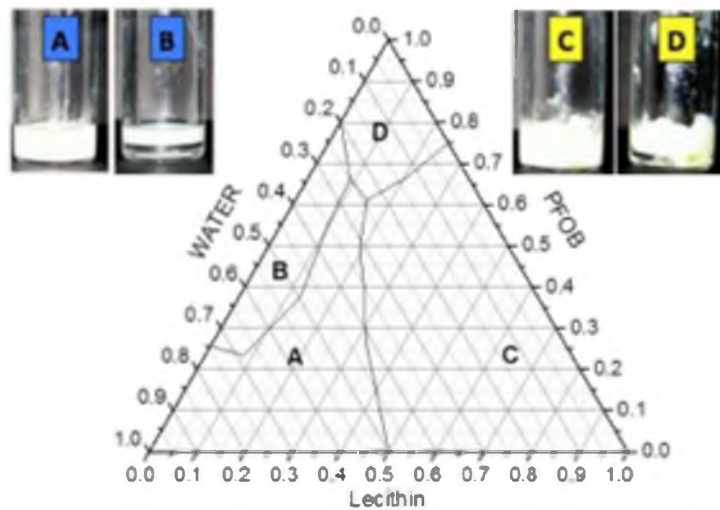
Figure 2-10 The ternary diagram of soy lecithin/PFOB/water. There were four various phases. The color of the samples was white, and some samples were viscous or had excess liquid.
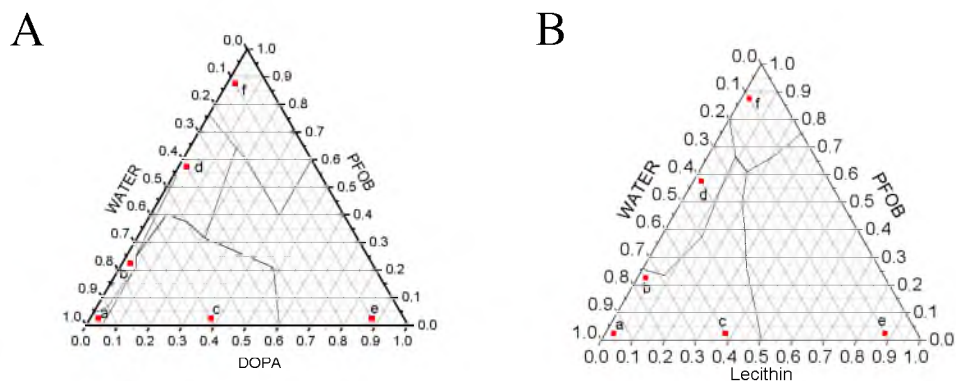
Figure 2-11 The ternary diagrams of A) DOPA/PFOB/water and B) lecithin/PFOB/water with the phase boundaries. The red dots represent the compositions to make the samples for the density, fluorescence quenching, and FTIR.
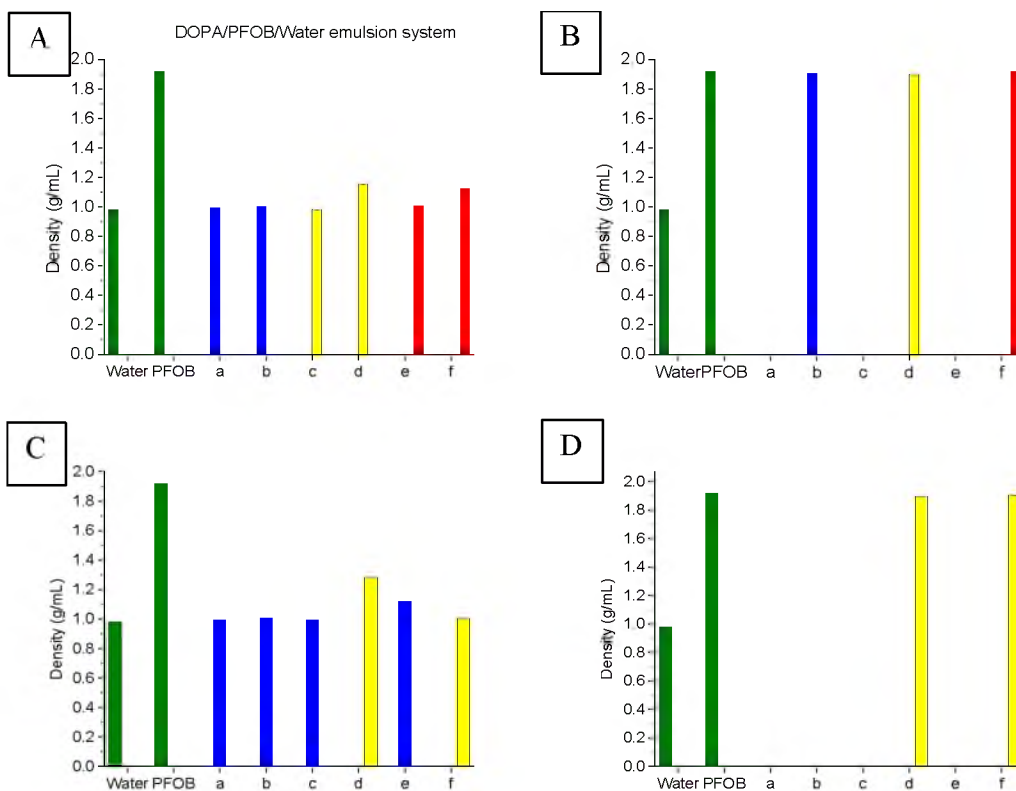
Figure 2-12 The measured densities of the DOPA and the soy lecithin emulsion systems. The synthesized regions in the DOPA emulsion system were measured by the customized pycnometer. A) represents the turbid suspension layer and B) the excess PFOB, verified by density measurements. The turbid layer in the soy lecithin emulsion system is shown in C) and the excess PFOB in D).
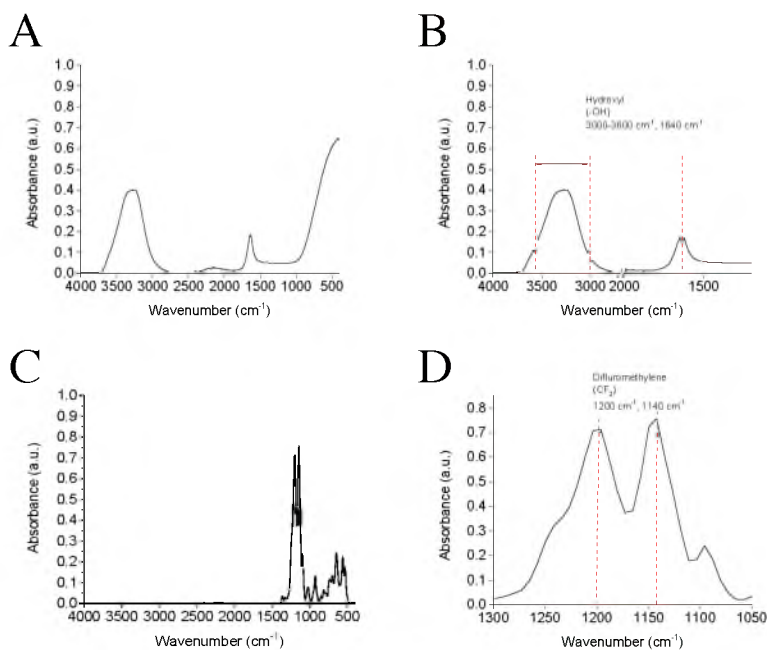
Figure 2-13 The FT-IR results of the control samples: water and PFOB. A) and B) Water demonstrated the hydroxyl group at 3000 - 3600 cm^{-1} (stretching) and at 1640 cm^{-1} (bending). C) and D) PFOB showed the difluromethylene group was the strongest intensity.
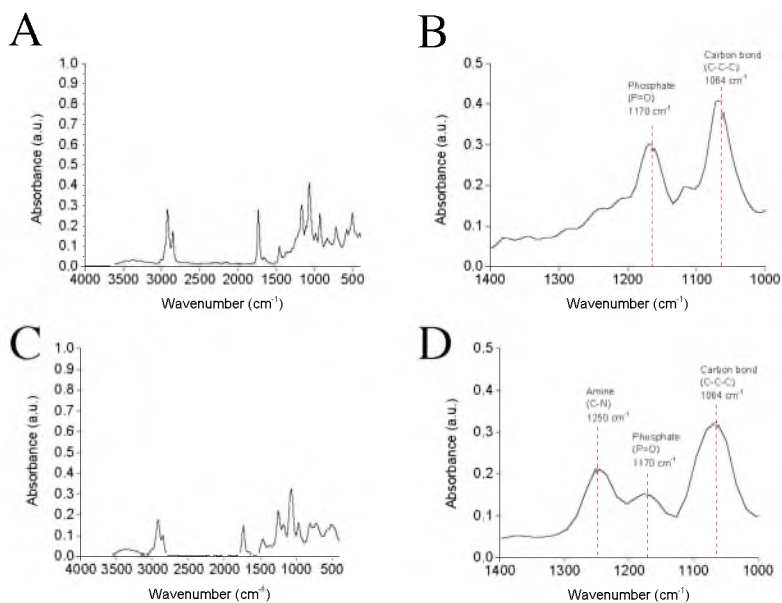
Figure 2-14 The FT-IR results of the control samples: DOPA (A and B) and soy lecithin (C and D). Both lipids (DOPA and soy lecithin) showed the phosphate at 1170 cm^{-1} and the three carbon bond (C-C C bending) at 1064 cm^{-1}. This carbon bond would be from ketone because both lipids had two ketone groups in the tail. Soy lecithin demonstrated the amine (C-N stretching) at 1250 cm^{-1}.
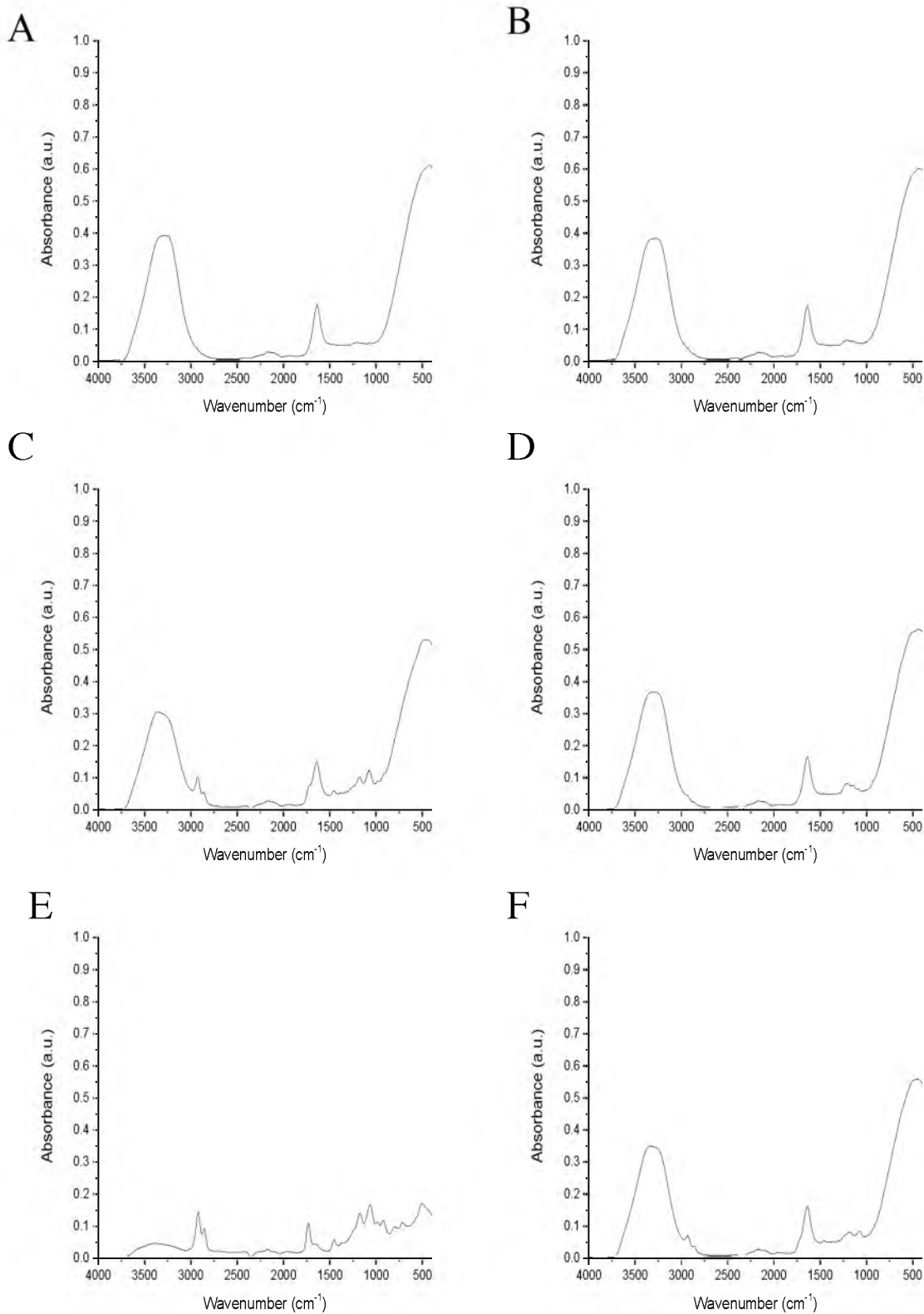
Figure 2-15 The raw data of the FT-IR in the DOPA emulsion system from A to F representing the same letter in the synthesized regions.

74
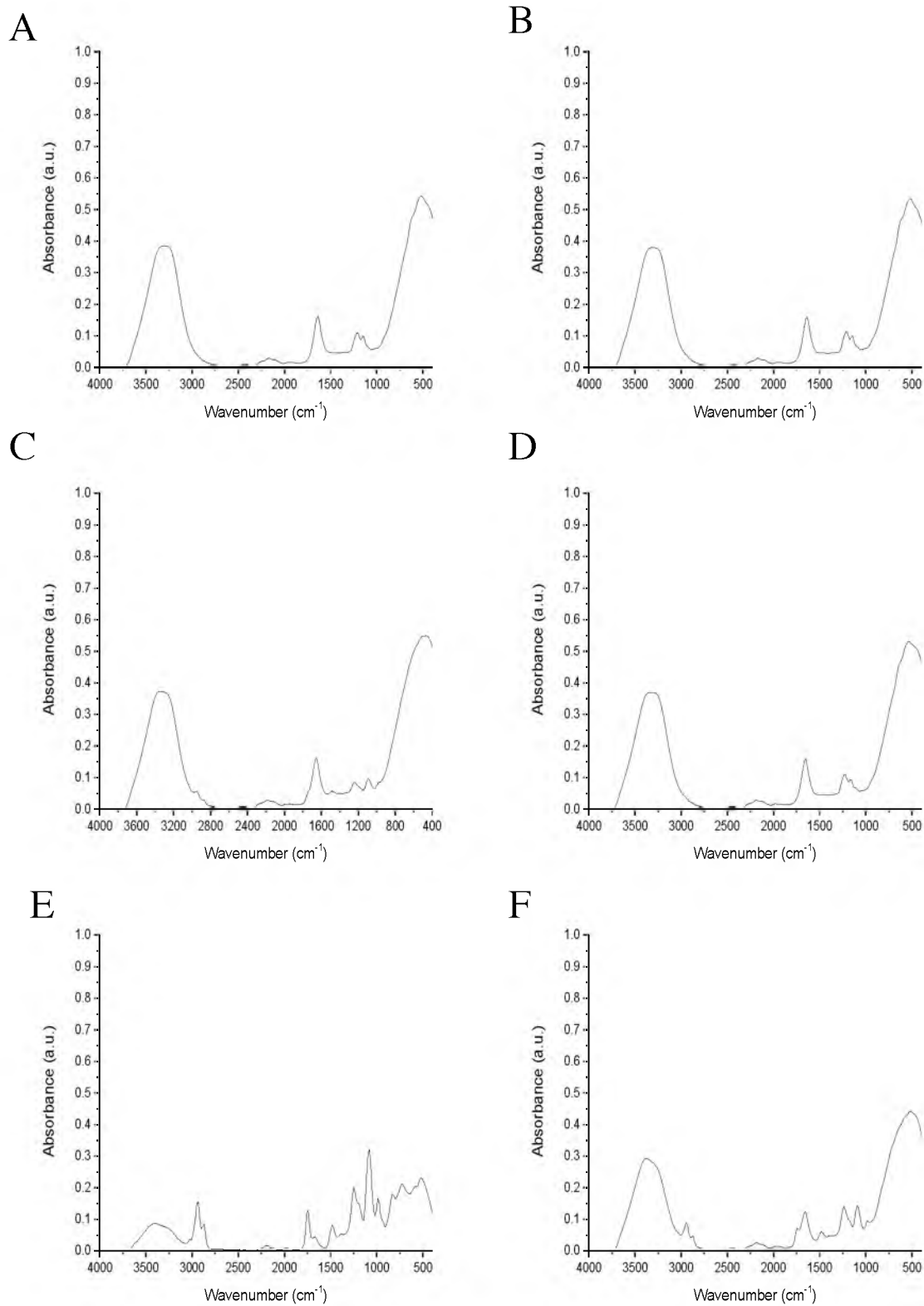
Figure 2-16 The raw data of the FT-IR in the soy lecithin emulsion system from A to F representing the same letter in the synthesized regions.
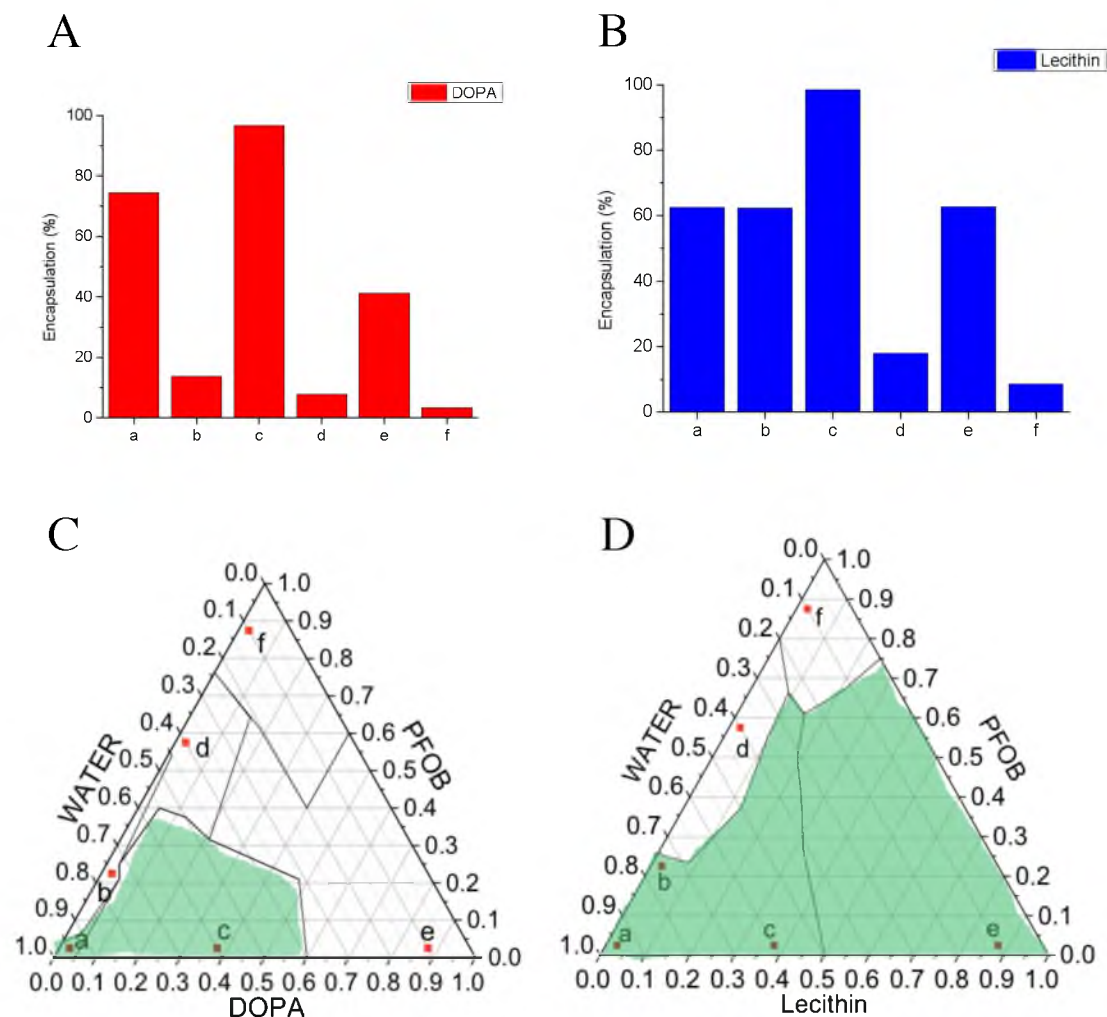
Figure 2-17 The calculated encapsulation of PFOB in the emulsion system. A) DOPA emulsion system demonstrated Region a and c encapsulate PFOB more than 50%, and B) soy lecithin emulsion system mostly encapsulates PFOB except Region d and f. C) and D) are the ternary diagrams of DOPA and soy lecithin. The green regions depict regions where there was efficient (greater than 50%) encapsulation of PFOB by the respective surfactant. Soy lecithin had the more effective encapsulation than DOPA.
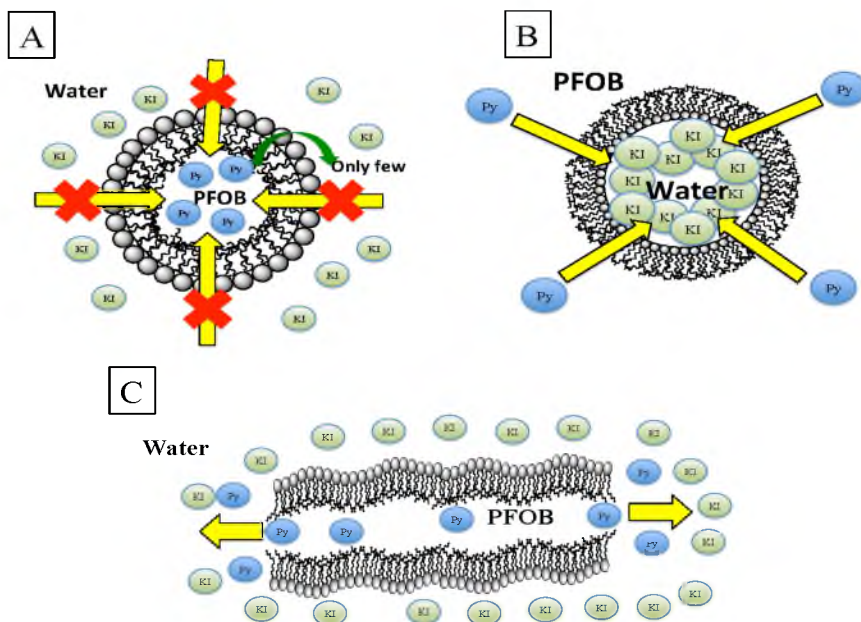
Figure 2-18 The schematic representing the initial idea for phases: A) oil-in-water (O/W), B) water-in-oil (W/O), and C) bicontinuous phases. The green and blue molecules indicate the quencher (KI) and the pyrene. A) Oil-in-water (O/W) phase: only a few of the dye molecules transport from the oil to the water across the lipid membrane. However, KI would not be transported into the emulsion because it is not soluble in the oil. B) Water-in-oil (W/O) phase: it would be difficult to be quenched by KI because the dye molecules would be easily trapped in the tails of the lipid molecules, and it is not soluble in the oil. C) Bicontinuous phase: because the oil phase is not encapsulated by the surfactant membrane the dye molecules are able to readily transport from the oil to the water where they are quenched by KI.
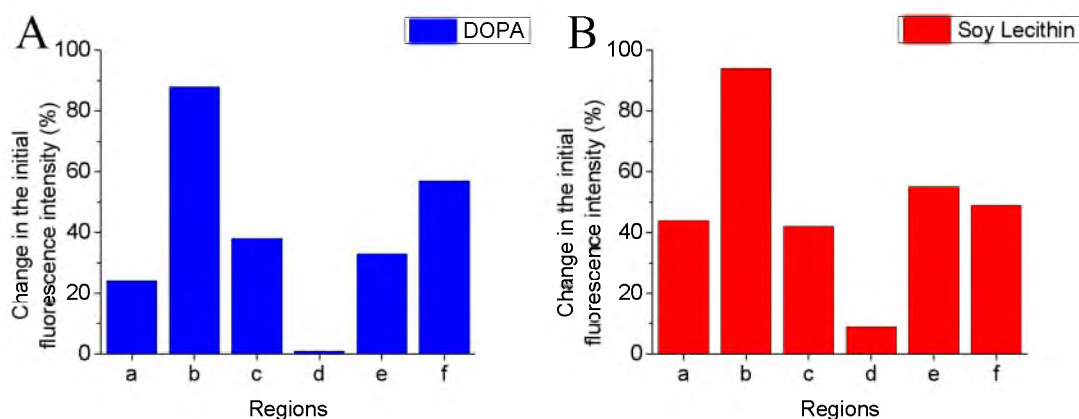
Figure 2-19 The change in the initial fluorescence intensity represented as a normalized percentage. Region b and d showed the maximal and minimal fluorescent quenching in both A) DOPA and B) soy lecithin. The DOPA system demonstrated the quenching in Region a (24%), b (88%), c (38%), d (1%), e (33%) and f (57%); the soy lecithin system is in Region a (44%), b (94%), c (42%), d (9%), e (55%), and f (49%).
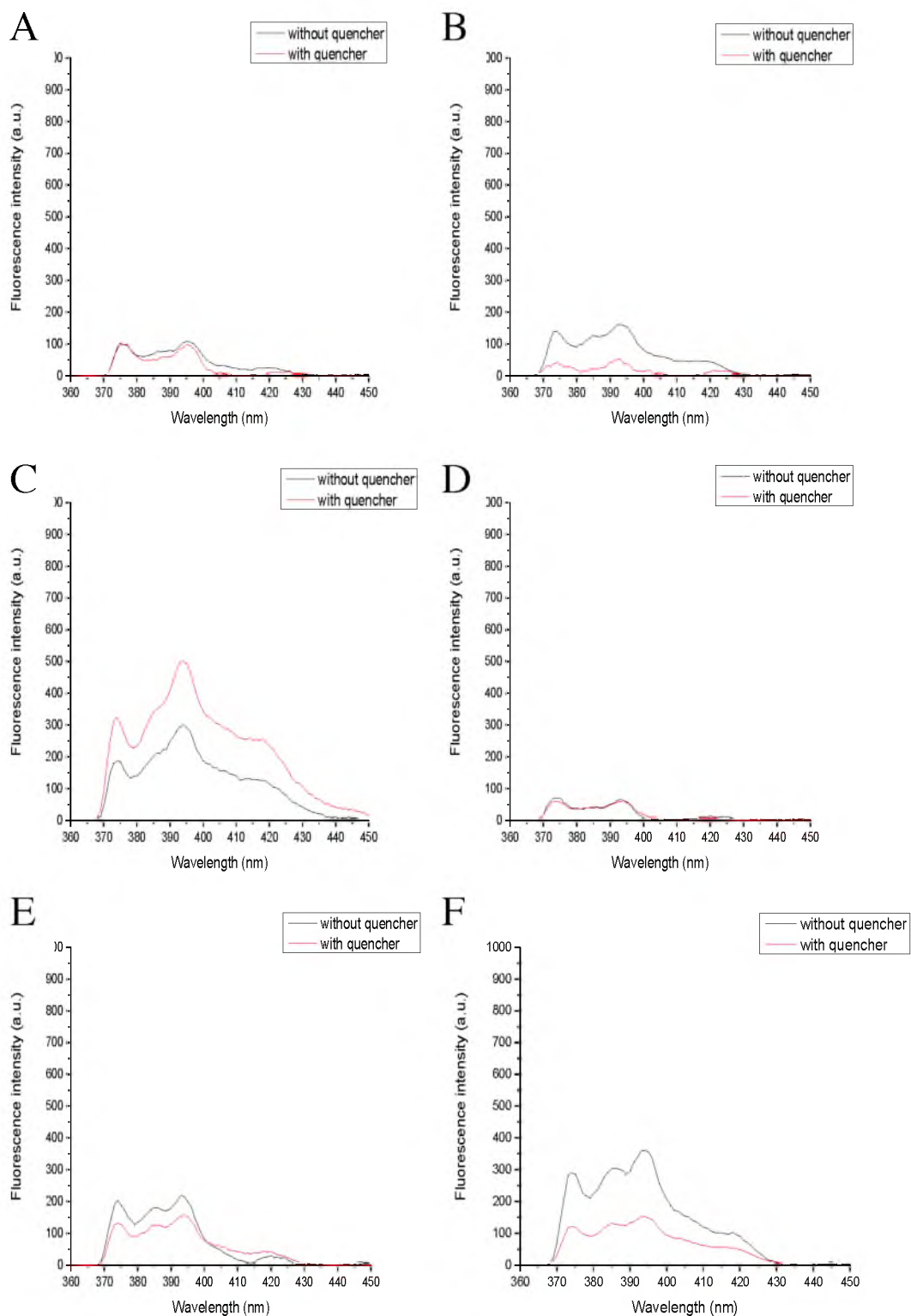
Figure 2-20 The fluorescence spectra of the DOPA emulsion system. The spectra at 385 nm showed the affects before and after adding the quencher. The labels represent the same letter of the synthesized regions.
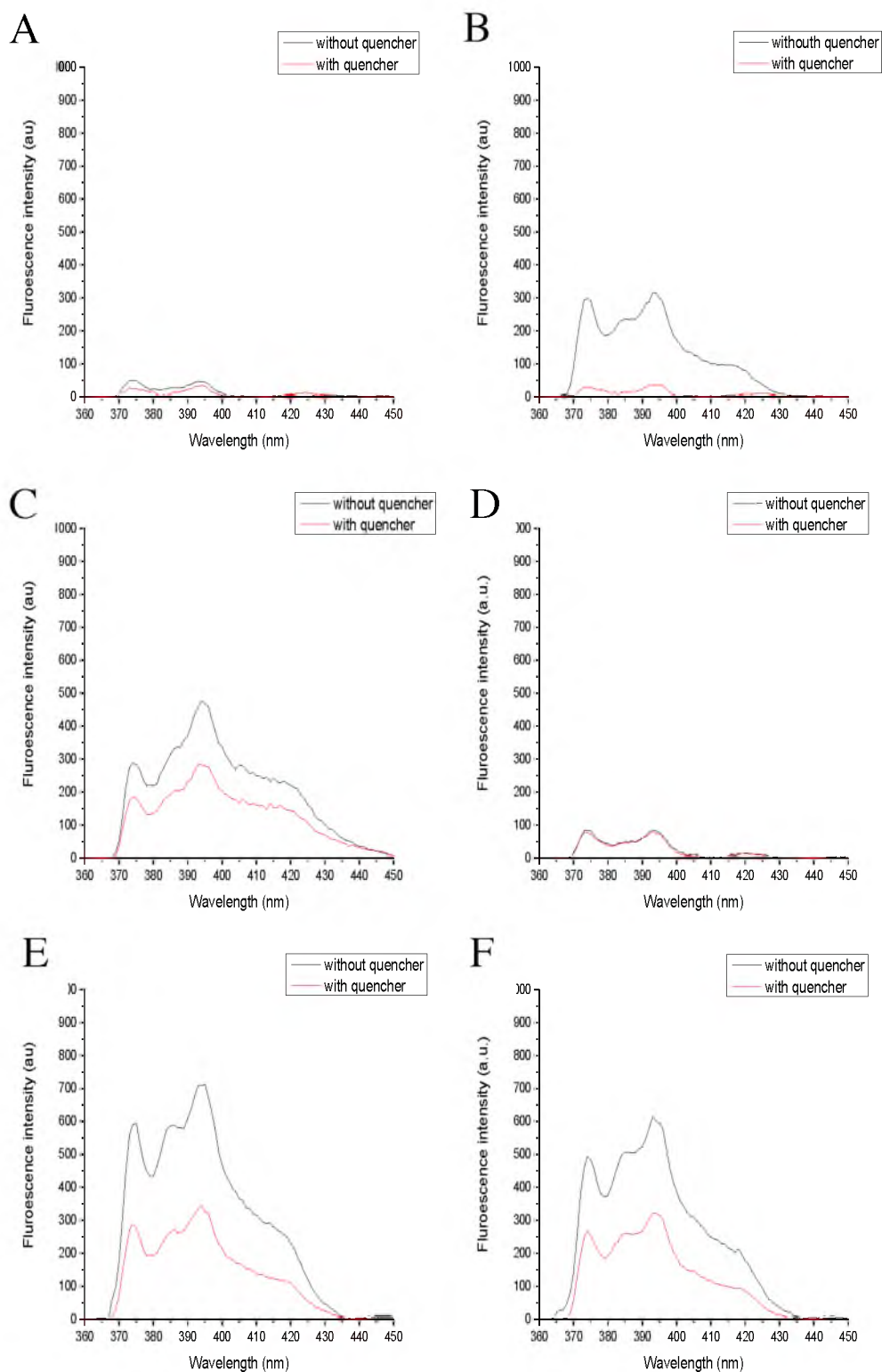
Figure 2-21 The fluorescence spectra of the soy lecithin emulsion system. The spectra at 385 nm showed the affects before and after adding the quencher. The labels are representing the same letter in the synthesized regions.
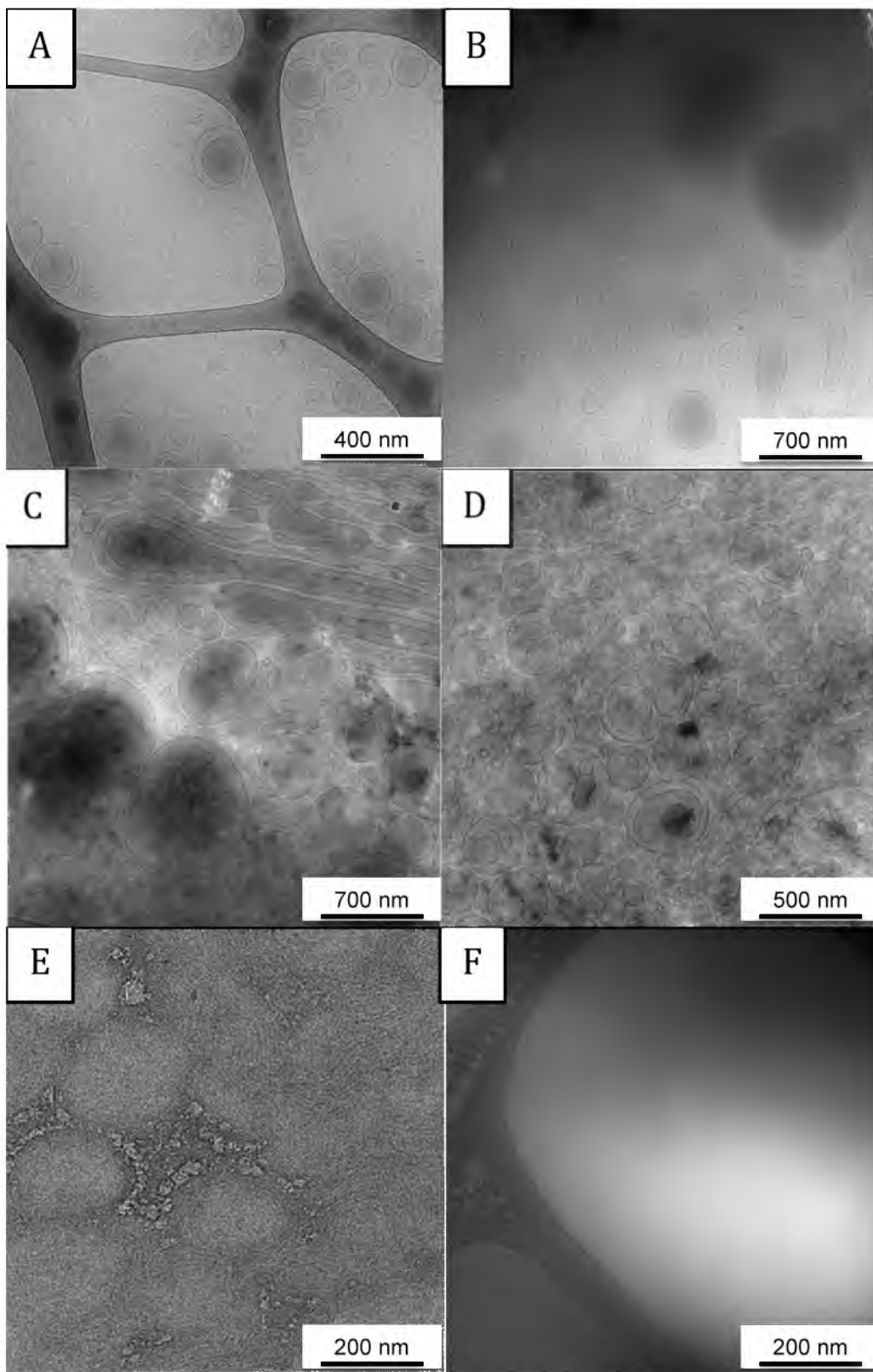
Figure 2-22 The cryo-TEM images of the DOPA emulsion system for each synthesized region from A to F represented by the same letter.

Figure 2-23 The cyro-TEM images of the soy lecithin emulsion system for each synthesized region from A to F represented by the same letter.
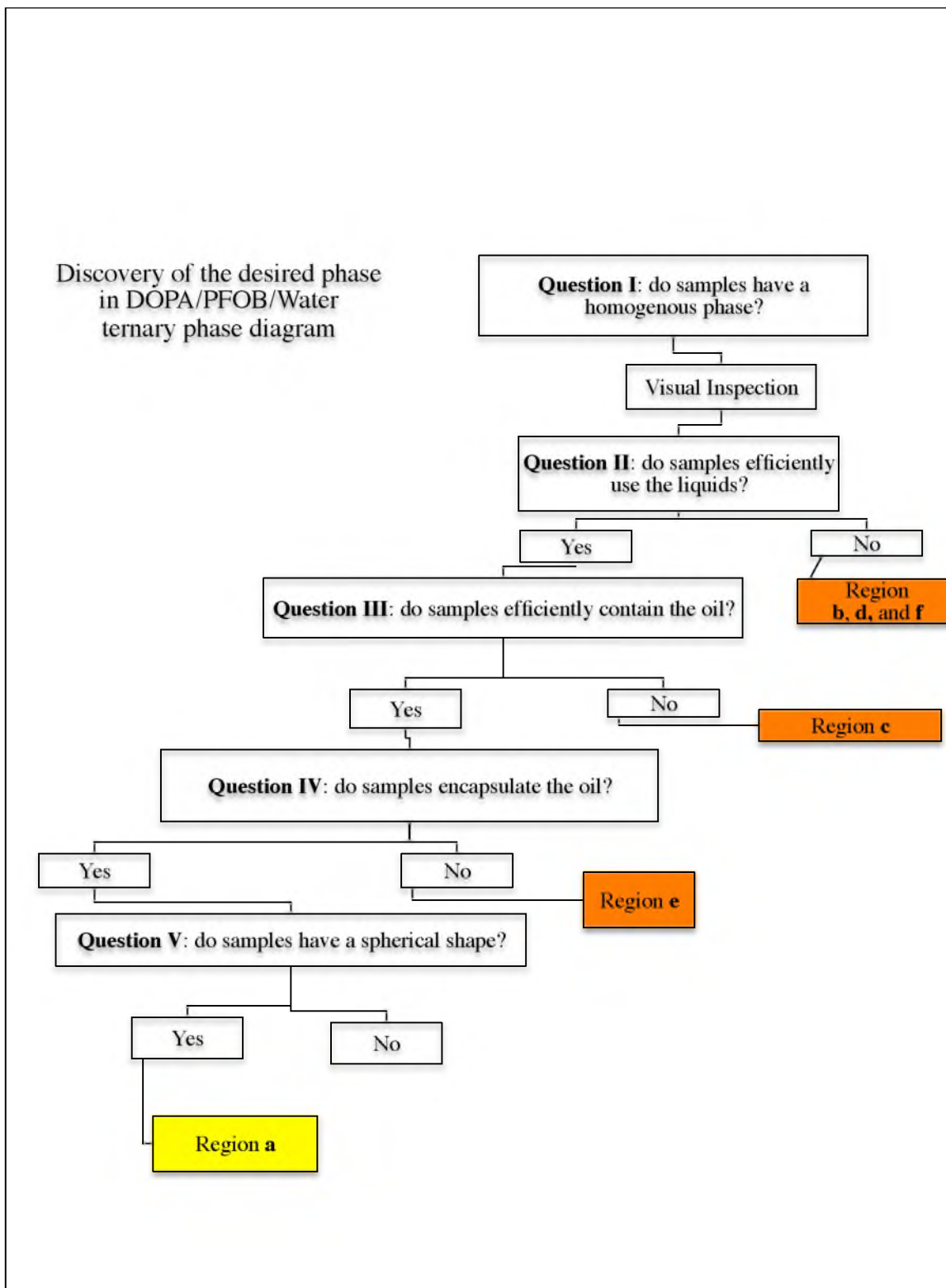
Figure 2-24 The flow chart used to find the desired phase in DOPA/PFOB/water ternary phase diagram. Employing the previous flow chart (Figure 2-1), each question was answered by characterizing the phases. Region **a** was the final desired phase in the DOPA emulsion system, and defined as oil-in-water.

Discovery of the desired phase in Soy Lecithin/PFOB/Water ternary phase diagram

Question I: do samples have a homogenous phase?

Visual Inspection

Question II: do samples efficiently use the liquids?

Yes

No

Region **d** and **f**

Question III: do samples efficiently contain the oil?

Yes

No

Question IV: do samples encapsulate the oil?

Yes

No

Region **b** and **e**

Question V: do samples have a spherical shape?

Yes

No

Region **a** and **c**

Figure 2-25 The flow chart used to find the desired phase in soy lecithin/PFOB/water ternary phase diagram. Employing the previous flow chart (Figure 2-1), each question was answered by characterizing the phases. Region **a** and **c** were the final desired phase in the soy lecithin emulsion system, defined as oil-in-water.
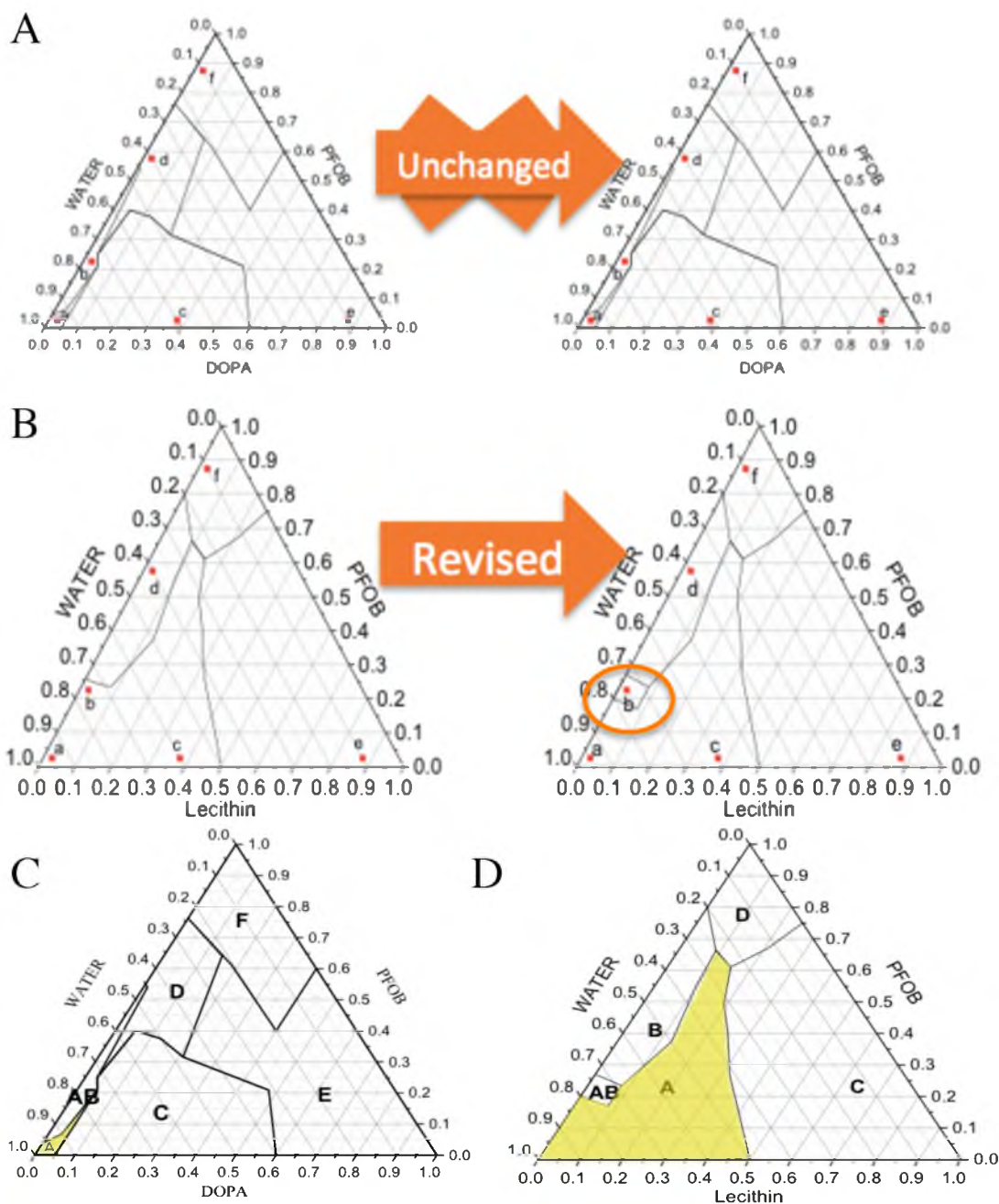
Figure 2-26 The ternary phase diagram of A) DOPA and B) soy lecithin. After characterizing each phase with buoyant density, FT-IR, fluorescence quenching, and TEM, the phase boundaries of the DOPA diagram were unchanged. Soy lecithin's diagram was revised after further characterization, with the addition of Region **b**. Region **b** in soy lecithin demonstrated the same phase behavior as Region **b** in DOPA. According to the fluorescence quenching results, this region transited from oil-in-water (Region **a**) to water-in-oil (Region **d**) in both systems. In the finalized ternary phase diagrams of C) DOPA and D) soy lecithin, the yellow phase, 36 times larger for the lecithin system, indicates the desired phase (oil-in-water) as A. The Phase (AB) is the transition phase between oil-in-water and water-in-oil phases, and is defined as the bicontinuous phase.

CHAPTER 3

CALCIUM PHOSPHATE COATING ON OIL-IN-WATER NANOEMULSION

AND PERFORMANCE OF STABILITY WITH OXYGEN RELEASE

AS OXYGEN CARRIER

3.1 Abstract

The focus of this study was to coat a nanoemulsion with shells of calcium

phosphate, of various thicknesses, and determine how the number of coating layers

affects the amount of oxygen released using a fast mixing method. The oil-in-water

emulsion consisted of soy lecithin, perfluorooctyle bromide, and water. Extrusion through

a submicron membrane was used to uniformly produce the particles, while also ensuring

monolayer phospholipid formation at the surface. The isoelectric point of the

nanoemulsion, defined as the pH at which the particle carries zero net charge, was found

to be at pH 9. At this pH, it was more favorable for the nanoemulsion to accept calcium

ions than its phosphate counterparts, which was confirmed with a Hill plot that showed an

association ratio of one calcium ion to one soy lecithin molecule. The coating was

constructed one layer at a time starting with the addition of calcium ions, followed by

phosphate, which constituted one layer of coating; repeating the process was said to form

the corresponding number of layers. The stability of the uncoated and coated emulsions

was then tested as a function of time with different physical and thermal conditions. The primary aim of the coated emulsion is to act as an oxygen carrier; thus, its oxygen release characteristics were measured by mixing the particles with deoxygenated hemoglobin. As the oxygen diffused out of the particles, it reacted with the hemoglobin and caused a spectroscopic change that was monitored with a stopped-flow apparatus. The pH of the solution determined the kinetic constant of hemoglobin, following the Bohr effect; otherwise, the lower the pH, the slower the oxygen uptake by deoxygenated hemoglobin. At a given pH, a thicker coating on the surface resulted in a slower oxygen release rate; for example, when shell thickness was increased from 0 nm to 38 nm, the kinetic constant was reduced from 2.8 sec^{-1} to 0.6 sec^{-1}. This suggests an inverse relationship between kinetic transfer and coating thickness.

In short, this study focused on the nanoemulsion coating and the measurements taken to evaluate its performance in oxygen release and stability. The coated emulsion was more stable than the uncoated one, but their oxygen release rates were reduced.

3.2 Introduction

This chapter focuses on coating the oil-in-water emulsion with calcium phosphate, a known biocompatible material [157-159], and describes measurement techniques for determining the amount of oxygen released from the particle. The calcium phosphate coating creates a rigid surface that protects the emulsion and improves its overall stability. The encapsulation technique used in this work has been implemented in other systems with biological applications, including drug delivery systems [160-164]. Calcium phosphate is a well-known ionic material found in the bone, but too much free calcium in blood can be toxic [165]. However, it is still a widely studied material among

drug delivery systems [166-170]. The emulsion was coated with calcium carbonate in powder form [171]. The advantage was that the product remained stable in long-term storage. The aggregated powder, however, was a challenge to resuspend in aqueous solutions. Both calcium phosphate and calcium carbonate are bioceramic materials, but relatively few studies have been completed on the toxicity of calcium carbonate [172-174], while calcium phosphate has been widely used in clinical studies due to its safety and simple production [165, 175-180]. Therefore, calcium phosphate material was selected as the coating material.

Oxygen release from the uncoated and coated emulsion [120] was measured by using the rival oxygen carrier, cell-free hemoglobin, as a reporter of oxygen exchange. The method using hemoglobin provided direct measurement by determining oxygen release. Furthermore, the fast mixing apparatus and the extremely high concentration gradient between inside and outside emulsion particles reduced the experimental time. Previously, the oxygen released from perfluorocarbon emulsion was measured using the gas-sparged oxygenator method, which takes a deoxygenated emulsion and monitors the change of oxygen in the solution [181]. The pathway for oxygen transfer starts in the gas phase, and then goes into the liquid medium, with a final destination inside the perfluorooctyl bromide (PFOB) droplet (Figure 3-1 and Figure 3-2). This method has many different variables and environments to consider, requiring the multiple assumptions listed as follows: 1) the oxygen transport affects the phase boundary formed at the interface between the surfactant and medium; 2) the emulsion particle is assumed to be uniformly distributed around the gas bubble within the bulk medium; 3) the loss of PFOB into the gas phase per pass through the gas-sparged oxygenator is neglected due to low vapor pressure; 4) the possibility of carbon dioxide being dissolved in the medium is

neglected; 5) the density of PFOB is assumed to be constant for the various concentrations of dissolved oxygen; and 6) the partial pressure of oxygen in the gas bubbles is constant.

The gas-sparged oxygenator method relies on a Clark electrode to monitor changes in the partial pressure of oxygen (Figure 3-3). However, there is a lag time that results from the limited diffusion of oxygen through the electrolyte, and probe membrane, before reaching the electrode surface. This, in combination with the many assumptions that needed to be implemented, ultimately resulted in inaccurate measurements and substantial uncertainty in system performance. Furthermore, the bubbling method was based on mass transfer, and it is limited to measuring only oxygen capacity with many inconvenient assumptions. The chemical kinetics provide a direct measurement of oxygen capacity and rate of release of oxygen without many assumptions.

After the emulsion had been coated with calcium carbonate and dried into a powder [171], there was still a problem with aggregation, which caused difficulties during re-suspension attempts. In order to prevent this problem, all of the processes, including the final product, ought to be well dispersed in a stable medium. The present study used the information from the ternary diagram generated in the previous chapter to determine the best composition for the desired phase and encapsulation properties. This approach has the following advantages: 1) minimizes the free surfactant, 2) maximizes the functional property, which is the amount of PFOB, and 3) optimizes the procedure by limiting the amount of excess materials. By understanding the ionic interaction with the emulsion surface, the optimal emulsion condition was found for proper coating formation. The zeta potential and Hill coefficient were the primary factors considered to understand this relationship.

In order to improve the previous oxygen measurement by Moolman, *et al* [181], this study used deoxygenated cell-free hemoglobin and a spectrophotometer to measure the oxygen released from the emulsion. Since the oxygenation of the emulsion does not necessarily have the same diffusion coefficient as the oxygen leaving the emulsion, the method described herein was viewed as a superior method to those previously implemented. Furthermore, the addition of calcium phosphate encapsulation of the emulsion, needed for *in vivo* applications, protected the emulsion from protein adsorption. Oxygen release from the coated emulsion was also measured utilizing the same method.

Measuring oxygen capacity of the particles was performed and verified with a specialized, liquid phase, dissolved oxygen probe with the bubbling method by Moolman, *et al* [181]. They measured the amount of oxygen loaded in the emulsion, which had a 200 nm diameter with 20 vol.% of PFOB, to be 3.7 mM while the theoretical oxygen for the same condition is 4.5 mM, see Appendix C. The experimental operation time was 12 minutes. The bubbling method had an error of 17%, and was not accurate enough to measure the oxygen capacity. This uncertainty is thought to be caused by free, excess, surfactant that has adsorbed onto the electrode surface, further hindering the diffusion of oxygen through the electrode interface. This also makes it difficult to estimate the diffusion coefficient of oxygen through the emulsion surface. The challenge, however, was to measure the kinetic rate of reaction of the oxygen released from the particle. Since the intended application will be *in vivo*, the emulsion particle will be competing with the red blood cell, which contains hemoglobin, a metalloprotein that transports oxygen to all cells in the body.

The rate of release was studied by simulating *in vivo* conditions using hemoglobin [182-186]. The studies used the red blood cells of chickens, ducks, and

humans. The kinetic rates of oxygen uptake by hemoglobin ranged between 2.4 to 3.8 s^{-1}. The results varied depending on the condition of the red blood cells, such as size. For the smaller diameter cells, the oxygen transfer conductance was smaller than its larger counterpart due to the ratio of surface area to radius.

However, in this present study, the experiment used a purified hemoglobin solution in order to prevent some of the common complications that are associated with the use of plasma or whole blood. Also, the particle size of the emulsion was constantly 280 nm in diameter. Hemoglobin is able to carry four oxygen molecules, but the rate constant will be different in each oxygen association. Simply put, the first oxygen is easier to load, while the fourth is the most difficult. Nevertheless, in order to maintain consistency and simplicity, only the first association of oxygen was considered. As mentioned in Chapter 1, a pseudo first order reaction was determined for this present study, and it is expressed as follows:

$$Hb + n \cdot O_2 \rightarrow HbO_2 \hspace{3cm} \text{Eq. 3-1}$$

where the Hb indicates deoxygenated hemoglobin, O_2 is oxygen, HbO_2 is the oxygenated hemoglobin, and n is the number of molecules; n was assumed to be 1 in this study because only the first oxygen association was considered. The reaction was a first order derivative.

This study presents the synthesis of an oil-in-water nanoemulsion taken from the ternary diagram in Chapter 2 and optimized for stable calcium binding on its surface. After the calcium phosphate coating was deposited its stability was determined in conditions similar to common storage and *in vivo* use. Finally, the release of oxygen was evaluated using the fast mixing, reaction monitoring method.

3.3 Materials and Methods

3.3.1 Calcium Phosphate Coating

3.3.1.1 Synthesis of the Nanoemulsion in Oil-in-water Phase

The materials, soy lecithin (500 mg), PFOB (0.7 mL), and water (7 mL), described in Figure 3-4 (A) were added to a 20 mL glass vial, and the mixture was stirred at 1200 rpm for 30 minutes at room temperature. Using this methodology, the mixture was extruded seven times at 150 psi through a 200 nm pore size membrane (Millipore polycarbonate extrusion filter with a 25 mm diameter, Millipore, Billerica, MA) in a 10 mL Thermobarrel LIPEX extruder (Northern Lipids, Burnaby, BC, Canada). Optical microscopy (Olympus IX71, Olympus America Inc., Melville, NY) was used to characterize the unextruded and extruded samples with bright-field and cross-polarized light illumination with 200× magnification. Fourier transform infrared spectroscopy (FT-IR) (Varian 3100 FT-IR, Varian Inc., Palo Alto, CA) was also performed to determine the amount of PFOB lost during the extrusion process. As described in the Fourier transform infrared spectroscopy characterization in Chapter 2, the attenuated total reflectance (ATR) (MIRacleTM Single Reflectance ATR, Pike Technologies, Madison, WI) sampling method was utilized in FT-IR. A volume of 10 uL was dropped onto the ATR surface, and 150 measurements were obtained with a resolution of 4 cm^{-1}.

Different amounts of soy lecithin were combined with PFOB and water to find the oil-in-water region, shown in Figure 3-4, B; all samples were extruded through the 200 nm pore size membrane by seven passes at 150 psi, and the particle size was measured by dynamic light scattering (DLS, Zetasizer Nano ZS, Malvern Ltd., Worcestershire, UK). The volume of the sample used in DLS was 1 mL, and it was measured in a UV-transparent plastic microcuvette (Disposable Micro Cuvette, ZEN0118, Malvern Ltd.,

Worcestershire, UK). The excess PFOB was determined by loading a pipette tip (either

10 uL, 200 uL, or 1000 uL capacities) and measuring its contents, as seen in Figure 3-5.

3.3.1.2 Constructing the Calcium Phosphate Coating

3.3.1.2.1 pH Titration

This experiment was to determine optimal pH under which the emulsion particles

were fully dispersed due to the highly repulsive surface charge. Two milliliters of the

nanoemulsion made with the optimal composition from the previous section 3.2.1.1 was

titrated from pH 11 to 2 with hydrochloric acid (HCl, 0.1 M). The relationship between

pH and zeta potential was monitored with a microcuvette (Disposable Micro Cuvette,

ZEN0118, Malvern Ltd., Worcestershire, UK) and the zeta potential cell (Disposable

Capillary Cell, DTS1070, Malvern Ltd., Worcestershire, UK).

3.3.1.2.2 Affinity of Calcium and Phosphate Ions

A titration method was utilized to understand the ionic affinity between calcium,

phosphate, and the emulsion surface. The nanoemulsion (2 mL) was, again, prepared with

the same optimal condition from section 3.3.1.1, and the pH was adjusted to 9 with NaOH.

Calcium chloride ($CaCl_2$, 3.0 mM, pH 9) and phosphoric acid (H_3PO_4, 3.0 mM, pH 9)

were separately titrated into the emulsion suspension, and the change in surface charge

was used to describe the binding affinity of ions to the particle surface. Zeta potential was

used at each point in the titration to characterize this surface affinity.

3.3.1.2.3 Calcium Ion Cooperative and Binding Constant to

Emulsion Surface

The results described in section 3.3.1.2.2, it was concluded that the emulsion had

a higher affinity for the calcium ion than the phosphate ion. These results determined the

binding constant of calcium ions to the emulsion surface, with the assumption that all of

the added soy lecithin was utilized to form the nanoemulsion. The $CaCl_2$ solution (10 mL,

3 mM, pH 9) was titrated by the emulsion solution with soy lecithin (1.4 mM, pH 9) using

the mixing and extruding methods as mentioned in section 3.3.1.1, where the emulsion

preparation was described. The free calcium was measured by using a calcium ion

selective electrode (Calcium ionplus® Sure-Flow® Plastic Membrane Combination,

Thermo Scientific, Waltham, MA). In order to develop the calibration curve for the

electrode, a serial dilution was employed to set a standard range from 10^{-1} M to 10^{-4} M

(Figure 3-6). The calcium standard ($CaCl_2$, Thermo Scientific, Waltham, MA) used was

0.1 M, and the following relationship was applied to the electrode [128]:

$$C_1 \times V_1 = C_2 \times V_2 \hspace{2cm} \text{Eq. 3-2}$$

where C_1 and V_1 were the concentration and the volume of the original standard, and C_2

and V_2 were the concentration and the volume of the standard after dilution.

3.3.1.3 Synthesis of Calcium Phosphate Coating

An emulsion of the optimal composition (15 mL) was coated with a thin shell of

calcium phosphate. The concentration of ions used in the coating process was determined

by the amount of soy lecithin, with a final 1:1 molar ratio between calcium ions and soy

lecithin molecules. Calcium chloride (1.4 mM, pH 9) and phosphoric acid (1.4 mM,

pH 9) were prepared as the stock solutions and added to 15 mL of emulsion in the following manner: First, the emulsion was stirred at 400 rpm at room temperature, then 1.5 mL of the stock calcium solution was added to the solution. After 30 seconds, another 1.5 mL aliquot of the calcium solution was added to the mixture, and the process was repeated until a total of 15 mL had been mixed in. The emulsion, with calcium ions, was stirred at 400 rpm for 10 additional minutes to ensure association. Then, the same process was repeated with the phosphoric acid solution, after which, stirring continued for 10 more minutes to ensure even distribution throughout. The process of adding calcium and phosphate with 10-minute buffer intervals was defined as one coating; hence, if more coatings were desired, the process could be repeated for the appropriate number of coating layers. For each coating layer, the zeta potential of the sample was monitored to verify that the added ions (calcium and phosphate) were actually binding to the surface. The synthesis of calcium phosphate coating on the emulsion is described in Figure 3-7.

Once the coating process was completed, the mixture was dialyzed for 3 days against deionized water, with a 3,500 MWCO (VWR Scientific, Radnor, PA) membrane, to remove free ions in the solution. After dialysis, the concentration of PFOB was lower than the original emulsion solution (2 vol.% of PFOB) due to dilution with calcium and phosphate solutions; thus, the suspension was concentrated back to the original concentration using tangential flow filtration (TFF) (KrosFlo® Research lli Tangential Flow Filtration System, Spectrum Laboratories, Inc., Rancho Dominguez, CA). TFF is an ultrafiltration method that is able to remove water and ions from the sample. The polyethersulfone hollow fiber membrane (Spectrum Laboratories, Inc., Rancho Dominguez, CA) had a 100 kDa MWCO, with a surface area of 115 cm². Finally, the particle size was measured with DLS.

3.3.1.4 Visual Chacterization of Calcium Phosphate Coated Emulsion

The nanoemulsion was imaged under TEM with a negative stain method, which protected the fragile emulsion from the vacuum environment and high-energy electron beam. To prepare the sample for viewing, uranyl acetate (2% or 47 mM, 10 uL) was mixed with an equal amount of the sample, and a drop of this mixture was placed on a TEM grid and left for 20 seconds. The entire solution was removed using filter paper, and the grid was air dried for 30 minutes.

The uncoated emulsions were thought to be considerably less robust, thereby making the negative staining method necessary. Therefore, samples were simply prepared by placing 2 uL of each sample onto separate TEM grids, and allowing them to air dry overnight. The samples were observed under a FEI Tecnai™ TEM (FEI, Hillsboro, OR) at 80 keV.

3.3.2 Method: Performance of Calcium Phosphate Coated Nanoemulsion

3.3.2.1 Stability in Practical Conditions

The stability of the phosphate coated emulsion was tested under three different conditions. First, the suspension was sterilized with an autoclave, then kept at room temperature. Second, the sample was simply stored on a platform shaker at room temperature, and the final condition was storing the suspension statically, in the dark, at room temperature. Stability was monitored by tracking the particle size as a function of time. The samples were steam autoclaved at $120^{\circ}C$ with an average pressure of 29 psi (SE 510, Yamato, Santa Clara, CA). The sample (2 mL) was added to a 2 mL vial, and filling the vial to the top eliminated any headspace and the possibility of a reaction caused by gaseous pressure. A 2 mL vial was completely filled with the sample and mixed on a

platform shaker. The stability, monitored by DLS measurements, was evaluated at 15-minute intervals for a total of 150 minutes. Lastly, the samples were stored at room temperature, in the dark, for 50 days, with a measurement interval of a few days. Table 3-1 summarizes the methodologies.

3.3.2.2 Oxygen Release as an Oxygen Carrier

3.3.2.2.1 Experimental Preparation

The Aminco-Morrow Stopped-Flow Apparatus (Cat. No. 4-6412, American Instrument Co., Inc., Silver Spring, MY) was used, in combination with a spectrophotometer (serial number 2799, Beckman, National Technical Laboratories, South Pasadena, CA), to observe the reaction rate of the two samples. The pistons used to inject the sample, and deoxygenated hemoglobin, were simultaneously driven by an air-operated plunger at 40 psi. The spectrometer set up had a slit at 0.82 mm for a wavelength of 550 nm, for observing the spectroscopic change of deoxygenated hemoglobin. The unshielded connector block (model NI CB-68LP, serial number CF315C, National Instruments Co., Carlsbad, CA) was used as the interface, and the results were recorded using LabView software (version 6.0, serial number G11X87212, National Instruments Co., Carlsbad, CA).

Four measured voltages from the spectrophotometer were used as reference points to estimate the oxygen content: 1) 100% light transmittance, 2) 0% light transmittance, 3) the deoxygenated hemoglobin (Hb), and 4) the oxyhemoglobin (HbO_2) transmittances. The working window was between the Hb and the HbO_2. When the Hb was mixed with the sample, the Hb absorbed the oxygen released from the sample,

transforming it into HbO_2, which was then used to calculate the concentration of oxygen originally in the sample. A detailed calculation process is presented in Appendix B.

In order to determine the oxygen release from the samples, hemoglobin collected from red blood cells was deoxygenated by nitrogen gas purging. Then, the deoxygenated hemoglobin was mixed with the samples in the stopped-flow apparatus. Table 3-2 simplifies the entire procedure for the reader's convenience.

In order to collect and deoxygenate hemoglobin, it was obtained from donated red blood cells, defined as "Collecting hemoglobin" in Table 3-2. The packed red blood cells (RBC) were obtained from the University Hospital Blood Bank at the University of Utah and hemolyzed. However, the blood was first washed by taking 5 mL of RBC and adding it to 45 mL of normal saline (150 mM sodium chloride (NaCl)). It was centrifuged in a 50 mL conical tube at 750 × g for 5 minutes using a centrifuge (Legend X1R, Thermo Scientific, Waltham, MA). The supernatant was removed by pipette and discarded. The tube was again filled with saline, the RBCs resuspended, and the process was repeated twice. Once the wash was completed, the RBCs were hemolyzed with a hypotonic phosphate buffer (5 mM, pH 7.4), bringing the volume up to 45 mL. The tube was centrifuged at 4000 × g for 30 minutes, and the hemoglobin containing supernatant was collected.

In order to find the concentration of the hemoglobin, the collected hemoglobin (0.05 mL) was diluted in the phosphate buffer (1.95 mL, pH 7.2). The absorbance of the sample was measured with a UV-Vis (Cary 100, Agilent Technologies, Santa Clara, CA), and the concentration (c) of the collected hemoglobin was calculated using Beer's law:

$$A = \varepsilon bc \qquad\qquad\qquad \text{Eq. 3-3}$$

where A was the measured absorbance, and the extinction coefficient (ε) of one heme group in hemoglobin was 55.2 mM^{-1}cm^{-1} at 541 nm [187], and the path length (b) of the quartz cuvette was 1 cm.

It is important to note that the concentration of the stock hemoglobin solution was too high to be accurately measured, so it was diluted 40 times. Thus, the concentration obtained from Eq. 3-3 was 1/40th of the actual value. The hemoglobin solution was then diluted to the desired concentration with the phosphate buffer.

Second, nitrogen purging, represented in Table 3-2 as "Deoxygenating hemoglobin," deoxygenated the collected hemoglobin. To monitor the concentration of oxygen dissolved in the hemoglobin solution a Clark electrode was used, along with a high sensitivity Teflon membrane with 5 um thickness (model 5776, YSI Inc., Yellow Springs, OH). The probe was calibrated by bubbling deionized water (60 mL) with nitrogen gas (95 mol.%) balanced with carbon dioxide (5 mol.%), during which the oxygen level was normalized to 0 %. Next, oxygen gas (25 mol.%) balanced with nitrogen gas (75 mol.%) was bubbled through, and the oxygen level was normalized to 25 %, properly establishing an upper oxygen limit. This process was repeated three times to ensure precise readings. Once the calibration was completed, the flask was emptied, and then assembled without the input gas tube, as described in Figure 3-7. Then, the collected hemoglobin (60 mL) was added to the flask through the sample valve, and the nitrogen gas was blown into the headspace until the voltammeter showed zero. The deoxygenated hemoglobin was extracted via the sample valve using a 10 mL syringe.

3.3.2.2.2 Control Experiments

There were two control experiments needed for accurate measurement of the oxygen parameters: 1) the limitations of the detector, determined by a serial dilution of deoxygenated hemoglobin and 2) establishing a new baseline for the effects of turbidity in coated and uncoated emulsion samples.

First, a spectrophotometer control test was performed to find the machines detection limitations. For the first control experiment (limitations of the detector as measured by deoxygenated hemoglobin), deionized water (60 mL) was deoxygenated using the bubbling method described above. Then, several concentrations of the deoxygenated hemoglobin (Hb) were prepared, and 3.5 mL of each concentration was loaded into the stopped-flow apparatus (Aminco-Morrow Stopped-Flow Apparatus, American Instrument Co., Silver Spring, MY) with a light-beam path of 4 mm. The slit was 0.8 mm, which allowed for the maximum window of detection at 10 volts for 100 % transmittance. An equivalent volume of deoxygenated water was loaded, then the two were manually mixed and the transmittance of the mixture was recorded using LabView software (National Instruments Co., Carlsbad, CA).

Second, a correcting factor that accounted for light scattering by the emulsion particles was determined. The uncoated and calcium phosphate coated emulsions were utilized for the second control experiment (scattering of light by the particles). Due to the relatively large particle size (~300 nm in diameter) when compared with hemoglobin, there were significant amounts of particle light scattering that needed to be corrected. The detector for the stopped flow apparatus was located 180° from the incident light, and it would be misleading to interpret losses in transmission due to scattering, as actual absorbance by hemoglobin molecules (Figure 3-8). The amount of light displaced by

scattering was dependent upon the particle size and refractive index. In order to properly correct for the light scattering of the particle, the relative transmittance of the samples was measured by loading them into the stopped-flow apparatus, and running the procedure as normal. In order to avoid any uncertainty, the particle size of the samples was measured by DLS to ensure similar diameters across the various concentrations. They were directly loaded in the apparatus as the first control experiment, and the transmittance was measured by the photometer.

3.3.2.2.3 Determination of Bohr Effect

One of the significant factors for loading oxygen to hemoglobin was pH because according to Bohr effect, hemoglobin should be less willing to bind oxygen at lower pH, such as pH 6.8 [188]. This was an important issue to address in order to find the proper conditions for good reproducibility. To create a proper pH range among the hemoglobin solutions, the pH was adjusted to the desired values (either 6.8, 7.2, or 7.8). Following the procedure in section 3.3.2.2.1., deoxygenated hemoglobin solutions were made, and then mixed with DI water, whose pH was matched with the hemoglobin solutions (either 6.8, 7.2, or 7.8). The stopped-flow apparatus monitored the oxygen uptake, which was conducted five times for each sample to ensure the validity of the results. The averages as well as the standard deviations were calculated, which the error bars represent. This method also was applied to the uncoated emulsion. The oxygen uptake was measured five times with the apparatus, and the results were averaged with the standard deviations, representing the error bars.

3.3.2.2.4 Oxygen Measurement of Calcium Phosphate Coated

Nanoemulsion

To test the effects of layer coating thickness, four different samples were produced, each with a different number of calcium phosphate layers; the procedure is described in section 3.3.1.3. For the emulsion itself, the concentration of soy lecithin was 1.4 mM, and the added amount of PFOB was 2 vol.%. They were then coated with different numbers of layers of calcium phosphate (CaP) and mixed in the stopped-flow apparatus with the deoxygenated hemoglobin described in Table 3-2. The pH of the samples was adjusted to 7.2 with NaOH, a condition previously determined in section 3.3.2.2.3. The amount of oxygen transferred from the CaP coated particle was monitored by spectroscopic changes in hemoglobin, and the results were verified by measuring each sample five times.

3.4 Results and Discussion

3.4.1 Calcium Phosphate Coating

3.4.1.1 Synthesis of Nanoemulsion in Oil-in-water Phase

The emulsion, synthesized by the stirring method in Figure 3-9 prior to extrusion, displayed a broad range of particle sizes, with most of them being greater than 1 um. Under cross-polarized light microscopy, the particles showed a Maltese-cross pattern that is indicative of a multilamellar formation at the emulsion surface [189]. After the emulsion had been extruded, the particle size became much smaller, almost invisible under bright-field microscopy, and the Maltese-cross shape previously seen had disappeared. The absence of the Maltese-cross was strong evidence that the phospholipid layer was no longer multilamellar, but rather a monolayer, separating the oil and water

phases (Figure 3-10 and Figure 3-11). The emulsion, isotopic liquid mixtures of oil, water, and surfactant, did not interfere with the polarized light and appeared dark [190]. After extrusion, the PFOB content was slightly reduced by 3.9 % (Figure 3-12); for example, if the initial volume of PFOB were 2.00 mL in 100.00 mL, the final volume would be 1.92 mL. This appears to be an inherent consequence of using the extrusion method, where a small amount of PFOB is simply retained within the unit.

During the emulsion synthesis, it became obvious that more soy lecithin in the emulsion reduced the amount of leftover PFOB. Above 1.1 mg/g of soy lecithin (or an overall concentration of 1.4 mM) did not exhibit any leftover PFOB (Figure 3-13 (A) and (B)). Moreover, the particle size increased with increasing soy lecithin, whereas a constant diameter was seen at lower amounts (Figure 3-13 (C) and (D)). The nanoemulsion-optimized condition was defined as having no PFOB leftover, and a particle size closest to the pore size of the membrane, 200 nm. This also limits the creation of liposomes and free surfactant structures. This specified condition has the following composition: soy lecithin (1.1×10^{-3} wt/wt), PFOB (3.9×10^{-2} wt/wt), and water (9.6×10^{-1} wt/wt).

3.4.1.2 Ionic Interaction of Emulsion

3.4.1.2.1 Optimization of Soy Lecithin Emulsion in pH

The pH titration test supported the notion that the phosphate group in soy lecithin was the site of ion interaction. Since the amine group in soy lecithin is quaternary, three methyl groups and one R group, it is not pH active. The phosphate in the head group of soy lecithin was the only chemical group that was expected to react with a proton.

The zeta (ζ) potential is a good indicator of the dispersion stability. Near zero mV in ζ-potential results in minimal electrostatic repulsion between particles, so the greater absolute value of zeta (ζ) potential, the better the stability due to the charge repulsion [140]. From the change in ζ-potential with pH, the isoelectric point (pI) and the electrostatically stabilized condition were determined (Figure 3-14). The emulsion yielded a ζ-potential of -38.5 mV, at pH 10.6, and upon the addition of acid, the zeta potential continued to increase until it reached 0 mV, at a pH of 4.1, the isoelectric point (pI). Continuing further, the ζ-potential raised to +5.8 mV at pH 2.8. The pI was measured to be at pH 4.1, which was in agreement with the previously reported value [191]. Soy lecithin molecules are zwitterionic because of the positive quaternary amine and the negative phosphate groups (pH dependent), making them ampholytic which means the molecule can obtain equilibrium in either basic or acidic conditions.

The soy lecithin emulsion surface was saturated with the negatively charged OH⁻ ions at pHs greater than 8.85, which is due to the electrostatic interaction between the positively charged quaternary amine and the free ion. The addition of more protons drives the equilibrium reaction, Le Chatelier Principle, toward the production of more water as a result there is an increase in ζ-potential, described in Eq. 3-4.

$$H_3O^+ + OH^- \rightarrow 2H_2O \qquad \qquad \text{Eq. 3-4}$$

Once the pH reached the isoelectric point, the overall electric charge in the head group of soy lecithin became neutral. When the ζ-potential started to plateau at pH 3, this suggested that essentially all of the phosphate groups had reacted with the protons, resulting in a net positive charge.

The head group of the soy lecithin molecule is bent, resting at about 90° [192],

and since the emulsion is formed by a complex array of soy lecithin, it was challenging to identify if either the amine or phosphate group was the primary binding site. From the pH titration and ζ-potential, it was concluded that the phosphate group was the primary binding site for free ions, see Figure 3-15. The amine group electrostatically bound to hydroxide at high pH and released it at decreasing pH. At pH 9, all soy lecithin molecules were deprotonated, and as a result, the phosphate groups were negatively charged, creating a negatively charged surface. The zeta potential demonstrated an equivalence point at pH 5.33. The phosphate group carried one negative charge and was the conjugate base of R_1R_2HPO4, where R_1 bound to the amine group and R_2 was the hydrophobic portion of the molecule. The result of the zeta potential measurement showed soy lecithin emulsion accepting protons at pH 8.8 because the increased potential indicated the surface charge of the emulsion changed by binding the protons to the phosphate group of the soy lecithin molecule.

3.4.1.2.2 Affinity of Calcium and Phosphate to Emulsion Surface

The emulsion system was adjusted to pH 9 because this yielded the lowest ζ-potential. When calcium ion was added, the ζ-potential of the particle increased from -34 mV to -3 mV, and when hydrogen phosphate (HPO_4^{2-}) was added, it decreased from -34 mV to -39 mV (Figure 3-16). The soy lecithin molecule, which was mostly deprotonated at pH 9, needs to be at a high pH for cation attraction. As a result, the change in potential with calcium absorption was greater than that caused by phosphate, which was a slight reduction.

At pH 9, the phosphate group is the dominant functional group for soy lecithin because the quaternary amine has been neutralized by the OH⁻ anion (Figure 3-17). When

calcium ion was added to the emulsion system, the ion associates itself with the phosphate group due to the lower solubility product constant. The solubility product constant (K_{sp}) values at 25 °C of calcium hydroxide ($Ca(OH)_2$) and calcium hydrogen phosphate ($CaHPO_4$) are 5.5 x 10^{-6} and 1 x 10^{-7} [193]; the lower the solubility, the easier it is precipitates. $CaHPO_4$ has a lower K_{sp} value than $Ca(OH)_2$; thus, it is easier for the calcium to bind to the phosphate group than the free hydroxide in solution or those adsorbed to the quaternary amine.

3.4.1.2.3 Calcium Ion Cooperativeness and Binding to Emulsion Surface

Since calcium ion has two valences, it was important to understand if the added calcium was binding to one, or two, phosphates in the monolayer. By monitoring the free calcium ion concentration with different amounts of calcium added, a Hill plot was constructed, which shows the fraction of the soy lecithin molecules saturated with calcium as a function of calcium concentration. The Hill plot and the estimated trend line from Figure 3-18 were constructed using the following equations:

$$\log\theta = n \cdot \log([Ca^{2+}]_{free}) + \log K_D \qquad \text{Eq. 3-5}$$

$$\log\theta = 0.981 \cdot \log([Ca^{2+}]_{free}) + 3.171 \qquad \text{Eq. 3-6}$$

where θ is the fraction of the occupied sites divided by total sites, n is the Hill coefficient, $[Ca^{2+}]_{free}$ is the concentration of measured free calcium in molar, and K_D is the dissociation constant. By the estimated trend line, the values of n and K_D were 0.981 and 3.171.

For infinite cooperatives, Hill coefficient, which is the slope of Hill plot, equals the number of binding sites. In fact, empirically, the coefficient is slightly less than or equal to the number of binding sites. In a real experiment, even though hemoglobin has four binding sites, the Hill coefficient of hemoglobin to oxygen, for example, is less than 4 due to the limitation of detection [130-132]. The estimated Hill coefficient (n) was 0.981, which suggests that there was one calcium ion binding to each phosphate group within the soy lecithin monolayer. This value was not exactly the same as the number of binding sites per soy lecithin molecule. It is possible that the technical precision might have caused some of the soy lecithin molecules to overlap each other so that the added calcium ion could not reach the molecule.

The logarithm of the affinity constant (K_a) is equal to the negative logarithm of the dissociation constant (K_D), shown as follows:

$$logK_a = -logK_D$$

Eq. 3-7

The estimated log K_D was 3.171, which results in a K_a of about 0.675 mM. K_a is the concentration occupying half of the binding sites, so the total concentration of binding sites was double, or 1.350 mM, which is in good agreement with the concentration of soy lecithin initially added, 1.4 mM. If both values are taken as absolutes, 96.4 % of the added soy lecithin had an associated calcium cation.

3.4.1.3 Synthesis of Calcium Phosphate Coating

Even though soy lecithin has two opposite charges on the head group, the soy lecithin emulsion is still able to bind calcium cations. In order to build the calcium phosphate coating, calcium ions were first added to the emulsion suspension, followed by

the phosphate anion. This allowed the layer to be built up layer-by-layer, with alternating additions of calcium and phosphate (Figure 3-19). The effect of each layer was measured with zeta potential (Figure 3-20 (A)), and it confirmed the sequential layering of each species as described. The initial zeta potential of the emulsion was -34 mV, and once calcium ion was added to the emulsion system, it increased to -5 mV. With the following dose of phosphate, the ζ-potential decreased to -30 mV. This same trend continued for each additional layer of calcium and each layer of phosphate, confirming the sequential growth process.

In order to verify the calcium phosphate (CaP) coating on the emulsion surface, the particle size was monitored by DLS. With each layer deposited on the emulsion surface the size of the particle linearly increased from 285 to 1400 nm. The CaP coating thickness was also measured to increase from 0 to 525 nm (Eq. 3-8).

The expected calcium and phosphate ionic bindings are shown in Figure 3-20 (B). Their binding can be modeled as bricks layers. The various thicknesses of calcium phosphate (CaP) was coated on the nanoemulsion surface (Figure 3-20 (C) and (D)). The thickness (CaP_t) was calculated as follows:

$$CaP_t = \frac{Size_{CaP} - Size_{Emulsion}}{2}$$

Eq. 3-8

where $Size_{CaP}$ and $Size_{Emulsion}$ are the measured particle size from DLS after and before CaP coating; because DLS was measuring the particle size in diameter, the subtracted size was divided by 2.

3.4.1.4 Morphology Analysis of Coated Emulsion by Transmission

Electron Microscopy

This section discusses the TEM analysis of coated and uncoated emulsions. The uncoated emulsion was prepared with a negative stain (Figure 3-21 (A)), and it revealed a uniform particle of 227.1 nm (+/- 128.7 nm). The CaP coated emulsion (27 mM of the added calcium) was measured at 250.4 nm (+/- 50.2 nm). The micrographs show a dark core with a light shell, a result of the electrons scattering off axis by elastic nuclear interaction known as Rutherford scattering. A thicker coating increased the elastic scattering due to the fixed mean-free path. This is also observed with elements of a higher atomic number that scatter more electrons than the lighter elements, making them appear darker. The molecular weight of PFOB ($C_8F_{17}Br$, 498.87 g/mol [194]) is greater than calcium phosphate ($Ca_3(PO_4)_2$, 310.18 g/mol [195]) and brushite ($CaHPO_4 \bullet 2H_2O$, 172.09 g/mol [196]). Therefore, the darker core image (Figure 3-21 (B)) suggested the presence of PFOB, and the lighter contrast surrounding the particle was defined as the calcium phosphate shell.

When the calcium phosphate coating was further propagated with the added calcium (220 mM), calcium phosphate crystalline began to form on the emulsion (see Figure 3-21 (C), and at 600 mM, aggregation of the particles became apparent (see Figure 3-21 (D). Greater addition of CaP layers resulted in a greater particle size in TEM than DLS. This is a result of the aggregation that is likely to occur while the samples dry on the TEM grid.

3.4.2 Performance of Calcium Phosphate Coated Nanoemulsion

3.4.2.1 Stability in Practical Conditions

The stability of the particle needed to be studied under practical application and storage conditions, such as long-term storage at room temperature, transportation conditions, and sterilization procedures. Both the calcium phosphate coated and uncoated emulsion samples were tested under all of these conditions, determining their stability with respect to time, mechanical perturbation, and thermal effects (Figure 3-22). The first condition tested was in the dark at room temperature for a period of 50 days. After 20 days, the uncoated emulsion showed an increase in particle size, up to 450 nm in diameter, in addition to an increase in standard deviation. Meanwhile, the coated emulsion remained at a constant particle diameter for the full 50 days. Shaking the samples on a platform shaker for 150 minutes tested the physical stability of the samples. The coated sample showed much greater stability with no observable change in the particle size, but for the uncoated emulsion, flocculation became evident as the particle size constantly changed. The thermal stability of the particles was tested using an autoclave with the standard sterilization temperature of 121 °C. After autoclaving, there was no change observed in the coated emulsion's particle size, but the uncoated emulsion became very heterogeneous after the treatment, with additional peaks in the particle size distribution spectra (1500 nm, 280 nm, and 100 nm). Even though the coated emulsion showed a size increase from 325 nm to 360 nm, it remained monodisperse, and the diameter increase was insignificant compared to the changes seen in the uncoated system.

3.4.2.2 Oxygen Release as an Oxygen Carrier

3.4.2.2.1 Limitation of Photometer and Correction Factor

In order to find the limitations of the photometer, various concentrations of deoxygenated hemoglobin (Hb) were mixed with the deoxygenated buffer solution. The result showed that the relative absorbance started to plateau at an overall concentration of 120 uM (Figure 3-23 (A); therefore, the Hb needed to be less than 200 uM because the stopped-flow apparatus would be inaccurate in detecting small changes at this concentration level.

Due to the relatively large size of the uncoated and coated nanoemulsions (~300 nm), the particles can cause significant light scattering, which generates error during absorbance measurements. In the stopped-flow apparatus, the photometer detector is located $180°$ from the incident light, and as a result, the scattered light is displayed as absorbed light, which can dramatically alter the interpreted results. Light scattering characteristics of the emulsion suspension showed that the maximum concentration was 6 vol.% PFOB. Above this concentration, the amount of light scattered is too large, which makes it very difficult to analyze the spectra. This same concentration limit was replicated for the calcium phosphate coated particle. When the uncoated and coated emulsion systems were tested at 2 vol.% of PFOB, which was the concentration used in all subsequent measurements, the photometer detected 0.68 and 0.62 in the relative transmittance (Figure 3-23 (B)), respectively. These values were used as the new baseline for measuring and estimating the oxygen uptake by hemoglobin.

3.4.2.2.2 Determination of the Bohr Effect

The collected, cell-free hemoglobin at various pHs was deoxygenated by nitrogen purging. The results suggest that oxygen uptake and the kinetic constant of the deoxygenated hemoglobin (Hb) both increase with increasing pH (Figure 3-24 (A)). The oxygen uptake was 174 uM at pH 6.8, 194 uM at pH 7.2, and 229 uM at pH 7.8 (Figure 3-24 (B)), see Appendix B. When an equilibrium is established between air and the amount of oxygen dissolved in water, the oxygen content is estimated to be about 20.95% [197], which was further evaluated using Henry's law constant (1.3 mM atm^{-1} [198]). The oxygen uptake at pH 7.8 was similar to the estimation (234 uM), making sure to account for the altitude of Salt Lake City (4,300 ft.). By comparing with the result, the actual measurement was 2.1% lower than the estimation.

When the same method was applied to the uncoated emulsion, raising the pH showed an increase in the amount of oxygen increase. The oxygen uptake was 264 uM at pH 6.8, 270 uM at pH 7.2 and 284 uM at pH 7.8. However, the quality of the data got worse with introduction of more noise. The standard deviation (error bars) was significantly greater from +/-1.5 at pH 6.8 and 7.2 and +/-3.2 at pH 7.8 when the pH was increased to 7.8, and was also demonstrated in the absence of the emulsion particle (Figure 3-24 (C) and (D)). The difference between the oxygen uptake at pH 6.8 and that at pH 7.8 was smaller than the water and hemoglobin control (Figure 3-24 (B)). It is possible that the Hb was mixed with a solution containing a greater concentration of oxygen, so the larger concentration gradient caused the Hb to take up more oxygen. In short, this control experiment confirmed that the fast mixing method is suitable for measuring the oxygen content of the emulsion particles. Also, a higher pH was shown to improve oxygen capacity at the expense of data integrity, and at the lower pH 6.8, the Hb

did not sufficiently uptake oxygen from the emulsion particles. Therefore, in order to have the greatest amount of oxygen content with the highest quality data, this control experiment was conducted at pH 7.2.

According to the Bohr effect, the oxygen affinity of hemoglobin drops with decreasing pH (Figure 3-24 (A)). In other words, the tendency to release oxygen increases in acidic conditions. This observation was in good agreement with the Bohr effect. The deoxygenated hemoglobin (Hb) had a greater oxygen uptake at higher pH values. As pH decreases, protons increasingly bind to hemoglobin amino acids; this decreases the hemoglobin affinity for oxygen by reducing the number of binding sites (Figure 3-24 (B)). When the emulsion was added to the solutions at various pHs, the results were the same, agreeing the Bohr effect (Figure 3-24 (C) and (D)). As concluded earlier, the control experiment suggested an optimal pH of 7.2. These control experiments concluded that the fast mixing method is suitable for studying the transfer of oxygen between hemoglobin and emulsion particle.

3.4.2.2.3 Oxygen Release and First Association Constant $\left(k_{a_1}\right)$

The relationship between the thickness of the coating and amount of oxygen released was determined in this section of the project. Increasing the coating thickness caused the amount of oxygen released to drop from 77 uM to 45 uM, and the kinetics constant (K_1) decreased from 2.8 s^{-1} to 0.6 s^{-1} (Figure 3-25), see Appendix B.

The mass transport pathway starts with the soy lecithin monolayer, after which, the oxygen must travel through the calcium phosphate shell, the second layer. The total length of the soy lecithin molecule, including head group and tail, is 5.03 nm [199], and

the thickness of the calcium phosphate coating varied between 8 to 38 nm. It was expected that the diffusion time for the coated emulsion would be significantly longer than that of the uncoated particle due to the extra barrier. The oscilloscope reading shown in Figure 3-25 (A) demonstrated a smoother curve, compared to that of the control experiment with the solvent and hemoglobin in Figure 3-24 (A). This is thought to be a consequence of the gradual release of oxygen gas, which led to a prolonged exchange between particle and deoxy-hemoglobin due to a limited number of collusions [200-202]. The overall reaction rate became more dependent on the diffusion of particles rather than transport of oxygen across the barriers. To summarize, a slower release of oxygen generated a smoother, more gradual, change in the transportation of oxygen.

Even though hemoglobin has four positions to which oxygen can associate itself, this study was only concerned with the kinetics of the first oxygen to bind to the deoxy-hemoglobin (Hb) because the other three are nonlinearly related to each other with respect to time. Therefore, a pseudo first-order reaction was assumed, Eq. 3-9, and it was used to calculate the first order kinetics rate coefficient $\left(k_{a_1}\right)$.

$$\frac{d[HbO_2]}{dt} = -k_{a_1}[HbO_2] \qquad \text{Eq. 3-9}$$

$$\log Y = -2.3 k_{a_1} t \qquad \text{Eq. 3-10}$$

where [HbO_2] was the concentration of the oxygenated Hb, t was the time for the first binding reaction, and Y was the fraction of hemoglobin absorbance at 550 nm. By plotting the logarithm of Y as a function of time, k_{a_1} was obtained from the slope. According to this relation, k_{a_1} showed a lower value with a thicker coating, which

confirmed the idea that the coating thickness controlled the release oxygen. The amount of oxygen inside the coated particle was less than the uncoated emulsion; hence, the oxygen uptake by Hb was lower than the uncoated emulsion. In order to verify the final oxygen content in the samples the reaction was continuously monitored until the transmittance level plateaued. In Figure 3-26 (A) and (B) the thicker calcium phosphate coating resulted in a longer diffusion time of oxygen across the interface.

3.4.2.2.4 Estimated Diffusion Coefficient of Released Oxygen

The release of drugs *in vivo* can vary greatly due to a vast number of variables, thus, *in vitro* modeling is used to estimate the performance of the particle as it would *in vivo*. The Hixson-Crowell model is the simplest model used to approximate oxygen release through the membrane and coating. This is because oxygen located closer to the surface of the particles would diffuse out first, an assumption that is very compatible with the Hixson-Crowell. The "drug" in the Hixson-Crowell model is represented by oxygen in this experiment, and its diffusion coefficient was calculated. Two samples were tested: a monolayer membrane, which only had a surfactant layer, and a calcium phosphate coated particle. Even though the Hixson-Crowell model is based on the dissolution of a solid particle, the relative change of the diffusion coefficient between the uncoated and coated particles proved that the coating does reduce the release rate of oxygen. As described in Table 3-3, the diffusion coefficient of oxygen through the coated particle dropped by 5%, relative to the uncoated particle, and remained constant independent of the shell thickness.

By treating the oxygen inside the emulsion as a drug, the Hixson-Crowell cube root law was applicable to the emulsion system. It was able to estimate the amount of

drug released by taking into account changes in the particle's surface area and diameter. The diameter of drug (or oxygen in this case) remained the same regardless of particle characteristics, and the overall oxygen release time was dependent on the thickness of layer (Figure 3-27). For the calcium phosphate coated particle, it should be noted that the derived diffusion coefficient does not differentiate between the membrane and mineral layers, only one inclusive layer is considered.

In order for this system to be useful, the water layer surrounding the particle must be sufficiently thick when compared to the particle diameter; in other words, the particle should be smaller than 500 um in diameter to apply the Hixson-Crowell law [203]. By applying the Noyes-Whitney equation to the Hixson-Crowell law, the change of particle size in radius as a function of time can be estimated as follows:

$$r^2 = r_o^2 - \frac{2DC_st}{\rho}$$ Eq. 3-11

where r_o is the initial radius, D is the diffusion coefficient, C_s is the drug concentration, t is drug release time in seconds, and ρ is the density of a particle. The time consumed for complete release of the drug is when the radius (r) equals to zero. Then, Eq. 1-2 is re-written as follows:

$$t = \frac{\rho r_o^2}{2DC_s}$$ Eq. 3-12

Even though the measured oxygen was 76 uM, excluding the dissolved oxygen in the continuous phase of the emulsion system, the measured oxygen uptake indicated that the number of particles determined the overall oxygen concentration in the system. However, the individual particle contained pure PFOB, which has an oxygen content of

4.5 mM at 4,300 ft. when in equilibrium with air. A more detailed calculation is described in Appendix C.

Using this concept, the diffusion coefficient could be estimated by Eq. 3-2, assuming all oxygen was released from the particle. For example, the radius (r) of the uncoated emulsion particle was 137 nm (only considering the PFOB liquid), C_s was 4.5 mM, and the density was 1.93 g/mL. The estimated diffusion coefficient of the uncoated emulsion was 3.28×10^{-5} cm^2 s^{-1}, which is lower than in PFOB (3.5×10^{-5} cm^2 s^{-1}), but greater than in water (2.5×10^{-5} cm^2 s^{-1}) and plasma (2.2×10^{-5} cm^2 s^{-1}) [181]. Furthermore, the estimated diffusion coefficient was greater than the diffusion coefficient of oxygen uptake by the red blood cell (2.1×10^{-7} cm^2 s^{-1}) [204].

This result is due to the following: 1) the nanoemulsion had a smaller size (280 nm) than the cell (8-10 um); the larger particle decreases the overall interfacial surface area, which provides the less open gate flow of oxygen from the particle [181]; 2) the emulsion had a monolayer of lipid while the cell had a bilayer, therefore, the emulsion had a shorter barrier for gas transfer; 3) the concentration difference between inside and outside the emulsion in this experiment system was high because the environment outside of the emulsion was deoxygenated; and 4) the oxygen concentration inside the emulsion was much higher due to the solubility of oxygen in PFOB. Even changing emulsion size altered the diffusion rate; the greater particle size of PFOB based emulsion showed a slower release of oxygen to the surroundings [181].

The calcium phosphate coated emulsion proved that a thicker coating decreased the amount of oxygen released over a given time; the oxygen released was from 76 uM to 45 uM. Zero nanometer thickness is synonymous with the uncoated emulsion. The thickness was determined by the difference between the uncoated and the coated

emulsion. Eq. 3-11 was used to estimate the diffusion coefficient. The coated emulsion increased the particle size by the coating thickness, but the containment space for the dissolved oxygen went unchanged from the uncoated emulsion. The calcium phosphate coated emulsion system assumed that the calcium phosphate coating layer was not dissolved in the solvent during the reaction with the deoxygenated hemoglobin solvent. Therefore, the drug, defined as oxygen in this system, was released in a limited range by the coating thickness. Setting the final radius (r) in Eq. 3-10 as the coating thickness and the initial radius (r_o) as the measured particle size by DLS, the average diffusion coefficient of the coated emulsion was 3.10×10^{-5} cm^2 s^{-1} ($\pm 2.31 \times 10^{-7}$), shown in Table 3-3. Additionally, the result suggested that the thicker the coating, the longer the oxygen release from the particle.

Previously, the Roughton model for oxygen diffusion and reaction with hemoglobin was used to simulate the oxygenation of red blood cells [204]. Later, this model was improved by using a Laplace transform [205]. These theoretical approaches focused on the understanding of the diffusion coefficient via the bilayer membrane in the red blood cells. The Roughton model used oxygen outside of the red blood cell that diffused into it and interacted with hemoglobin. This model was not ideal for this study, but the fundamental concept of diffusion through the membrane was considered. The fundamental kinetics reaction (Eq. 3-13) was also accounted for in this study.

$$Hb(O_2)_n \underset{k_1}{\overset{k_{-1}}{\rightleftarrows}} Hb(O_2)_{n+1} \qquad \text{Eq. 3-13}$$
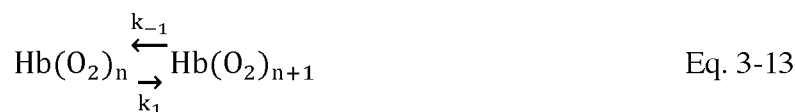
where n = 0, 1, 2, and 3 by assuming the association constant (k_1) and the dissociation constant (k_{-1}) were the same for all n's [205].

In this study, however, the Hixson-Crowell law (Eq. 3-11), see Figure 3-28, which focuses on the surface area of the particle, was used to determine the amount of oxygen released. This technique was used because of the small particle size and the increase in overall surface area and concentration with a smaller individual diameter. Even though the emulsion is not a solid particle, it can be treated as such because 1) the emulsion in this study was in the submicron region (~280 nm) and 2) the difference in oxygen concentration between the inside and outside of the particle was high so the monolayer boundary had little effect. Therefore, the Hixson-Crowell equation is more suitable than the Roughton model in this study because the Hixson-Crowell equation estimates drug release from the solubility of the solid.

The advantage of this method, combined with the deoxygenated condition, had less error by directly observing the reaction of the media in a shorter period of time. The experimental setup caused an extremely high concentration gradient, but the different diffusion coefficients show that the coating does indeed slow down oxygen release. The diffusion coefficient for the calcium phosphate coated emulsion was constant, regardless of coating thickness.

Other studies have found that the oxygen diffusion coefficient through an artificial lecithin bilayer membrane was 2.10×10^{-5} cm^{2}s^{-1} at 25 °C [206, 207]. The calculated value of the oxygen diffusion coefficient through this study's emulsion particle was 3.28×10^{-5} cm^{2}s^{-1} at 20 °C, which was greater. This comparative increase in the diffusion coefficient is thought to be a result of either the lecithin monolayer (versus a bilayer), or a larger concentration gradient between the particle and surrounding fluid. Nevertheless, this calculation proved that the Haxison-Crowell model would be suitable to estimate the diffusion coefficient. Furthermore, the oxygen diffusion coefficient

through the calcium phosphate coating was lower, at 3.10 (+/- 0.02) $\times$ 10^{-5} $cm^2 s^{-1}$, significantly less than the uncoated emulsion. This was expected, as the coated surface would add an additional barrier for the oxygen molecules to overcome.

3.4 Summary

This study described the encapsulation of the nanoemulsion with calcium phosphate and its performance regarding stability and the release of oxygen. The nanoemulsion was made with the desired phase, as determined from the ternary diagram results. Then, the emulsion surface was coated with calcium phosphate by optimizing the reaction conditions, such as pH and ion activity. The stability of the coated emulsion was analyzed in various conditions, such as elevated temperatures, physical perturbation, and time. The coated emulsion showed improved stability across all environments and treatments when compared with the uncoated one. The uncoated and the coated emulsions both showed that they do indeed release oxygen; however, the presence of the calcium phosphate coating caused a slower rate of oxygen release.

Table 3-1 The summary of stability tests for uncoated and coated nanoemulsion by calcium phosphate.

Tested stability	Tested methodologies	Duration	Temperature
Thermal stability	Autoclave	4 hours	20 °C–121 °C
Physical stability	Shaker	150 minutes	20 °C
Time stability	Storage	50 days	20 °C

Table 3-2 The summary of the experimental procedure for oxygen release from coated and uncoated emulsions.

Preparation and reaction of deoxygenated hemoglobin	Experimental steps
Collecting hemoglobin	1. Wash the red blood cells 5 times with normal saline. 2. Hemolyze the washed cells with phosphate buffer (5 mM, pH 7.4). 3. Measure the concentration of hemoglobin using UV-Vis. 4. Dilute the hemolysis solution to the desired concentration of hemoglobin.
Deoxygenating hemoglobin	1. Calibrate the Clark electrode using the bubbling method. 2. Deoxygenate the hemoglobin by nitrogen purging in the gas phase.
Monitoring reaction with hemoglobin	1. Calibrate the instrument. 2. Measure the reaction of the samples with the deoxygenated hemoglobin.

Table 3-3 The measured oxygen in the uncoated and coated emulsion particles, the estimated diffusion coefficient, and relative change of diffusion coefficient from the uncoated emulsion with various coating thicknesses. The measured oxygen refers to the results from fast mixing method (Figure 3-23 (B)) and is represented by the drug concentration (C_s) in Eq. 3-11. Using the equation and the results, the diffusion coefficient was estimated.

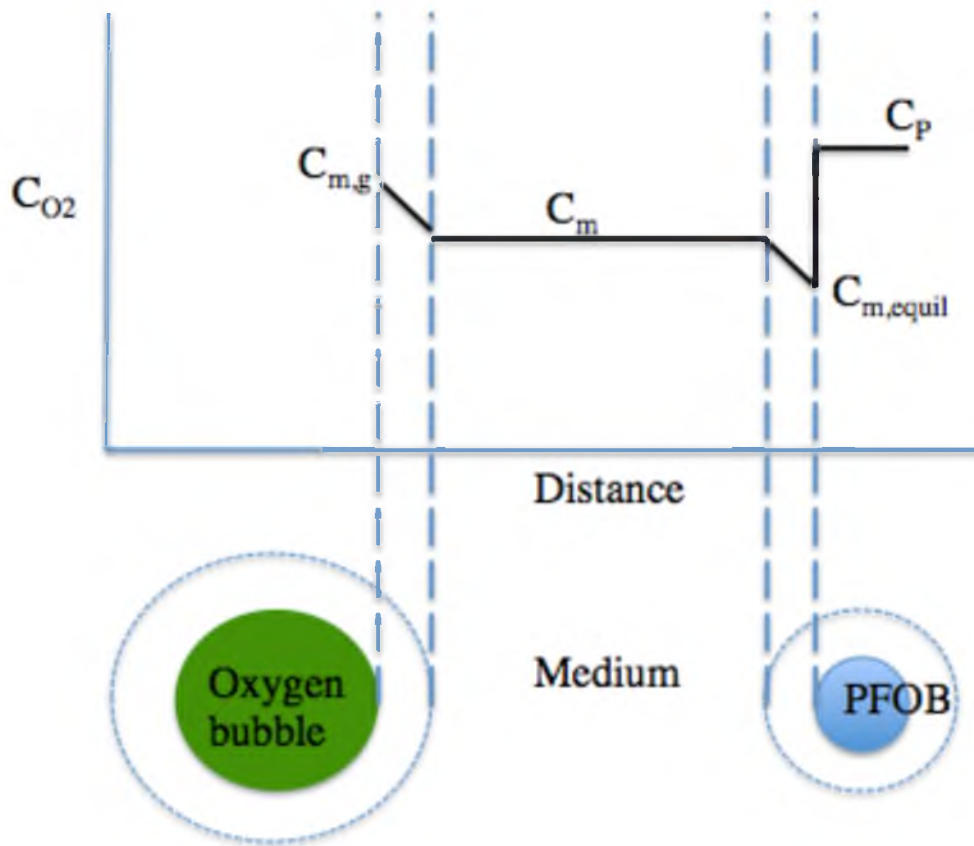| Calcium phosphate coating thickness (nm)	Measured oxygen in the system (uM)	Estimated diffusion coefficient (cm^2 s^{-1})	Relative change of diffusion coefficient from 0 nm coating thickness
0	76.0	3.28×10^{-5}	NA
8	68.4	3.12×10^{-5}	Decreased by 5.9%
24	60.8	3.08×10^{-5}	Decreased by 4.1%
38	45.6	3.10×10^{-5}	Decreased by 5.5%

Figure 3-1 A model depicting concentrations of oxygen from the gas bubble to the PFOB droplet, adapted from [181, 208]. Initially, the emulsion particle (PFOB droplet) was filled with nitrogen gas, and a known amount of oxygen was bubbled through. Measuring the amount of oxygen in solution allowed for the determination of oxygen loaded into the particle. The pathway of oxygen transfer (C_{O2}) would be gas bubble → membrane → medium → PFOB droplet. The concentration of oxygen from the gas bubble would drop as it passes through the membrane ($C_{m,g}$) into the suspending medium (C_m). Assuming there was no interruption in the medium, the concentration of oxygen (C_m) would be constant until oxygen transferred to the surface of the PFOB droplet, at which point it is reduced significantly ($C_{m, equil}$). With the assumption that the PFOB droplet absorbs all of the transferred oxygen, the concentration of oxygen would be back to the initial level (C_p).
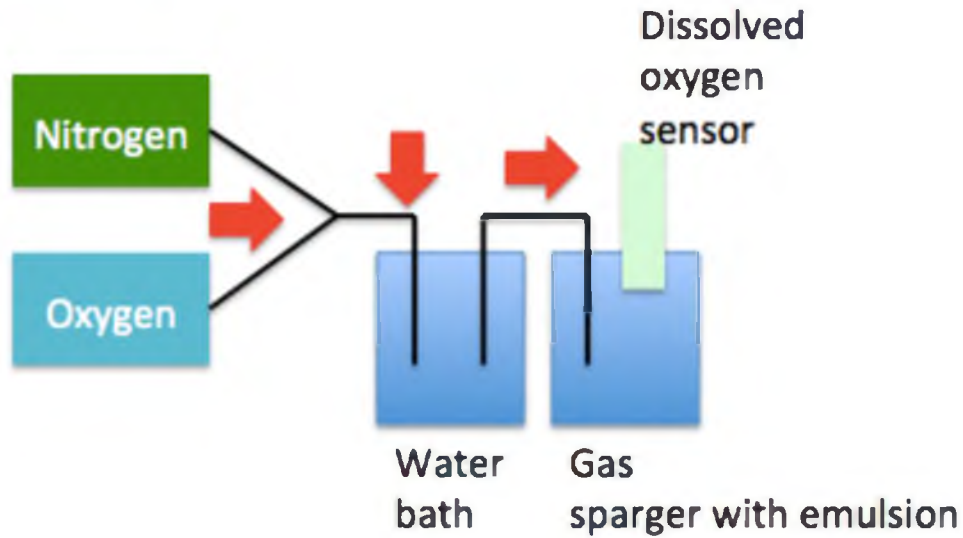
Figure 3-2 The schematics of the experimental setup for the bubbling method (or gas-sparged oxygenator), modified from [208]. The gases pressure and flow rate were monitored by P and F. The heater controlled the temperature of the experiment, and by stirring the solution in a gas-sparger, the bubbled gas was well dispersed throughout the solution. In order to measure the amount of oxygen taken by the emulsion, initially filled with nitrogen gas, the dissolved oxygen electrode probe was submerged in the solution. PFC is an acronym for perfluorocarbon.

Figure 3-3 Schematics of mechanism of oxygen kinetics measurement using hemoglobin and stopped-flow apparatus. A) A schematic showing the proposed method to measure the oxygen capacity and rate of release from the emulsion particle, which utilized the fast mix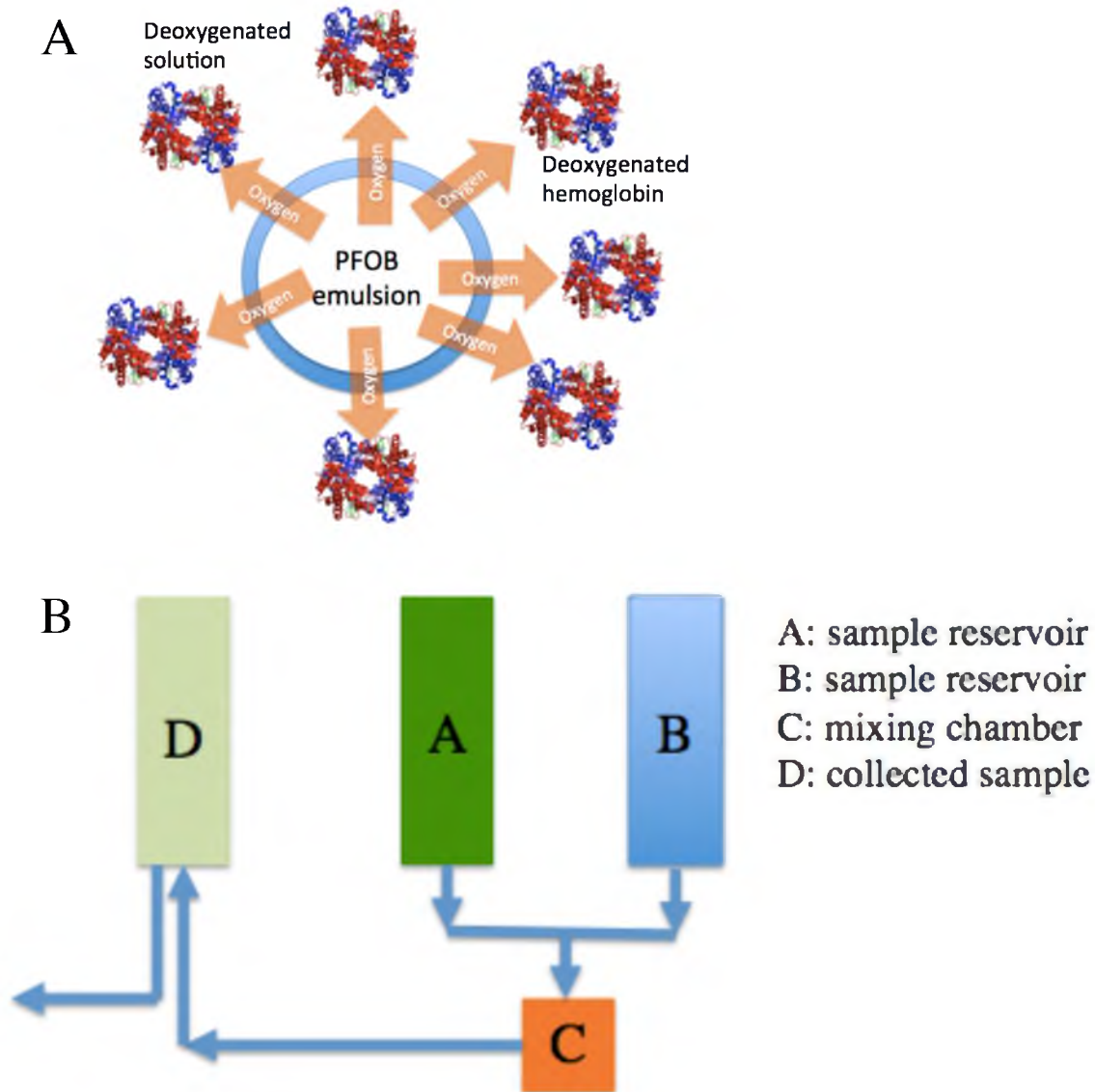ing method. Creating a very high oxygen concentration gradient allowed the deoxygenated hemoglobin to effectively react with the oxygen released by the particle. This is a measurement of kinetics, not a mass transfer method. B) The setup of the stopped-flow apparatus, modified from [209]. Two solutions (emulsion system and deoxygenated hemoglobin) were loaded into two drive pistons via the reservoir syringes. Once loaded a constant pressure was applied to the plunger, and the solutions were mixed in the mixing chamber where the reaction was observed spectroscopically. The stopping piston ensured mixing with a constant volume. After the reaction was observed in the mixing chamber cell, the waste solution was removed through the exhaust valve.
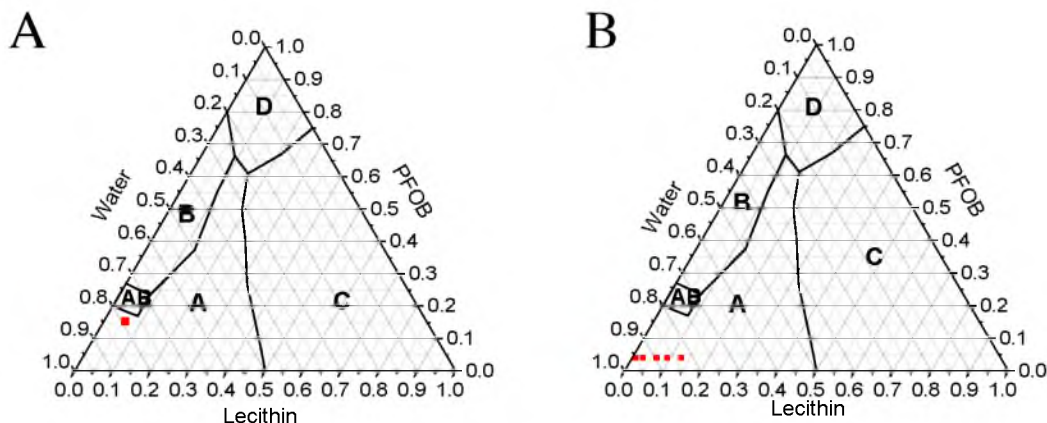
Figure 3-4 The ternary diagram of soy lecithin/PFOB/water. As described in Chapter 2, there were four phases from A to D: A) oil-in-water, B) water-in-oil, C) gel-like in oil-in-water, and D) gel-like in water-in-oil. The red dots indicate the composition for synthesizing the emulsion and compares the unextruded emulsion with the extruded one. The composition of 0.96 wt/wt of water was the minimum soy lecithin content needed to form an emulsion with no excess PFOB. The red dot in A was selected to test the hypothesis that a multilayer of surfactant could be reduced to monolayer with extrusion. There was a rich excess of surfactant with a spherical shape, 200 nm in diameter, but it was not too viscous to pass through the extrusion membrane. The red dots in B were selected by calculating the theoretical surface area of a spherical emulsion with 200 nm in diameter. It was assumed that each lecithin molecule had a surface area of 72 $\mathring{A}^2$ [210, 211] and one emulsion particle would contain 2.897×10^{-19} moles of lecithin molecules for a 200 nm diameter.
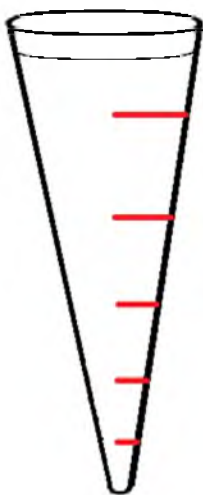

Figure 3-5 The pipette marked (red) tip. Three tips (10 uL, 200 uL, and 1000 uL) were marked in fives. Using the custom measurement method, the excess PFOB was precisely measured with a 6 % error range on 10 measurements.
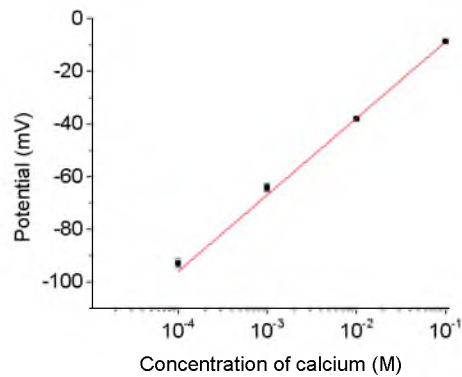
Figure 3-6 Calibration curve of electrode in series of free calcium concentration with standard deviation (+/- 0.3).
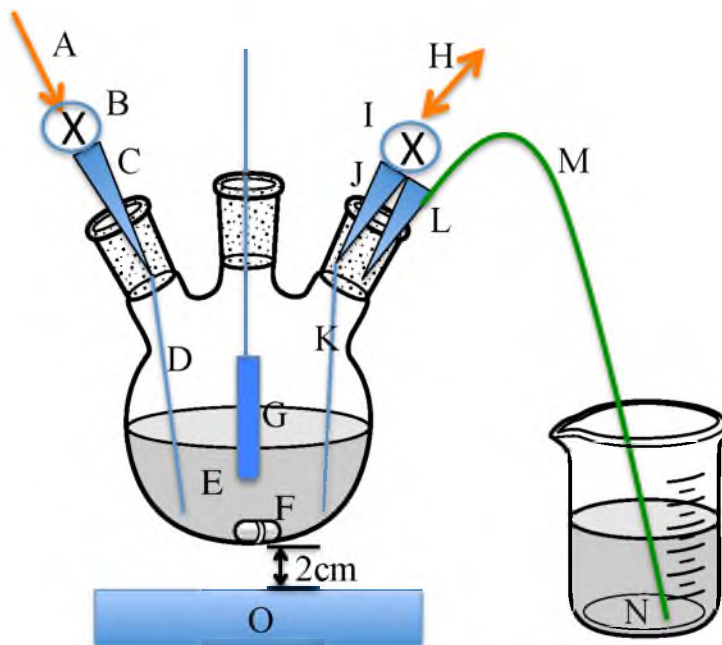
Figure 3-7 A schematic showing the deoxygenation of hemoglobin. A) Input gas direction, B) gas switch open/close, C) input gas valve, D) input gas tube, E) sample, F) stir bar (Teflon, ¾ inches), G) Clark probe, H) input/output sample direction, I) sample switch open/close, J) sample valve, K) sample tube collection, L) pressure equilibrium valve, M) pressure equilibrium tube, N) water in a beaker, and O) stir plate. The flask was suspended 2 cm above the stir plate, and thermal insulation was placed in between the plate and the flask. The samples were stirred at 100 rpm, and the probe was submerged just below the liquid surface. When the probe was calibrated with nitrogen and oxygen, the input gas tube (D) was sitting beneath the sample. When the hemoglobin was deoxygenated by the nitrogen gas, the input gas tube (D) was removed from the input gas valve (C).
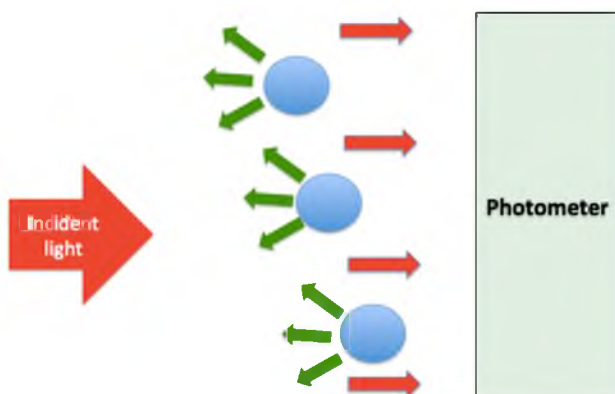
Figure 3-8 A schematic of light scattering by particles (blue). When the incident light was emitted to the particles, some (red) went to the detector, and some (green) was scattered by the particles.
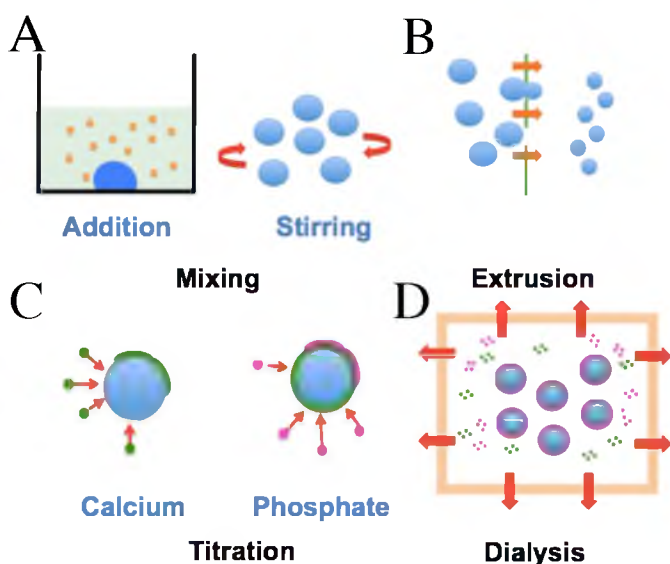
Figure 3-9 A summary of the synthesis procedure for the calcium phosphate emulsion coating. There are a total of four steps. A) Addition of the three materials (soy lecithin, PFOB, and water) to a beaker in that respective order. Water, PFOB, and soy lecithin are respectively represented by light green, blue, and orange. The mixture was stirred at 1200 rpm for 30 minutes at room temperature. B) The mixture was sized by extruding through a 200 nm pore size membrane at 150 psi, seven times. This step resulted in a uniform particle size (~280 nm in diameter). C) Titration of ions: the first step was to coat the emulsion surface. First, calcium chloride (dark green) was added to the emulsion suspension. Due to the ionic attractive force, calcium ions were adsorbed to the emulsion surface. Next, the suspension had phosphate (pink) added and associated with the calcium ions adsorbed to the emulsion surface. D) The free ions, unassociated ions, were washed away while under dialysis for 3 days.
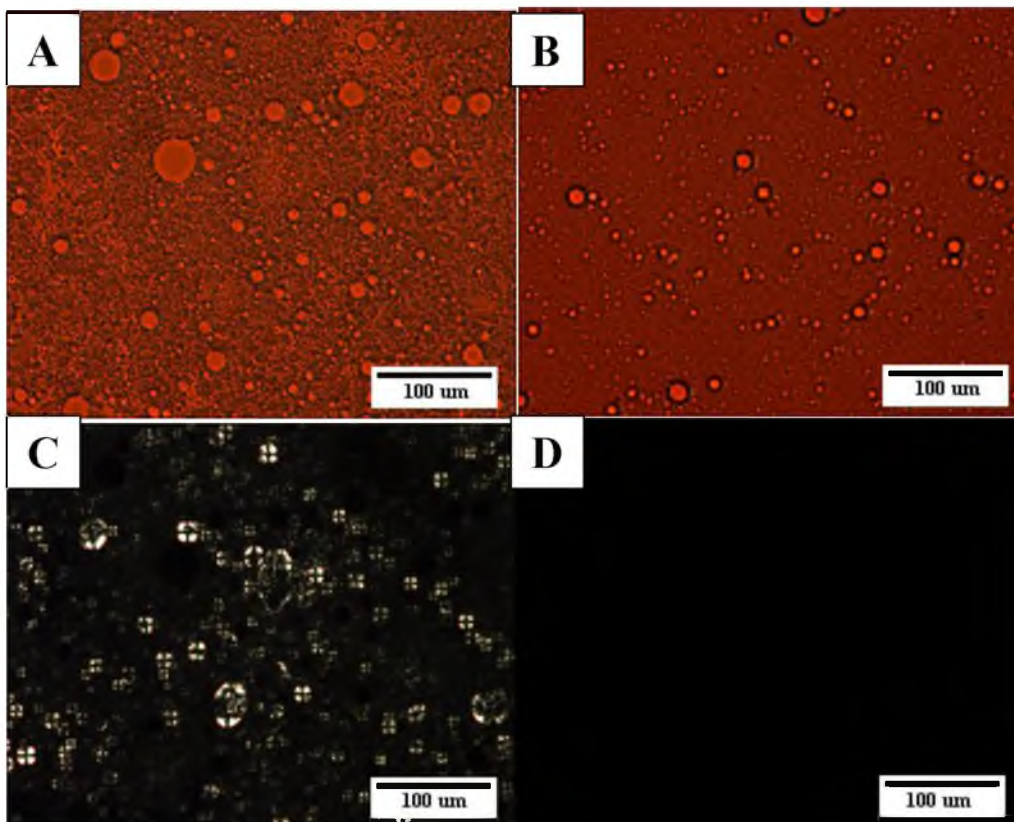
Figure 3-10 Bright field images (A and B) and cross-polarized images (C and D) by optical microscope with 200× magnification. The unextruded and extruded emulsion samples also show air bubbles in the bright-field images. The unextruded emulsion can be seen in A and C, while the extruded emulsion is shown in B and D. The unextruded emulsion has the Maltese-cross pattern under the cross-polarization and large particles under the bright-field, which is evident of a multilamellar emulsion [49]. The Maltese cross disappeared and the particle size became smaller once the emulsion was extruded through the 200 nm pore size membrane.
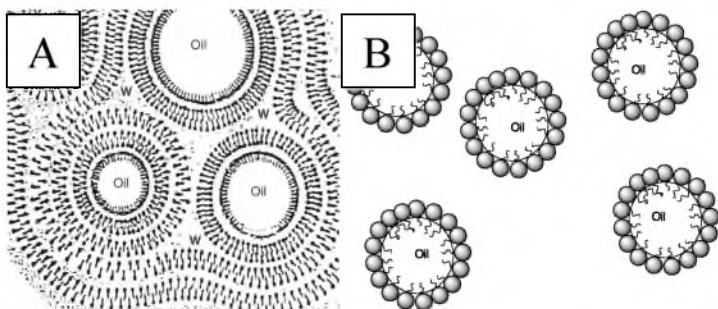
Figure 3-11 Schematics of multi and single-layer emulsions. A) Illustrations of the multilamellar emulsion droplets, reprinted from [156], which caused Maltese-cross patterns to appear under polarized light illumination. The emulsifier, which is anchored in the oil phase, is a monolayer, but excess molecules form multiple layers. The layers then intertwine to form a network of connecting particles, which influences light scattering and interacts with the polarized light. B) A schematic of the monolayer emulsion droplets. Unlike the multilamellar emulsion system, the extra emulsifiers do not connect the monolayer system, the particles remain distinct and separate. Because the emulsion has a monolayer, the light scattering from the monolayer is hardly observed by optical microscopy.
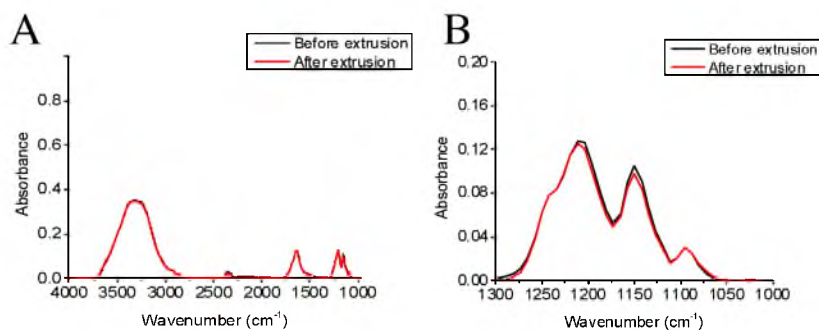
Figure 3-12 The FT-IR results of the unextruded and extruded emulsions. A) The spectrum of the samples was from 4000 cm^{-1} to 950 cm^{-1}, and B) the spectrum was focused on the PFOB region and ranged from 1300 cm^{-1} to 1000 cm^{-1}. Ultimately, there was no PFOB lost as a result of extrusion.
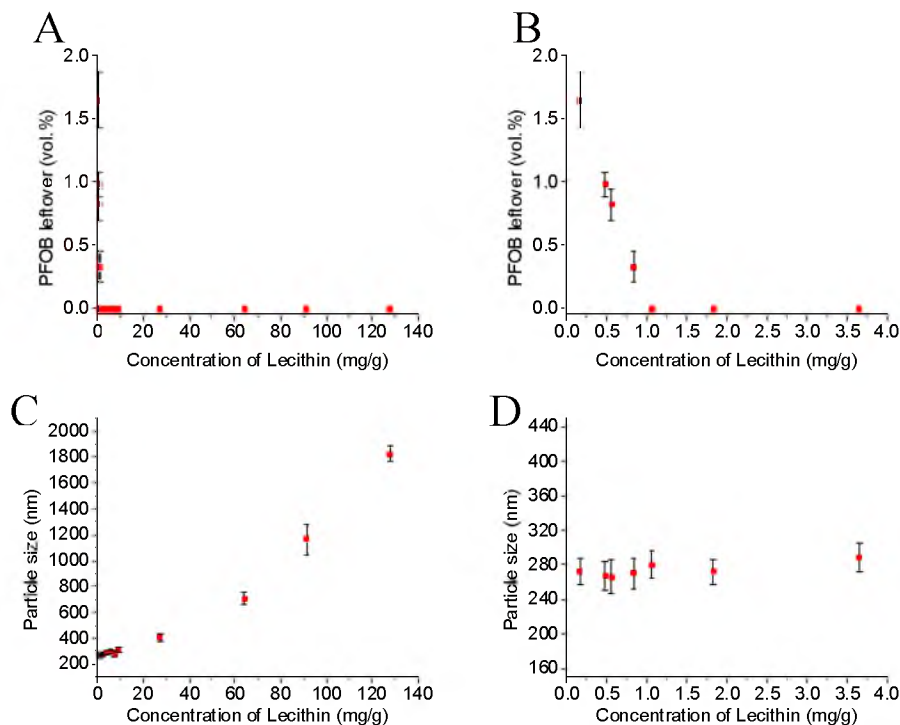
Figure 3-13 The measured PFOB leftover and the particle size after extrusion for various concentrations of soy lecithin at 9.6×10^{-1} wt/wt of water by following the direction from Figure 3-3 and with mean and standard deviation in three measurements: concentration of soy lecithin A) from 0 to 124 mg/g and B) from 0 to 3.6 mg/g. The excess PFOB was measured by following the steps described in section 3.3.1.1 after the emulsion was extruded through the membrane with mean and standard deviation calculated for all three measurements. The equal and greater concentration of soy lecithin at 1.1 mg/g showed that there were not excess PFOB. The concentration of soy lecithin C) from 0 to 124 mg/g and D) from 0 to 3.6 mg/g. The particle size was increased to 27 mg/g of soy lecithin. The lower concentration demonstrated the constant size.
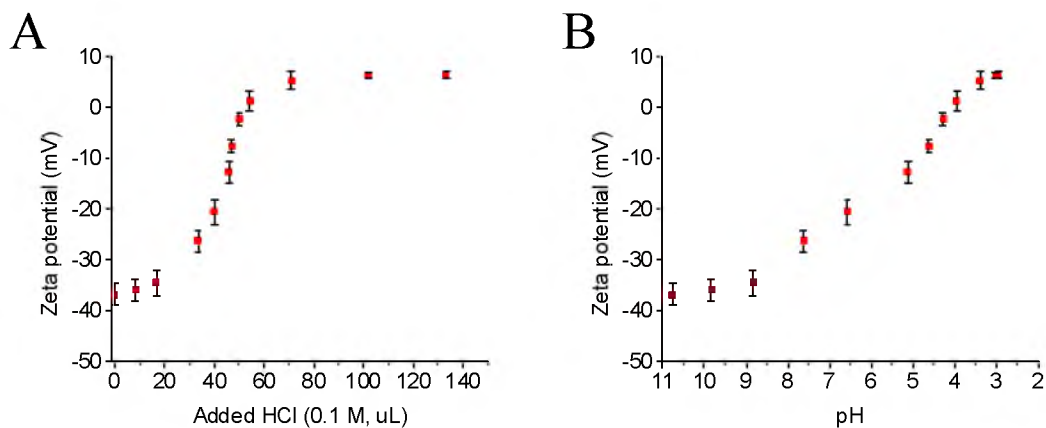
Figure 3-14 The titration curves of the emulsion. A) zeta (ζ)-potential as a function of added HCl and B) compiled zeta potential as a function of pH; the last two data points overlap because both pH and zeta potential changed slightly.
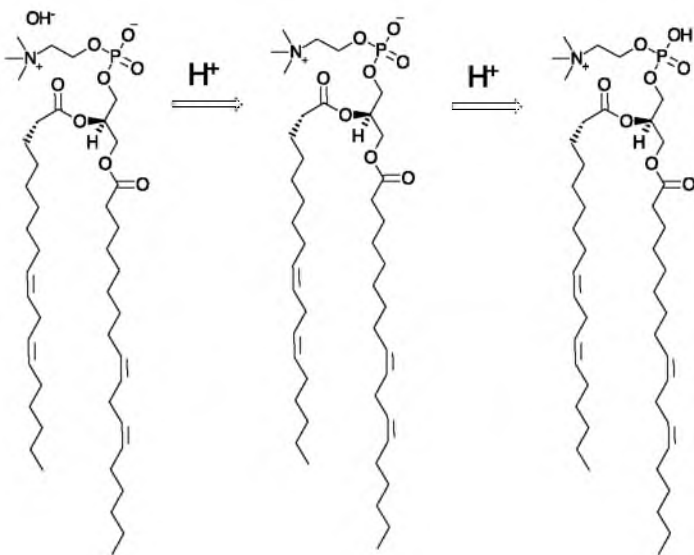
Figure 3-15 A schematic depicting how the soy lecithin molecule interacts with protons. At high pH, hydroxide approaches the positively charged amine group. By decreasing the pH, the hydroxide is binding to the added proton, creating water [212, 213]. At the isoelectric point, the molecule is neutral containing one positive and one negative charge, respectively, the amine and phosphate groups. Decreasing the pH further, the added proton is bound to the phosphate group, and the net charge of the molecule becomes positive.
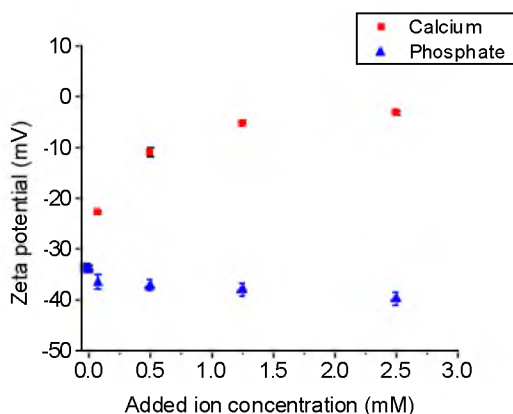
Figure 3-16 Ionic affinity of calcium and phosphate to the emulsion surface at pH 9. Zeta potential curve of the optimized nanoemulsion at pH 9 with calcium and phosphate ions to find the affinity to the emulsion surface by titration with mean and standard deviation in three measurements. The zeta potential changed from -40 mV to -21 mV by adding calcium, while phosphate changed from -40 mV to -46 mV. The absolute values of the slope in the first three data points were 18 in calcium and 6 in phosphate.

A

B

C
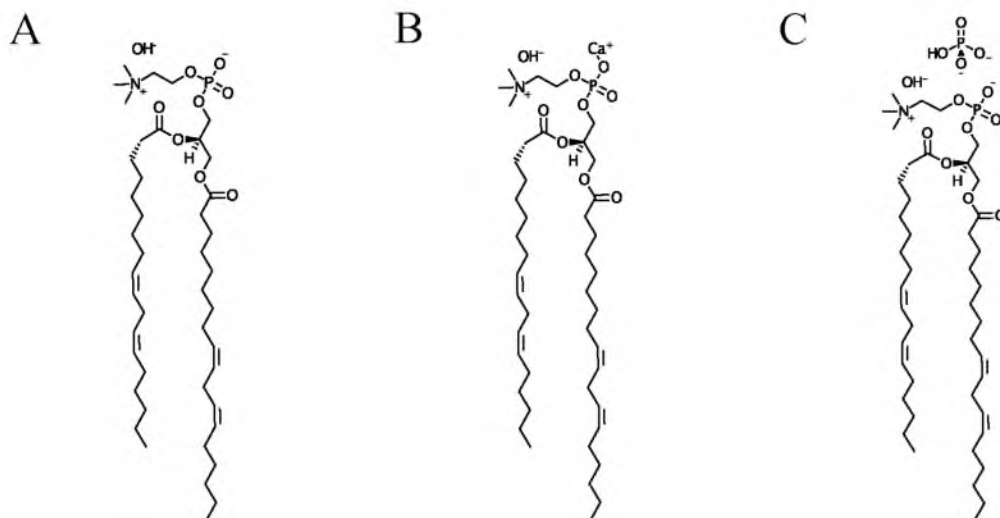
Figure 3-17 The schematics of reaction to soy lecithin molecule by the calcium and phosphate titrations at pH 9. A) The soy lecithin molecule at pH 9. The hydroxide is closely located to the amine group in soy lecithin due to electrostatic interaction, nullifying the charge of the quaternary amine. B) Titrating soy lecithin with calcium, at pH 9, the calcium ion would bind itself to the phosphate group. C) Addition of hydrogen phosphate at pH 9 does not attach to the soy lecithin head group.
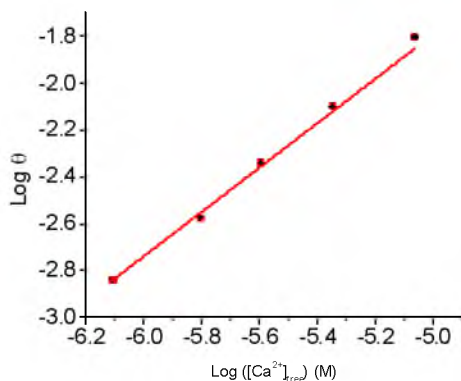
Figure 3-18 Hill plot of calcium binding to the emulsion at pH 9, with the mean and standard deviation from three measurements. Hill coefficient was 0.981. The logarithm of the dissociation constant was 3.171.
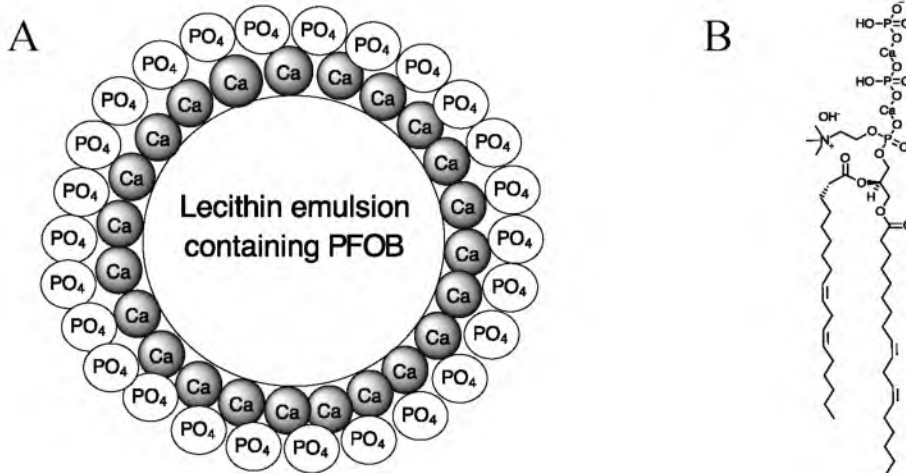
Figure 3-19 Schematics of calcium phosphate coating on the emulsion surface. A) Schematics of the calcium phosphate coating on the soy lecithin oil-in-water emulsion. Alternating the addition of calcium and phosphate, the calcium phosphate coating was built on the particle surface. B) The molecular schematic of the calcium phosphate coated soy lecithin emulsion. At pH 9.0, the amine group would attract hydroxide (OH-), and calcium would be more favorable to binding on the phosphate in the head group than the hydroxide due to the lower K_{sp}.
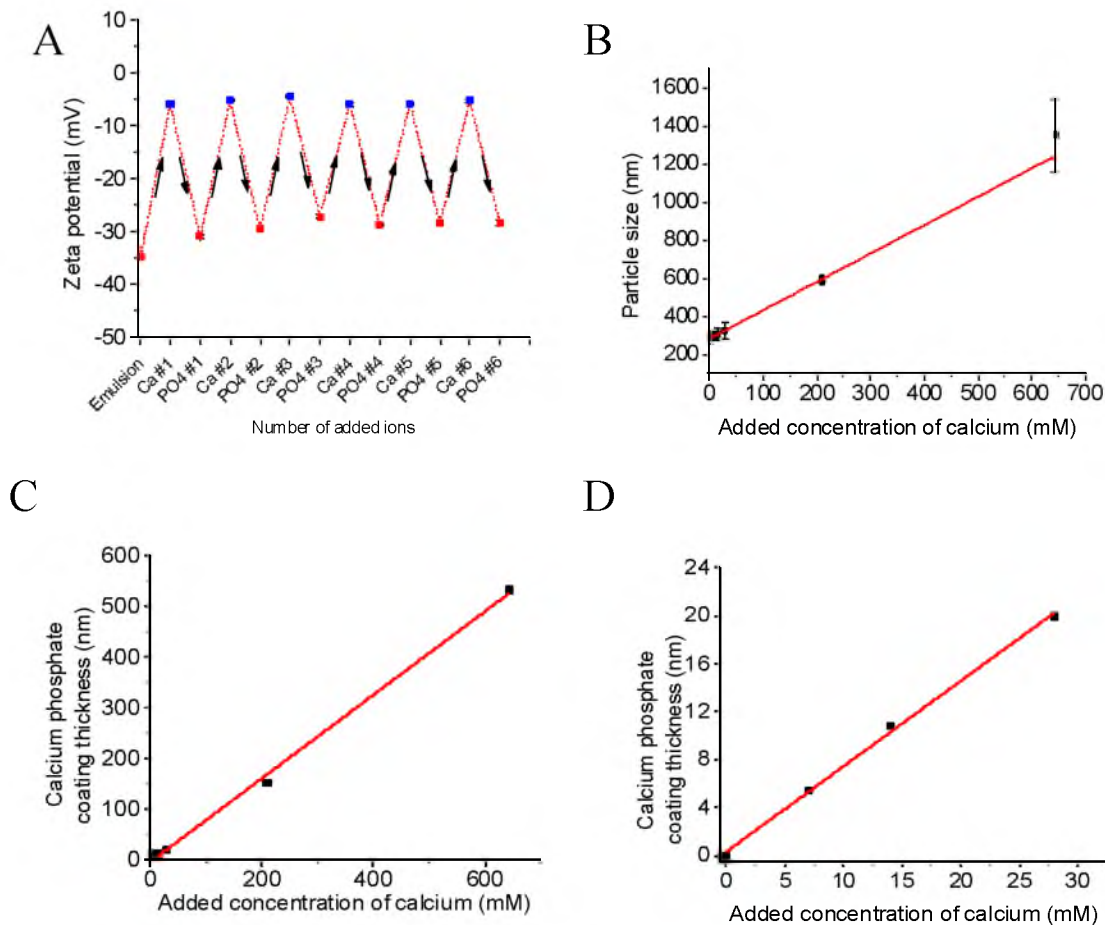
Figure 3-20 Characterizations of the coating by zeta potential and particle size. A) Changes in zeta potential with the addition of each layer of the calcium phosphate coating. The initial zeta potential was -35 mV, and the first addition of calcium (Ca) ion increased the potential to -5 mV. Then, the first addition of phosphate ($PO4_3$) decreased the potential to -30 mV. B) The particle size at various thicknesses of calcium phosphate (CaP) coating. By constantly adding the calcium phosphate, from 0 to 680 mM, the particle size increased from 280 nm to 1400 nm in diameter. The CaP coating thickness was calculated by subtracting the particle size from the initial size (281 nm), C) from 0 to 680 mM, and D) from 0 to 27 mM. The thickness was increased to 20 nm in 27 mM of the added calcium ion.
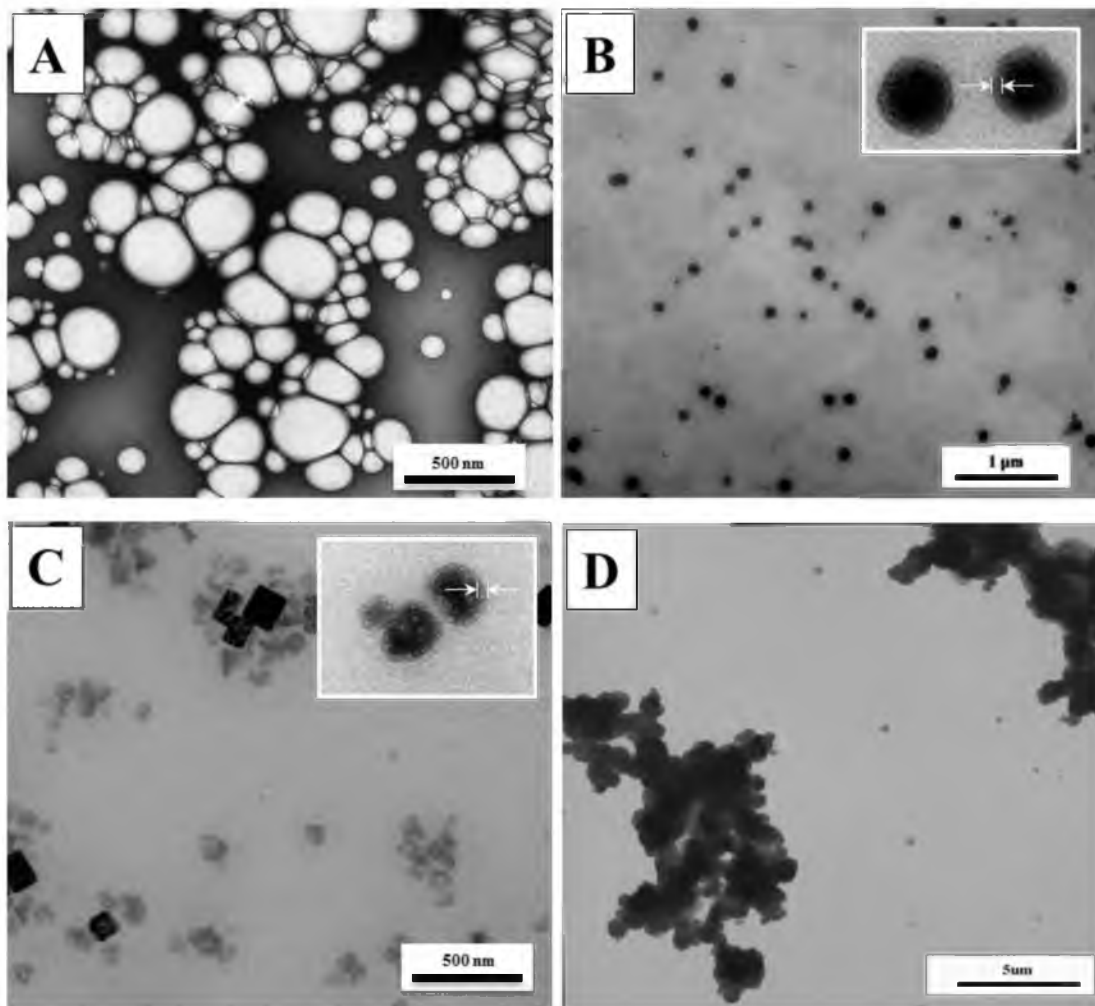
Figure 3-21 Transmission electron microscopy images of the emulsion and the calcium phosphate (CaP) coated emulsion. A) The negatively stained emulsion. The emulsion size was 227.1 nm (+/- 128.7 nm), statistics calculated from 20 particles. B) The CaP coated emulsion with 14 mM of added calcium and phosphate. The particle size was calculated based on 20 particles with an average of 250.4 nm (+/- 50.2 nm). The particle has a dark core with a lighter outline, which suggested proper formation of the calcium phosphate shell, with a measured thickness of 11 nm (+/- 3 nm). This is similar to the value calculated from DLS. C) The particles formed by adding 40 mM of calcium and phosphate solutions. Once the addition exceeded 30 mM, the calcium phosphate crystalline was also formed in the system. There were few emulsion particles, coated with CaP, with an average particle size of 320.7 nm (+/- 133.6 nm). D) The addition of calcium and phosphate was 650 mM, and all of the particles aggregated. The size of aggregations, measured by dynamic light scattering, was about 1300 nm (+/- 250 nm). It was possible that the particles became more aggregated while the sample dried on the TEM grid.
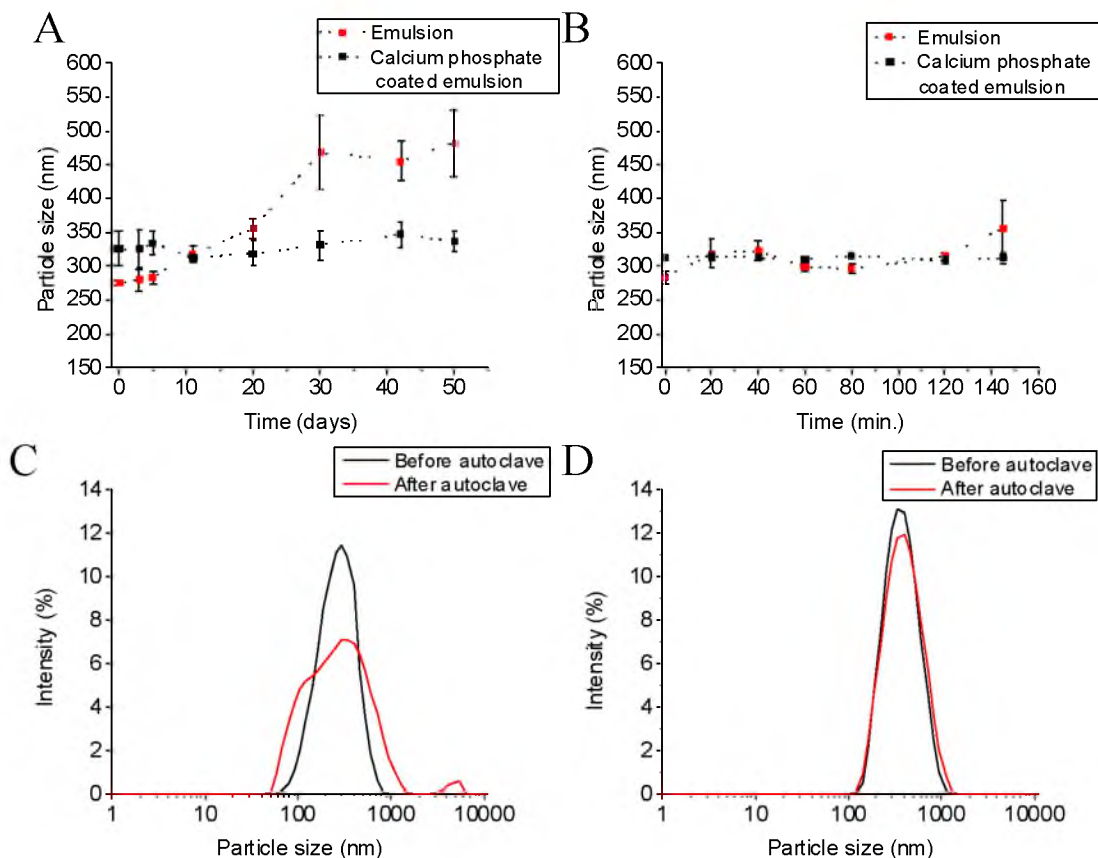
Figure 3-22 Comparing the stability of the calcium phosphate coated nanoemulsion, compared with the uncoated emulsion. The particle size was monitored, via DLS, after a set time under various conditions: A) Physical perturbation: the particles of the uncoated emulsion showed more fluctuation with increasing time in the shaker, while the coated emulsion was constant with a narrower standard deviation. B) Storage in the dark: the coated emulsion had a constant particle size over time, but the uncoated emulsion increased in size after 20 days. Autoclave: the particle size of C) the uncoated and D) the coated emulsions. The uncoated emulsion was 285.3 nm (+/- 138.2 nm in full-width half max (FWHM)) before autoclaving, and after it had a much broader size (312.3 nm +/- 296.8 nm in FWHM) with multiple peaks (110.2 nm, 312.3 nm, and 5560.0 nm). The calcium phosphate coated emulsion was 322.5 nm (+/- 172.4 nm in FWHM) before autoclaving and 340.2 nm (+/- 217.1 in FWHM) afterward.
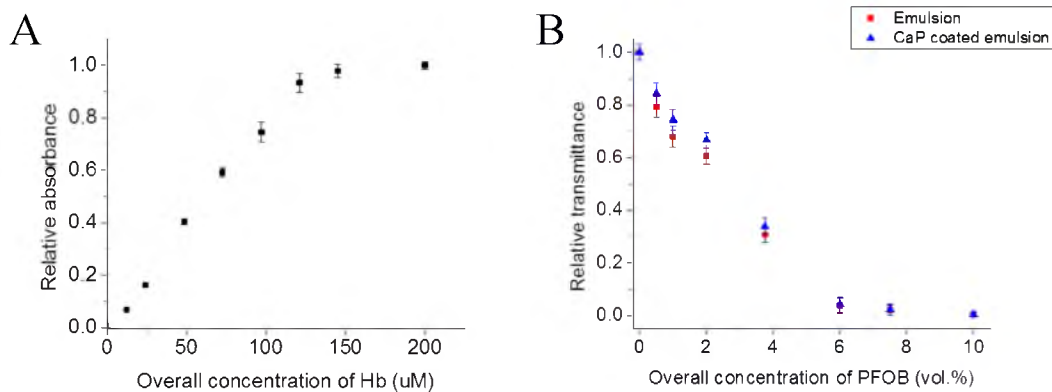
Figure 3-23 Control experiments of the photometer in stopped-flow apparatus: the limitation of relative absorbance and the light scattering due to nanoparticles. A) The relative absorbance of the deoxygenated hemoglobin. This assumed the photometer was limited to 120 uM of Hb to accurately detect the changes due to chemical reaction. B) The relative transmittance of the emulsion (280 nm), and the calcium phosphate coated emulsion (330 nm). The uncoated and the coated emulsion suspensions were measured at 2 vol.% of PFOB to minimize the effects of light scattering.
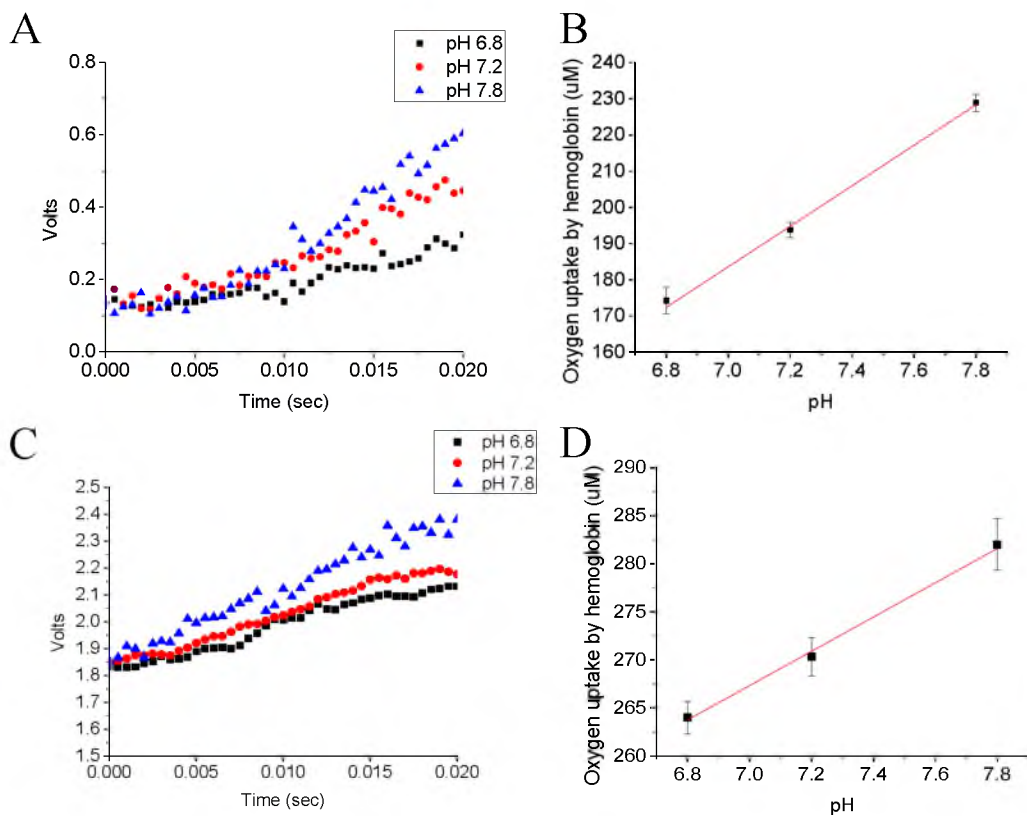
Figure 3-24 The oxygen uptake by deoxy-hemoglobin in water and in water with emulsion at various pHs. A) The oscilloscope trace of transmittance versus time for the Hb in a controlled aqueous environment, as described in section 3.3.2.2.3. The pHs of Hb and water samples were pH 6.8, pH 7.2, and pH 7.8. B) The oxygen uptake by the Hb at various pHs. The transmittance voltage was converted to molar concentration using the method described in Appendix B. C) The oscilloscope trace of transmittance versus time for the Hb in controlled pHs. The uncoated emulsion was mixed with the Hb matching the pHs in both solutions. D) The oxygen uptake by the Hb at various pHs. At pH 7.8, the signal was unstable while the rest of pHs were constantly increased. As (B), the higher pH demonstrated the greater oxygen uptake. However, the standard deviation at pH 7.8 was the greatest while the rest of pHs were constant at 2.
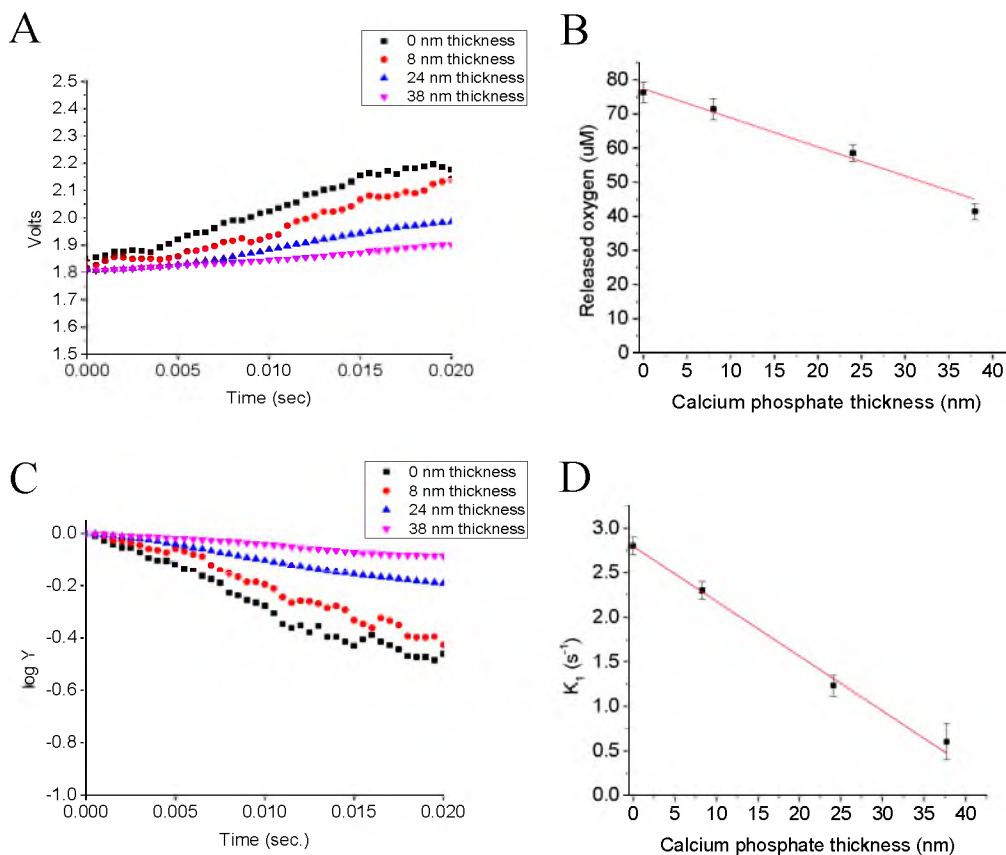
Figure 3-25 The oxygen capacity and release rate from emulsion particles. A) The oscilloscope trace of transmittance in volts versus time for the Hb and the calcium phosphate coated emulsion at pH 7.2. With increasing coating thickness, the Hb was less saturated with oxygen. B) The oxygen uptake by Hb at various coating thickness with the mean and standard deviation taken from five measurements. The transmittance voltage was converted to molar concentration of oxygen uptake by hemoglobin (Appendix B). C) The logarithm of the absorbance versus time for the Hb and CaP emulsion. D) The first order kinetic constant of the oxygen uptake by Hb with the mean and standard deviation taken from five measurements. Increasing the coating layer thickness slowed, and reduced, the amount of oxygen absorbed by hemoglobin.
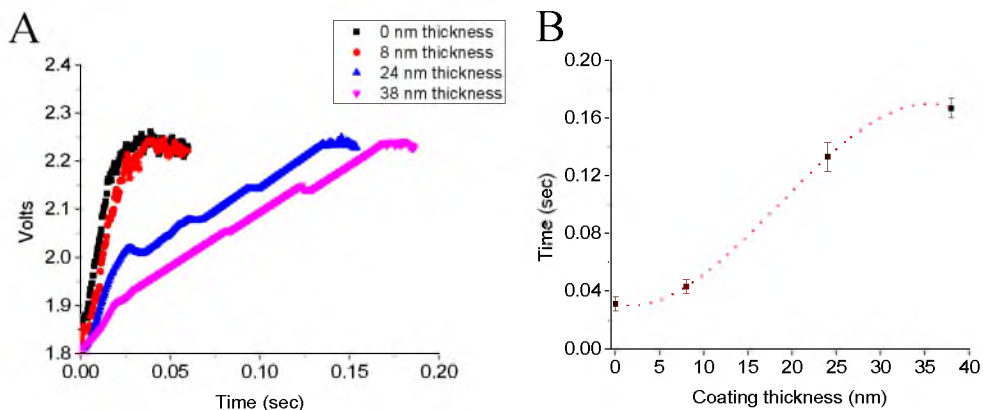
Figure 3-26 The oxygen release time from emulsion particles. A) The transmittance measurement in volts of the calcium phosphate coated emulsion with various thicknesses until it reached equilibrium. B) The amount of time taken for the oxygen release from the samples. The thicker the coating, the longer it took to release oxygen. The amount of oxygen released from the emulsion was 87 uM at 0 nm thickness, 82 uM at 8 nm thickness, 80 uM at 24 nm thickness, and 82 uM at 38 nm thickness following the calculation in Appendix B.
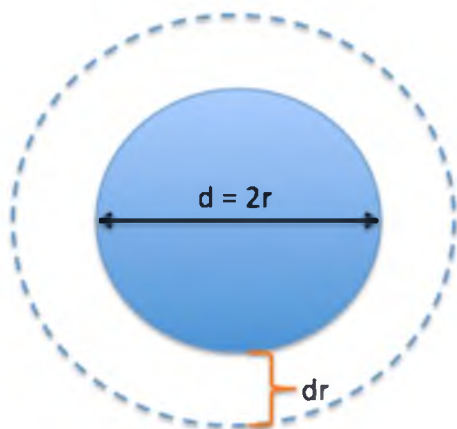
Figure 3-27 A schematic of the eluted drug particle, which demonstrated a change in surface area over time; d is diameter, r is radius, and dr is the change in radius. When time was changed by dt, the amount of drug released was estimated by multiplying the change of radius (dr) and surface area ($4r^2\pi$).
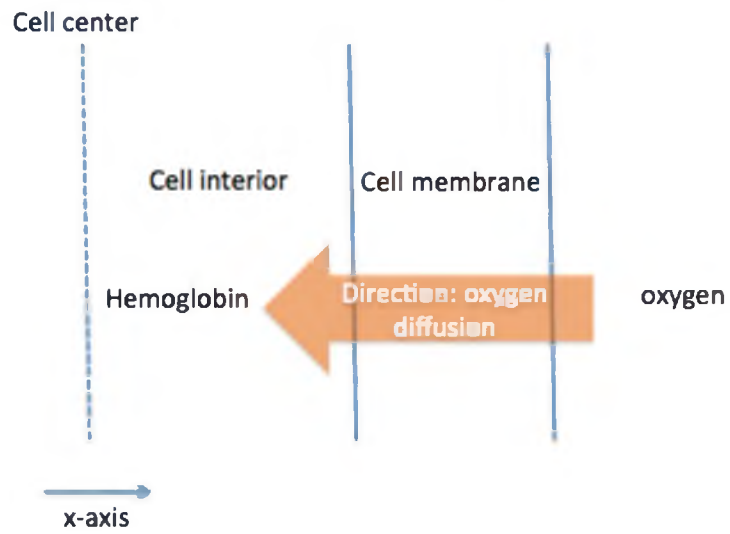
Figure 3-28 The Roughton model for oxygen diffusion in the red blood cell, modified from [204]. The model shows only one side of the cell for simplicity. Oxygen outside of the cell diffused in, then it interacted with the hemoglobin inside [205].

CHAPTER 4

CONCLUSION AND FUTURE WORK

The principle goals of this research were to synthesize a biocompatible emulsion

encapsulated by a calcium phosphate coating in the desired phase, increasing its stability,

while maintaining its function as an oxygen carrier. The emulsion needed to meet the

following criteria in order to be viable:

1) The perfluorooctyle bromide (PFOB)-based emulsion should be in the desired

   phase, such as oil-in-water.

2) The size of the emulsion particles should be synthesized using a reproducible

   procedure.

3) The sized emulsion particles should be coated with a

   biocompatible/biodegradable material such as dicalcium phosphate.

4) The coated emulsion particles should demonstrate the increased stability,

   while maintaining their performance as oxygen carriers.

Chapter 2 described the mapping of the ternary phase diagram using two different types

of surfactants – anionic (1,2 dioleoyl-sn-glycero-3-phosphatidic acid (DOPA)) and

zwitterionic (L-α-phosphatidylcholine (soy lecithin)) – and the constant materials of two

immiscible liquids (oil and water). I hypothesized that the anionic surfactant would have a

smaller region for the oil-in-water phase because the stronger repulsive force between the

head groups of surfactants would require fewer molecules to form particles if both types of surfactants formed the same-sized particle. Generally, visual inspection and shear stress measurements were utilized to identify the phase boundaries. These methods, however, did not yield convincing results. While visual inspection was essential for mapping the diagrams and observing the phase changes in the given materials, more evidence was required to verify the phase boundaries. Therefore, specialized techniques, such as buoyant density, fluorescence quenching, Fourier transform infrared spectroscopy (FT-IR), and cryogenic electron microscopy (cryo-EM), were used to conduct the analysis.

Buoyant density estimated how the oil and water were dispersed and associated in the emulsion. Fluorescence quenching supported and disproved the proposed oil-in-water, water-in-oil, and bicontinuous phases. FT-IR quantitatively determined the amount of oil that was employed to form the emulsion. Finally, cryo-EM was used to observe the morphology of the emulsion in each phase, using images to verify the proposed phase behaviors. I determined the desired region of the oil-in-water (O/W) phase by answering the questions in the flow chart shown in Figure 2-1. The results showed that the ternary phase diagram with soy lecithin had the larger region of O/W phase, thereby supporting the hypothesis. This result was caused by the different packing factor in each surfactant. Since the larger region provides more reliability for producing the desired synthesis experimentally, I selected the diagram with soy lecithin for the calcium phosphate coating.

The three objectives of Chapter 3 were to 1) size the emulsion particle, 2) coat the sized particle with calcium phosphate, and 3) determine the stability and the oxygen release/content. I was not sufficiently able to obtain uniform, dispersed particles using

the fast mixing method. Therefore, I sized the emulsion particles by extruding them through a polymer membrane under constant pressure. The emulsion particles were passed through the membrane seven times in order to ensure that the particles were uniform and dispersed. The emulsion size was reduced from 1 micron to ~280 nm in diameter. The uniform size and dispersion of the particles facilitated the initial experiments for the coating. In order to ensure the optimal dispersion of particles, monitoring the zeta potential performed pH titration. Since the emulsion would be unstable causing it to flocculate, coalesce, or cream if its potential came close to zero millivolts, a well-dispersed emulsion would carry a greater value, either in positive or negative volts. The optimal dispersion was found to be at pH 8.8. Since the soy lecithin molecule was zwitterionic, containing both negative and positive charges, I studied the ionic affinity of the head group by adding calcium and phosphate. The change in zeta potential was 32 times greater with calcium than with phosphate, indicating that the soy lecithin molecule accepted the positive ion from the phosphate group more easily. I also studied the binding coefficient of the calcium ion to the soy lecithin emulsion in order to estimate the amount of the calcium that would be needed for coating using the Hill plot. The results showed that one calcium ion was needed to bind to one soy lecithin molecule. In order to verify the layer-by-layer coating, the zeta potential monitored the change in voltage. When the calcium ion was added to the emulsion system, the potential increased. The potential returned to its initial value when the phosphate ion was added. Using these monitoring techniques, the emulsion particles were coated with calcium phosphate to various thicknesses ranging from 8 nm to 38 nm.

In order to test the stability of the coated emulsion, I performed three types of stability tests on the product: a thermal test using an autoclave, a physical test using a

shaker, and a time test by storing the emulsion. These stability tests could also be conducted during the management of the product prior to injecting it into patients. The coated emulsion showed greater stability than the uncoated one. After all of the tests, the particles of the coated emulsion remained the same size and well-dispersed. I assessed the oxygen release/content of the coated emulsion by using the fast mixing method with a stopped-flow apparatus and hemoglobin. Combining these tools, the oxygen from the particle was measured quickly and accurately. When the thickness of the coating on the emulsion particle was increased, the amount of oxygen released over a given time decreased from 77 uM to 45 uM. I used the Hixson-Crowell cube root law to estimate the diffusion coefficient, which showed the differences between diffusion coefficients for the uncoated and the coated emulsions. The coated emulsion had the lower coefficient, and all of the coated emulsions exhibited constant diffusion coefficients.

In sum, the results of the study proved the hypothesis by demonstrating 1) the fundamental understanding of the emulsion system through the construction of the ternary phase diagram, 2) the coating on the emulsion flexible surface with biocompatible material, and 3) the increased stability and better performance of the emulsion as an oxygen carrier.

Future research will focus on applying the product *in vitro*, testing the stability of the product when it mixes in blood and determining whether circulating the product with blood simulates the blood vessel. The particle size will be monitored for its stability. Another avenue of future research will be to assess the emulsion's degree of separation from the blood. Due to the high density of PFOB, theoretically the product should separate from blood as it circulates in the human body. The results from this study

indicate that the calcium phosphate coated oxygen carrier can be a great future product

that improves upon the stability of current oxygen carrier products.

APPENDIX A

CALCULATION OF ENCAPSULATION OF PFOB BY THE

ABSORBANCE

$$[PFOB] = \frac{Vol_{PFOB}}{Vol_{total}}$$ Eq. A-1

$$ABS_{PFOB\ theoretical} = ABS_{PFOB\ pure} \times [PFOB]$$ Eq. A-2

$$ABS_{PFOB\ true} = ABS_{PFOB\ exp} \times \left(1 - \frac{ABS_{surfactant\ exp}}{ABS_{surfactant\ pure}}\right)$$ Eq. A-3

$$Encapsulation_{PFOB} = \left(\frac{ABS_{PFOB\ true}}{ABS_{PFOB\ theoretical}}\right) \times 100\%$$ Eq. A-4

where [PFOB] indicates the concentration of PFOB in the total volume. The volume of

PFOB is known in the experiment and the total volume is the addition of both PFOB and

water. $ABS_{PFOB\ theoretical}$ represents the expected absorbance from IR if the PFOB is

entirely encapsulated by the emulsion system without the excess liquid. The surfactants,

DOPA and soy lecithin, present the wavenumbers in both 2930 cm^{-1} and 1200 cm^{-1} so

that the measured absorbance of the emulsion demonstrates the surfactant and PFOB at

the same wavenumber. In order to make a correction, the empirical absorbance of PFOB

is subtracted by the surfactant, and the ratio between the pure and experiment surfactant

results in the amount of the surfactant in the PFOB wavenumber. Once the absorbance of

PFOB is corrected by the true absorbance, the actual amount of the encapsulation is

calculated by the ratio between the theoretical and the true absorbance (Eq. A-4).

APPENDIX B

CALCULATION OF CONCENTRATION OF OXYGEN IN

EMULSION SYSTEM

B.1 Calibration Curve of Oxygenated and Deoxygenated Hemoglobin

$$T = \frac{V - V_{min}}{V_{max} - V_{min}}$$ Eq. B-1

$$Abs = -\log(T)$$ Eq. B-2

$$[HbO_2] = a \cdot Abs + b$$ Eq. B-3

where V was the measured voltage of initially oxygenated and deoxygenated

hemoglobins, V_{min} and V_{max} were the voltages at 0% transmittance and 100%

transmittance in the solvent used for the emulsion, Abs was the absorbance, and [HbO$_2$]

was the concentration of oxygenated hemoglobin with constant values (a and b). The

concentration of initially oxygenated hemoglobin was measured by UV-Vis (3.3.2.2.1.2)

at 540 nm, and the [HbO$_2$] for deoxygenated hemoglobin was confirmed by measuring it

with a Clark electrode. Then, the calibration curve of [HbO$_2$] was developed linearly by

knowing these two values due to Beer's law.

B.2 Concentration of Oxygen Uptake by Deoxy-hemoglobin in Solvent

$$T_{measured} = \frac{V_{measured} - V_{min}}{V_{max} - V_{min}} \qquad \text{Eq. B-4}$$

$$Abs_{measured} = -\log(T_{measured}) \qquad \text{Eq. B-5}$$

$$[O_2]_{solvent} = \frac{[HbO_2] \cdot Mw_{Hb} \cdot O_2 \, binding \cdot \rho_{O_2}}{MW_{O_2}} \qquad \text{Eq. B-6}$$

where $V_{measured}$ was the measured voltage of reaction between deoxy-hemoglobin and the solvent used in the emulsion, $T_{measured}$ was the converted transmittance from $V_{measured}$, and $Abs_{measured}$ was the converted absorbance from $T_{measured}$. The concentration of oxygenated hemoglobin ($[HbO_2]$) was estimated by applying $Abs_{measured}$ to Eq. B-3. Once $[HbO_2]$ was estimated from Eq. B-3, it was converted to the oxygen concentration in Eq. B-6. MW and MW_{O_2} were the molecular weight of the hemoglobin (64,500 Da [214]) and the oxygen gas (32 g/mol), O_2 binding was the concentration of the oxygen binding per grams of hemoglobin (1.34 mL O_2/g [133]), and ρ_{O_2} was the density of the oxygen (1.331 kg/m^3).

B.3 Concentration of Oxygen Uptake by Deoxy-hemoglobin from Particle

$$T_{particle} = \frac{V_{particle} - V_{min}}{V_{max} - V_{min}} \qquad \text{Eq. B-7}$$

$$T' = T_{particle} \times C \qquad \text{Eq. B-8}$$

$$Abs' = -\log(T') \qquad \text{Eq. B-9}$$

$$[O_2]_{sample} = \frac{[HbO_2]_{particle} \cdot MW \cdot O_2 binding \cdot \rho_{O_2}}{MW_{O_2}} \qquad \text{Eq. B-10}$$

$$[O_2]_{particle} = [O_2]_{sample} - [O_2]_{solvent} \qquad \text{Eq. B-11}$$

where $V_{particle}$ was the measured voltage of the reaction between deoxy-hemoglobin and

the sample. The transmittance of the reaction was multiplied by the correction factor (C),

which was from Figure 3-19 (B) as a function of concentration. The correction factor was

the inverse of the relative transmittance (T'). Then, the corrected transmittance was

converted to absorbance in Eq. B-9. The estimated absorbance was applied to Eq. B-3 to

find the concentration of the oxygenated hemoglobin. Then, the concentration was

utilized to find the oxygen concentration in the sample solution (Eq. B-10) using the

same values as mentioned in Eq. B-6. In order to obtain the oxygen content by the

particles, the oxygen concentration from the sample was subtracted by the solvent

(Eq. B-11).

APPENDIX C

CALCULATION OF HENRY'S LAW CONSTANT OF PERFLUOROOCTYLE

BROMINE AT ROOM TEMPERATURE

Since the experiment was performed at room temperature (20 °C), the Henry's

law constant of PFOB was converted from 37°C to 20°C using the Van't Hoff equation

[215] as follows:

$$k_H(T_{20°C}) = k_H(T_{37°C}) \cdot e^{\left[C \cdot \left(\frac{1}{T_{20°C}} - \frac{1}{T_{37°C}} \right) \right]}$$

Eq. C-1

where T was temperature in Kelvin, k_H was the Henry's law constant 0.0516 bar·m^3·mol^{-1}

at 37°C [181], and C was the constant in Kelvin. Constant C of oxygen was 1700 [216].

REFERENCES

[1]   A. R. Cross. *Blood Facts and Statistics.* Available:
        http://www.redcrossblood.org/learn-about-blood/blood-facts-and-statistics

[2]   T. Thomas, "The intravenous injection of milk as a substitute for the transfusion
        of blood," *NY State J. Med.,* vol. 27, 1878.

[3]   R. Winslow, "Historical Background," in *Blood Substitutes*, R. Winslow, Ed., ed
        San Diego: Elsevier Academic Press, 2006, p. 6.

[4]   C. Jennings, "The intravenous injection of milk," *Br. Med. J.,* vol. 1, 1885.

[5]   D. Villota, "Equality of the in vivo and in vitro oxygen-binding capacity of
        haemoglobin in patients with severe respiratory disease," *Br. J. Anaesth,* vol. 53,
        1981.

[6]   G. Von Stark, "Die Resorbierbarkeirt des Hamatins und die bedeutung
        hamoglobin-prararate," *Dtsche Med. Wochenschr,* vol. 24, 1898.

[7]   A. Sellards and G. Minot, "Injection of hemoglobin in man and its relation to
        blood destruction, with especial reference to the anemias," *J. Med. Res.,* vol. 34,
        1916.

[8]   H. Bunn and J. Jandl, "The renal handling of hemoglobin," *Trans. Assoc. Am.
        Phys.,* vol. 81, 1968.

[9]   R. Benesch and R. Benesch, "The effect of organic phosphates from the human
        erythrocyte on the allosteric properties of hemoglobin," *Biochem. Biophys. Res.
        Comm.,* vol. 26, 1967.

[10]   R. Benesch, R. Benesch, R. Renthal, and N. Maeda, "Affinity labeling of the
        polyphosphate binding site of hemoglobin," *Biochem.,* vol. 11, 1972.

[11]   S. Rabiner, J. Helbert, H. Lopas, and L. Friedman, "Evaluation of stroma-free
        haemoglobin for use as a plasma expander," *J. Exp. Med.,* vol. 126, 1967.

[12]   F. DeVenuto, H. Friedman, R. Neville, and C. Peck, "Appraisal of hemoglobin
        solution as a blood substitute," *Surg. Gynecol. Obst.,* vol. 149, 1979a.

[13]   F. DeVenuto, A. Zegna, and K. Busse, "Lyophilization of crystalline hemoglobin solution and exchange transfusions with lupophilized, reconstitutes hemoglobin," *Surg. Gynecol. Obst.*, vol. 148, 1979b.

[14]   F. DeVenuto and A. Zegna, "Transfusion with pyridoxalated-polymerized hemoglobin solutions," *Transfusion*, vol. 21, 1981.

[15]   F. DeVenuto and A. Zegna, "Blood exchange with pyridoxalated and polymerized hemoglobin solution," *Surg. Gynecol. Obst.*, vol. 149, 1982.

[16]   F. DeVenuto, "Hemoglobin solutions as oxygen-delivering resuscitation fluids," *Crit. Care Med.*, vol. 10, 1982.

[17]   K. Bonhard, "Experimentelle Erfahrungen mit hamoglobin-infusionslosungen," in *Internationales Symposium uber Struktur and Function der Erythrozyten*, S. Rappaport and F. Jung, Eds., ed Berlin: Akademie-Verlag, 1975a, p. 221.

[18]   K. Bonhard, "Acute oxygen supply by infusion of hemoglobin solutions," *Fed. Proc.*, vol. 34, 1975b.

[19]   J. Payne, "Polymerization of proteins with glutaraldehyde. Soluble molecular-weight markers," *Biochem.*, vol. 135, 1973.

[20]   M. Laver, P. Boysen, and K. Morris, "Water soluble crosslinked polymerised haemoglobin free of stroma used as a blood substitute," US Patent, 1975.

[21]   L. Sehgal, A. Rosen, and S. Gould, "In vitro and in vivo characteristics of polymerized pyridoxylated haemoglobin solution," *Fed. Proc.*, vol. 39, 1979.

[22]   G. Moss, S. Gould, and A. Rosen, "Results of the first clinical trial with a polymerized hemoglobin solution," *Biomat. Adrtif. Cells Artif. Organs*, vol. 17, 1989.

[23]   T. Chang, "30th Anniversary in artificial red blood cell research," *Biomat. Artif. Cells, Artif. Organs*, vol. 16, 1988.

[24]   L. Djordjevich, J. Mayoral, and A. Ivankovich, "Synthetic erythrocytes: cardiorespiratory changes during exchange transfusions," *Anesthesiology*, vol. 63, 1985.

[25]   C. Hunt, R. Burnette, and R. MacGregor, "Synthesis and evaluation of a prototypal artificial red cell," *Science*, vol. 230, 1985.

[26]   A. Rudolph, R. Rabinovici, and G. Feuerstein, *Red blood cell substitutes: Basic principles and clinical applications*. New York: Marcel Dekker, 1998.

[27]   R. Rabinovici, A. Rudolph, and G. Feuerstein, "Characterization of hemodynamic hemotologic, and biochemical responses to administration of liposome-encapsulated hemoglobin in the consciuous, freely moving rat," *Circ. Shock,* vol. 29, 1989.

[28]   R. Winslow, in *Blood Substitute,* R. Winslow, Ed., ed London, UK: Elsevier Academic Press, 2006, p. 304.

[29]   H. Sloviter and T. Kamimoto, "Erythrocyte substi- tutes for perfusion of brain," *Nature,* vol. 216, 1967.

[30]   R. Geyer, R. Monroe, and K. Taylor, "Survival of rats having red cells totally replaced with emulsified fluorocarbon," *Fed. Proc.,* vol. 27, 1968.

[31]   H. Saito and K. Shinoda, "Stability of W/O[water/oil]-type emulsions as a function of temperature and of the hydrophilic chain length of the emulsifier," *Colloid Interface Sci.,* vol. 32, p. 649, 1970.

[32]   A. van Zyl, D. de Wet-Roos, R. Sanderson, and B. Klumperman, "The role of surfactant in controlling particle size and stability in the miniemulsion polymerization of polymeric nanocapsules," *Eur. Poly. J.,* vol. 40, 2004.

[33]   J. Strassner, "Effect of pH on interfacial films and stability of crude oil-water emulsions," *J. Pet. Technol.,* vol. 20, 1968.

[34]   S. Radford, E. Dickinson, and M. Golding, "Stability and rheology of emulsions containing sodium caseinate: combined effects of ionic calcium and alcohol," *J. Colloid Interface Sci.,* vol. 274, 2004.

[35]   C. Peng and Y. Hsu, "Perfluorocarbon-soluble compounds," USA Patent, 2006.

[36]   C. Peng and F. Huang, "Formation of perfluorocarbon microemulsion by fluorinated polyethylene glycol," *J. Disper. Sci. Tech.,* vol. 29, 2008.

[37]   C. Colina and K. Gubbins, "Vapor-liquid and vapor-liquid-liquid equilibria of carbon dioxide/n-perfluoroalkane/n-alkane ternary mixture," *J. Phys. Chem. B,* vol. 109, 2005.

[38]   P. LoNostro, S. Choi, C. Ku, and S. Chen, "Fluorinated microemulsions: a study of the phase behavior and structure," *J. Phy. Chem. B,* vol. 103, 1999.

[39]   R. Aboofazeli, C. Lawrence, S. Wicks, and M. Lawrence, "Investigations into the formation and characterization of phospholipid microemulsions III. Pseudo-ternary phase diagrams of systems containing water-lecithin-isopropyl myristate and either an alkanoic acid, amine, alkanediol, poly ethylene glycol alkyl ether or alcohol as co-surfactant," *Int. J. Pharm.,* vol. 111, 1994.

[40]   J. Lee and K. Lim, "Changes in two-phase emulsion morphology in temperature-amphiphile concentration or fish diagram for ternary amphiphile/oil/water systems," *J. Colloid Interface Sci.*, vol. 290, 2005.

[41]   E. Mahdi, M. Sakeena, M. Abdulkarim, G. Abdullah, M. Sattar, and A. Noor, "Effect of surfactant and surfactant blends on pseudoternary phase diagram behavior of newly synthesized palm kernel oil esters," *Drug Des Devel Ther.*, vol. 5, 2011.

[42]   P. Winsor, "Hydrotropy, solubilization, and related emulsification processes: Part I," *Trans. Faraday Soc.*, vol. 44, p. 376, 1948.

[43]   P. Kumar and K. L. Mittal, *Handbook of Microemulsion Science and Technology*. New York: Marcel Dekker, Inc., 1999.

[44]   D. Belnap, N. Olson, and T. Baker, "A method for establishing the handness of biological macromolecules," *J. Struct. Biol.*, vol. 120, 1997.

[45]   R. Batting and A. Williamson, "Single-pan balance, buoyancy, and gravity or 'a mass of confusion,'" *J. Chem. Ed.*, vol. 61, 1984.

[46]   C. Parker, *Photoluminescenc of Solutions*. New York, NY: Elsevier, 1968.

[47]   P. Technologies. *ATR-Theory and Applications*. Available: http://www.piketech.com/files/pdfs/ATRAN611.pdf

[48]   S. Tenjarla, "Microemulsions: an overview and pharmaceutical applications," *Crit. Rev. Therapeut. Drug Carrier Syst*, vol. 16, 1999.

[49]   B. Park, J. Youm, S. Jeong, E. Choi, S. Ahn, and S. Lee, "The characterization of molecular organization of multilamellar emulsions containing pseudoceramide and type iii synthetic ceramide," *J. Invest. Dermatol.*, vol. 121, 2003.

[50]   T. Tadros, "Emulsion Science and Technology: A General Introduction," in *Emulsion Science and Technology*, T. Tadros, Ed., ed Weinheim: Willey-VCH, 2009.

[51]   J. Sjoblom, "Emulsion Phase Inversion Phenomena," in *Emulsions and Emulsion Stability*. vol. 132, J. Sjoblom, Ed., ed Boca Raton, FL: CRC Press, 2006, p. 218.

[52]   H. Paroor, "Microemulsion: prediction of the phase diagram with a modified Helfrish free energy," Doctor of Philosophy, Polymer Research, Johannes Gutenberg University, Mainz, Germany, 2012.

[53]   K. Lowe, "Perfluorochemicals: blood substitutes and beyond," *Adv. Mater.*, vol. 3, 1991.

[54]   E. Dickinson and M. Golding, "Influence of alcohol on the stability of oil-in water emulsion containing sodium caseinate," *J. Colloid Interface Sci.,* vol. 197, 1998.

[55]   E. Dickinson and M. Golding, "Creaming and flocculation of oil-in-water emulsions containing sodium caseinate," *J. Colloid Interface Sci.,* vol. 185, 1997.

[56]   C. Berli, D. Quemada, and A. Parker, "Modelling the viscosity of depletion flocculated emulsions," *Colloids & Surf. A: Physicochem. Eng. Asp.,* vol. 203, 2002.

[57]   S. S. Davis and D. E. Wotton, "Emulsion of Perfluorocarbons in Aqueous Media," U.S. Patent 4859363, 1989.

[58]   T. E. ToolBox. (2014, 8/25). *Water-Density and Specific Weight.* Available: http://www.engineeringtoolbox.com/water-density-specific-weight-d_595.html

[59]   T. Grubbs. (2014, 6/30). *Fluorescence Lifetimes and Dynamic Quenching.* Available:http://www2.stetson.edu/~wgrubbs/datadriven/quenching/quenchingwtg.html

[60]   Y. Barenholz, T. Cohen, R. Korenstein, and M. Ottolenghi, "Organization and dynamics of pyrene and pyrene lipids in intact lipid bilayers. Photo-induced charge transfer processes," *Biophys. J.,* vol. 60, 1991.

[61]   B. Valeur, *Molecular Fluorescence: Principles and Applications.* New York: Wiley-VCH, 2002.

[62]   W. Reusch. (2014, 7/28). *Infrared Spectroscopy.* Available: http://www2.chemistry.msu.edu/faculty/reusch/VirtTxtJml/Spectrpy/InfraRed/infrared.htm

[63]   D. Larsen. (2014, 6/12). *Infrared: Interpretation.* Available: http://chemwiki.ucdavis.edu/Physical_Chemistry/Spectroscopy/Vibrational_Spectroscopy/Infrared_Spectroscopy/Infrared%3A_Interpretation

[64]   S. Yokoyama, S. Murachima, and T. Watanabe, "Oxygen-Transferable Emulsion," U.S. Patent 3962439, 1976.

[65]   I. R. Schmolka and G. Ile, "Artificial Blood Emulsifiers," U.S. Patent 4395393, 1983.

[66]   P. Becher, *Emulsion: Theory and Practice.* New York: Reinhold, 1965.

[67]   K. Meleson, G. Graves, and T. G. Mason, "Formation of concentrated nanoemulsion by extreme shear," *Soft Mater.,* vol. 2, p. 109, 2004.

[68] R. J. Kaufman and T. J. Richard, "Emulsion of Highly Fluorinated Organic Compounds," U.S. Patent 5350571, 1992.

[69] P. Franco and J. Heine, "Water-thin emulsion formed by high pressure homogenization process," U.S. Patent 5994414 1999.

[70] K. Landfester, F. Tiarks, H. Hentze, and M. Anotonietti, "Polyaddition in miniemulsions: a new route to polymer dispersions," *Macromol. Chem. Phys.*, vol. 201, p. 1, 2000.

[71] H. A. Sloviter, "Process for Preparing Perfluorochemical Emulsion Artificial Blood," U.S. Patent 4497829, 1985.

[72] D. Roth, P. Keipert, N. Faithfull, T. Zuck, and J. Riess, "Use of Synthetic Oxygen Carriers to Facilitate Oxygen Delivery," U.S. Patent 5344393, 1994.

[73] S. Ogawa, E. Decker, and D. McClements, "Production and characterization of O/W emulsions containing cationic droplets stabilized by lecithin-chitosan membranes," *J. Agric. Food Chem.*, vol. 2003, pp. 2806-12, 2003.

[74] K. Shinoda and T. Ogawa, "Solubilization of water in nonaqueous solutions of nonionic surfactants," *Colloid Interface Sci.*, vol. 24, p. 56, 1967.

[75] H. Brinkman, "A calculation of the viscous force exerted by a flowing fluid on a dense swarm of particles," *App. Sci. Res.*, vol. 1, 1949.

[76] D. Papageorgiou, "On the breakup of viscous liquid threads," *Phy. Fluids*, vol. 7, 1995.

[77] L. LizMarzan, M. Giersig, and P. Mulvaney, "Synthesis of nanosized gold-silica core-shell particles," *Langmuir*, vol. 12, 1996.

[78] L. LizMarzan, M. Giersig, and P. Mulvaney, "Homogeneous silica coating of vitreophobic colloids," *Chemical Comm.*, vol. 6, 1996.

[79] T. Ung, L. LizMarzan, and P. Mulvaney, "Redox catalysis using Ag@SiO2 colloids," *J. Phys. Chem. B*, vol. 103, 1999.

[80] S. Kim, D. Bae, H. Shin, and K. Hong, "Optical absorption behaviour of platinum core-silica shell nanoparticle layer and its influence on the reflection spectra of a multi-layer coating system in the visible spectrum range," *J. Phys. Conden. Matter*, vol. 16, 2004.

[81] G. Wang and A. Harrison, "Preparation of iron particles coated with silica," *J. Colloid Interface Sci.*, vol. 217, 1999.

[82] Y. Lu, Y. Yin, B. Mayers, and Y. Xia, "Modifying the surface properties of superparamagnetic iron oxide nanoparticles through a sol-gel approach," *Nano Lett.*, vol. 2, 2002.

[83] J. Spatz, A. Roescher, S. Shieiko, G. Krausch, and M. Moller, "Noble-metal loaded block ionomers - micelle organization, adsorption of free chains and formation of thin-films," *Adv. Mater.*, vol. 7, 1995.

[84] J. Deng, X. Ding, W. Zhang, Y. Peng, J. Wang, X. Long, *et al.*, "Magnetic and conducting Fe3O4-cross-linked polyaniline nanoparticles with core-shell structure," *Polymer*, vol. 43, 2002.

[85] D. Hubert, M. Jung, P. Frederik, P. Bomans, J. Meuldijk, and A. German, "Vesicle-directed growth of silica," *Adv. Mater.*, vol. 12, 2000.

[86] D. Hubert, M. Jung, and A. German, "Vesicle templating," *Adv. Mater.*, vol. 12, 2000.

[87] S. Begu, S. Girod, D. Lerner, N. Jardiller, C. Tourne-Peteilh, and J. Devoisselle, "Characteriazation of a phospholipid bilayer entrapped into non-porous silica nanoshperes," *J. Mater. Chem.*, vol. 14, 2004.

[88] P. Tanev and T. Pinnavaia, "Biomimetic templating of porous lamellar silicas by vesicular surfactant assemblies," *Science*, vol. 271, 1996.

[89] T. Pedley, *The Fluid Mechanics of Large Blood Vessels* vol. 1. New York: Cambridge University Press, 1980.

[90] N. Resnick, H. Yahav, A. Shay-Salit, S. Schubert, and L. Ziberman, "Fluid shear stress and the vascular endothelium: for better and for worse," *Preg. Biophys. Mol. Bio.*, vol. 81, 2003.

[91] M. Zamir, "Shear forces and blood vessel radii in the cardiovascular system," *J. Gen. Physiol.*, vol. 69, 1977.

[92] Y. Fung and S. Liu, "Elementary mechanics of the endothelium of blood vessels," *J. Biomech. Eng.*, vol. 115, 1993.

[93] T. Ziegler and R. Nerem, "Tissue engineering a blood vessel: regulation of vascular biology by mechanical stresses," *J. Cell. Biochem.*, vol. 56, 1994.

[94] K. Keller, "Effect of fluid shear on mass transport in flowing blood," *Fed. Proc.*, 1971.

[95] F. Akbarian, A. Lin, B. Dunn, J. Valentine, and J. Zink, "Spectroscopic determination of cholinesterase activity and inhibition in sol-gel media," *J. Sol-Gel Sci. Tech.*, vol. 8, 1997.

[96]   C. Radloff and N. Halas, "Enhanced thermal stability of silica-encapsulated metal nanoshells," *App. Phys. Lett.*, vol. 79, 2001.

[97]   J. Patarin, B. Lebeau, and R. Zana, "Recent advances in the formation mechanisms of organized mesoporous materials," *Curr. Op. Coll. Inter. Sci.*, vol. 7, 2002.

[98]   R. Rioux, H. Song, J. Hoefelmeyer, P. Yang, and G. Somorjai, "High- surface-area catalyst design: synthesis, characterization, and reaction studies of platinum nanoparticles in mesoporous SBA-15 silica," *J. Phy. Chem. B,* vol. 109, 2005.

[99]   D. Shephard, T. Maschmeyer, B. Johnson, J. Thomas, G. Sankar, D. Ozkaya, *et al.,* "Bimetallic nanoparticle catalysts anchored inside mesoporous silica," *Angewandte Chemie-Inter. Ed. English,* vol. 36, 1997.

[100]   H. Lang and B. Chandler, "Silica supported bimetallic platinum-gold nanoparticle catalysts from dendrimer mediated route," *Abs. Papers Am. Chem. Soc.,* vol. 228, 2004.

[101]   B. Scott, G. Wirnsberger, and G. Stucky, "Mesoporous and mesostructured materials for optical applications," *Chem. Mater.,* vol. 13, 2001.

[102]   S. Santra, D. Dutta, and B. Moudgil, "Functional dye-doped silica nanoparticles for bioimaging, diagnostics and therapeutics," *Food Biopro. Pro.,* vol. 83, 2005.

[103]   R. Naik, M. Tomczak, H. Luckarift, J. Spain, and M. Stone, "Entrapment of enzymes and nanoparticles using biomimetically synthesized silica," *Chem. Comm.,* vol. 15, p. 1684, 2004.

[104]   Y. Itoh, M. Matsusaki, T. Kida, and M. Askashi, "Preparation of biodegradable hollow nanocapsules by silica template method," *Chem. Lett.,* vol. 33, 2004.

[105]   H. Yang, S. Zhang, X. Chen, Z. Zhuang, J. Xu, and X. Wang, "Magnetite-containing spherical silica nanoparticles for biocatalysis and bioseparations," *Analy. Chem.,* vol. 76, 2004.

[106]   D. Bharali, I. Klejbor, E. Stachowiak, P. Dutta, I. Roy, N. Kaur, *et al.,* "Organically modified silica nanoparticles: a nonviral vector for in vivo gene delivery and expression in the brain," *Proc. Nat. Acad. Sci.,* vol. 102, 2005.

[107]   M. Kumar, M. Smati, S. Mohapatra, X. Kong, R. Lockey, U. Bakowsky, *et al.,* "Cationic silica nanoparticles as gene carriers: synthesis, characterization and transfection efficiency in vitro and in vivo," *J. Nanosci. Nanotech.,* vol. 4, 2004.

[108]   X. Kong, C. Kan, H. Li, D. Yu, and Q. Yuan, "Synthesis and characterization of hollow polymer latex particles," *Poly. Adv. Tech.,* vol. 8, 1997.

[109] M. Fleming, T. Mandal, and D. Walt, "Nanosphere-microsphere assembly: methods for core-shell materials preparation," *Chem. Mater.,* vol. 13, 2001.

[110] S. Marinakos, M. Anderson, J. Ryan, L. Martin, and D. Feldheim, "Encapsulation, permeability, and cellular uptake characteristics of hollow nanometer-sized conductive polymer capsules," *J. Phy. Chem. B,* vol. 105, 2001.

[111] S. Marinakos, J. Novak, L. Brousseau, A. House, E. Edeki, J. Feldaus, *et al.,* "Gold particles as templates for the synthesis of hollow polymer capsules. Control of capsule dimensions and guest encapsulation," *J. Am. Chem. Soc.,* vol. 121, 1999.

[112] M. Wu, S. O'Neil, L. Brousseau, W. McConnell, D. Shultz, R. Linderman, *et al.,* "Synthesis of nanometer-sized hollow polymer capsules from alkanethiol-coated gold particles," *Chem. Comm.,* vol. 9, 2000.

[113] X. Tong, T. Tang, N. Zhu, Z. Feng, and B. Huang, "Preparation of polymer/silica nanoscale hybrids through sol-gel method involving emulsion polymers (PMMA/SiO2)," *Chem. J. Chin. Univ. Chin.,* vol. 23, 2002.

[114] B. Roy, M. Fazal, A. Arruda, S. Malik, and A. Campiglia, "Polymerized fluorescent liposomes incorporating lanthanide ions," *Org. Lett.,* vol. 2, 2000.

[115] J. Hotz and W. Meier, "Vesicle-templated polymer hollow spheres," *Langmuir,* vol. 14, 1998.

[116] S. Ramesh, C. Tan, I. Sopyan, M. Hamdi, and W. Teng, "Consolidation of nanocrystalline hydroxyapatite powder," *Sci. Techniol. Adv. Mater.,* vol. 8, 2007.

[117] T. Guda, M. Appleford, S. Oh, and J. Ong, "A cellular perspective to bioceramic scaffolds for bone tissue engineering: the state of the art.," *Curr. Topics Med. Chem.,* vol. 8, 2008.

[118] K. Schrodter, G. Bettermann, T. Staffel, F. Wahl, T. Klein, and T. Hofmann, "Phosphoric Acid and Phosphates," in *Ullmann's Encyclopedia of Industrial Chemistry,* K. Schrodter, G. Bettermann, T. Staffel, F. Wahl, T. Klein, and T. Hofmann, Eds., ed Weinheim: Wiley-VCH, 2008.

[119] C. Andres, V. Sinani, D. Lee, Y. Gun'ko, and N. Kotov, "Anisotropic calcium phosphate nanoparticles coated with 2-carboxyethylphosphonic acid," *J. Mater. Chem.,* vol. 16, 2006.

[120] H. Schmidt and A. Ostafin, "Liposome directed growth of calcium phosphate nanoshells," *Adv. Mater.,* vol. 14, 2002.

[121] H. Schmidt, B. Gray, P. Wingert, and A. Ostafin, "Assembly of aqueous-cored calcium phosphate nanoparticles for drug delivery," *Chem. Mater.,* vol. 16, 2004.

[122] W. Tjandra, P. Ravi, J. Yao, and K. Tam, "Synthesis of hollow spherical calcium phosphate nanoparticles using polymeric nanotemplates," *Nanotechnology,* vol. 17, 2006.

[123] S. Sadasivan, D. Khushalani, and S. Mann, "Synthesis of calcium phosphate nanofilaments in reverse micelles," *Chem. Mater.,* vol. 17, 2005.

[124] C. Coppel, "Factors causing emulsion upsets in surface facilities following acid stimulation," *J. Pet. Technol.,* vol. 27, 1975.

[125] S. Ali, C. Durham, and E. Elphingstone, "Test identifies acidizing fluid/crude compatibility problems," *Oil & Gas J.,* vol. 19, 1994.

[126] E. Moore, C. Crowe, and A. Hendrickson, "Formation, effect and prevention of asphaltene sludges during stimulation treatments," *J. Pet. Technol.,* vol. 19, 1965.

[127] Malvern. (2014, 6/1). *Emulsions and Predicting the Stability of Emulsions Using Particle Size Analysis and Zeta Potential Using Equipment From Malvern Instruments.* Available: http://www.azonano.com/article.aspx?ArticleID=1213 - _The_Importance_of

[128] Orion, *User Guide Calcium Ion Selective Electrode,* T. Scientific, Ed., ed. Waltham, MA: Thermo Scientific, 2013.

[129] A. Hill, "The possible effects of the aggregation of the molecules of haemoglobin on its dissociation curves," *J. Physiol.,* vol. 40, 1910.

[130] H. Saroff and A. Minton, "The Hill plot and the energy of interaction in hemoglobin," *Science,* vol. 175, 1972.

[131] K. Imai and T. Yonetani, "PH dependence of the Adair constants of human hemoglobin. Nonuniform contribution of successive oxygen bindings to the alkaline Bohr effect," *J. Biol. Chem.,* vol. 250, 1975.

[132] I. Tyuma, K. Shimizu, and K. Imai, "Effect of 2,3-diphosphoglycerate on the cooperativity in oxygen binding of human adult hemoglobin," *Biochem. Biophys. Res. Comm.,* vol. 43, 1971.

[133] E. Dominguez de Villota, M. Ruiz Carmona, J. Rubio, and S. de Andres, "Equality of the in vivo and in vitro oxygen-binding capacity of haemoglobin in patients with severe respiratory disease," *Br. J. Anaesth,* vol. 53, 1981.

[134] C. Chang and T. Traylor, "Kinetics of oxygen and carbon monoxide binding to synthetic analogs of the myglobin and hemoglobin active sites," *Proc. Nat. Acad. Sci.,* vol. 72, 1975.

[135] ChemSpider. (2014, 6/30). *Cetyltrimethylammonium Bromide*. Available: http://www.chemspider.com/Chemical-Structure.5754html

[136] ChemSpider. (2014, 6/30). *Sodium Dodecyl Sulfate*. Available: http://www.chemspider.com/Chemical-Structure.8677.html?rid=260f37dd-7db2-416d-8253-62783b953fc3

[137] ChemSpider. (2014, 6/30). *20-(4-(1,1,3,3-Tetramethylbutyl)Phenoxy)-3,6,9,12,15,18-Hexaoxaicosan-1-ol*. Available: http://www.chemspider.com/Chemical-Structure.68144.html

[138] ChemSpider. (2014, 6/30). *1-Palmitoyl-2-Oleoyl-Sn-Glycero-3-Phosphocholine*. Available: http://www.chemspider.com/Chemical-Structure.4593686.html

[139] S. Dorozhkin, "Calcium orthophosphates as bioceramics: state of the art," *J. Func. Biomater.*, vol. 1, 2010.

[140] S. Salgin, U. Salgin, and S. Bahadir, "Zeta potentials and isoelectric points of biomolecules: the effects of ion types and ionic strength," *Int. J. Electrochem. Sci.*, vol. 7, 2012.

[141] P. Co. (2014, 6/19). *Introduction to Tangential Flow Filtration for Laboratory and Process Development Applications*. Available: http://www.pall.com/main/laboratory/literature-library-details.page?id=34212

[142] W. Royer Jr., "High-resolution crystallographic analysis of co-operative dimeric hemoglobin," *J. Mol. Biol.*, vol. 235, 1994.

[143] W. Caughey, "Heme A of cytochrome c oxidase structure and properties: comparison with heme B, C, and S and derivatives," *J. Biol. Chem.*, vol. 250, 1975.

[144] A. Bellelli. (2014, 6/30). *Medicine and Surgery: Course of Laboratory Medicine Chemical and Biochemical Methods*. Available: http://biochimica.bio.uniroma1.it/didattica/Fcourse/L02_Methods/LabMed.htm

[145] S. Mandal and S. S. Mandal, "Microemulsion drug delivery system: a platform for improving dissolution rate of poorly water soluble drug," *Int. J. Pharm. Sci. Nanotechnol.*, vol. 3, 2011.

[146] C. Anjali, M. Dash, N. Chandrasekaran, and A. Mukherjee, "Anti bacterial activity of sunflower oil microemulsion," *Int. J. Pharm. Sci. Nanotechnol.*, vol. 2, 2010.

[147] B. P. a. C. Education. (2014, 8/15). *How to Calculate Air Density*. Available: https://http://www.brisbanehotairballooning.com.au/faqs/education/116-calculate-air-density.html

[148] K. Kalyanasundaram, "Pyrene fluorescence as a probe of fluorocarbon micelles and their mixed micelles with hydrocarbon surfactants," *Langmuir*, vol. 4, 1988.

[149] O. M. L. Center. (2014, 3/25). *Pyrene*. Available: http://chemwiki.ucdavis.edu/ Analytical_Chemistry/Analytical_Chemistry_2.0/10_Spectroscopic_Methods/10F %3A_Photoluminescence_Spectroscopy

[150] P. Technologies. (2014, 4/12). *Product Data: MIRacle ATR - Fast and Easy IR Sampling*. Available: http://www.piketech.com/files/pdfs/MIRaclePDS1213.pdf

[151] N. Niknafs, R. Hancocks, and I. Norton, "Measurement Techniques Applicable to the Investigation of Emulsion Formation During Processing," in *Emulsion Formation and Stability*, T. Tadros, Ed., ed Weinheim, Germany: Wiley-VCH.

[152] P. Sherman, "Viscosity of emulsion," *Rheologia Acta*, vol. 2, 1962.

[153] F. Nielloud and G. Marti-Mestres, "Formulation Concepts for the EMulsion Maker," in *Pharmaceutical Emulsions and Suspensions*, F. Nielloud and G. Marti-Mestres, Eds., ed New York: Marcel Dekker, Inc., 2000, p. 31.

[154] P. Winsor, *Solvent properties of Amphiphilic compounds*. London, UK: Butterworth, 1954.

[155] W. Switzer. (2014, 3/18). *Density of Water Vapor Pressure of Water*. Available: http://www.ncsu.edu/chemistry/resource/H2Odensity_vp.html

[156] K. Klein, "Liquid Crystals and Emulsions: A Wonderful Marriage," in *Skin Barrier: Chemistry of Delivery Systems*, J. Wiechers, Ed., ed Carol Stream, IL: Allured Publishing Co., 2008.

[157] F. Theiss, D. Apelt, B. Brand, A. Kutter, K. Zlinszky, M. Bohner, *et al.*, "Biocompatibility and resorption of a brushite calcium phosphate cement," *Biomater.*, vol. 26, 2005.

[158] Y. Yoshimine, A. Akamine, M. Mukai, K. Maeda, M. Matsukura, Y. Kimura, *et al.*, "Biocompatibility of tetracalcium phosphate cement when used as a bone substitute," *Biomater.*, vol. 14, 1993.

[159] O. Schneider, D. Mohn, R. Fuhrer, K. Klein, K. Kämpf, K. Nuss, *et al.*, "Biocompatibility and bone formation of flexible, cotton wool-like PLGA/calcium phosphate nanocomposites in sheep," *The Open Orthop. J.*, vol. 5, 2011.

[160] J. Shaikh, D. Ankola, V. Beniwal, D. Singh, and M. Kumar, "Nanoparticle encapsulation improves oral bioavailability of curcumin by at least 9-fold when compared to curcumin administered with piperine as absorption enhancer," *Eur. J. Pharm. Sci.*, vol. 37, 2009.

[161] Y. Wang, R. Dave, and R. Pfeffer, "Polymer coating/encapsulation of nanoparticles using a supercritical anti-solvent process," *J. of Supercritical Fluids,* vol. 28, 2004.

[162] R. Balasubramanian, Y. Kwon, and A. Wei, "Encapsulation and functionalization of nanoparticles in crosslinked resorcinarene shells," *J. Mater. Chem.,* vol. 17, 2007.

[163] P. Pantazis, K. Dimas, J. Wyche, S. Anant, C. Houchen, J. Panyam, *et al.,* "Preparation of siRNA-encapsulated plga nanoparticles for sustained release of sirna and evaluation of encapsulation efficiency," *Nanopart. Bio. Med.,* vol. 906, p. 311, 2012.

[164] M. Aslam, F. Li, and V. Dravid, "Silica encapsulation and magnetic properties of FePt nanoparticles," *J. Colloid Interface Sci.,* vol. 290, 2005.

[165] S. Chae, H. Kim, H. Lee, C. Rhee, and K. Seo, "Calcium phosphate artificial bone as osteoconductive and biodegradable bone substitute material," S. Korea Patent, 2001.

[166] M. Ginebra, C. Canal, M. Espanol, D. Pastorino, and E. Montufar, "Calcium phosphate cements as drug delivery materials," *Adv. Drug Deliv. Rev.,* vol. 64, 2012.

[167] W. Jun, L. Lin, C. Yurong, and Y. Juming, "Recent advances of calcium phosphate nanoparticles for controlled drug delivery," *Mini. Rev. Med. Chem.,* vol. 13, 2013.

[168] X. Cheng and L. Kuhn, "Chemotherapy drug delivery from calcium phosphate nanoparticles," *Int. J. Nanomed.,* vol. 2, 2007.

[169] M. Otsuka, Y. Nakahigashi, Y. Matsuda, J. Fox, W. Higuchi, and Y. Sugiyama, "A novel skeletal drug delivery system using self-setting calcium phosphate cement VIII: the relationship between in vitro and in vivo drug release from indomethacin-containing cement," *J. Control. Release,* vol. 43, 1997.

[170] S. Sasikumar, "Effect of particle size of calcium phosphate based bioceramic drug delivery carrier on the release kinetics of ciprofloxacin hydrochloride: an in vitro study," *Frontriers of Mater. Sci.,* vol. 7, 2013.

[171] V. Patel, "Synthesis of calcium carbonate-coated emulsion droplets for drug detoxification," Master of Science, Department of Materials Science and Engineering, University of Florida, Gainesville, FL, 2002.

[172] C. Buzea, I. Pacheco, and K. Robbie, "Nanomaterials and nanoparticles: sources and toxicity," *Biointerphases,* vol. 2, 2007.

[173] I. Linkov, F. Kyle, and M. Lisa, "Nanotoxicology and nanomedicine: making hard decisions," *Nanomedicine,* vol. 2, 2008.

[174] H. Meng, Z. Chen, G. Xing, H. Yuan, C. Chen, F. Zhao, *et al.,* "Ultrahigh reactivity provokes nanotoxicity: explanation of oral toxicity of nano-copper particle," *Toxicol. Lett.,* vol. 175, 2007.

[175] Y. Xie, Y. Chen, M. Sun, and Q. Ping, "A mini review of biodegradable calcium phosphate nanoparticles for gene delivery," *Curr. Pharm. Biotechnol.,* vol. 14, 2014.

[176] M. Serlachius, K. Zhang, and L. Andersson, "Stanniocalcin in termially differentiated mammalian cells," *Peptides,* vol. 25, 2004.

[177] H. Patel, H. Patel, N. Patel, and A. Gupta, "Calcium phosphate coated liposomes: a novel approach for drug targeting," *Inter. J. Pharm. Res. Bio-Sci.,* vol. 16, 2013.

[178] D. Gabizon, A. Goren, D. Horowitz, A. Tzemach, and T. Siegal, "Long-circulating liposomes for drug delivery in cancer therapy: a review of biodistribution studies in tumor-bearing animals," *Adv. Drug Deliv. Rev.,* vol. 24, 1997.

[179] H. Schmidt and A. Ostafin, "Liposome directed growth of calcium phosphate nanoshell," *Adv. Mater.,* vol. 14, 2002.

[180] J. Vasir and V. Labhasetwar, "Targeted drug delivery in cancer therapy," *Tech. Cancer Res. Treat.,* vol. 4, 2005.

[181] F. Moolman, "Mass Transfer Considerations," in *Oxygen Carriers for a Novel Bio-artificial Liver Support System,* F. Moolman, Ed., ed Germany: Verlag Dr. Muller, 2003, p. 130.

[182] S. Bouwer, L. Hoofd, and F. Kreuzer, "Reaction rates of oxygen with hemoglobin measured by non-equilibrium facilitated oxygen diffusion through hemoglobin solutions," *Biochem. Biophys. Acta.,* vol. 1525, 2001.

[183] G. Ilgenfritz and M. Schuster, "Kinetics of oxygen binding to human hemoglobin: temperature jump relaxation studies," *J. Bio. Chem.,* 1974.

[184] K. Keller and S. Friedlander, "The steady-state transport of oxygen through hemoglobin solutions," *J. Gen. Physiol.,* vol. 49, 1966.

[185] H. Kutchai, J. Jacquez, and F. Mather, "Nonequilibrium facilitated oxygen transport in hemoglobin solution," *Biophys. J.,* vol. 10, 1970.

[186] J. Wittenberg, "The molecular mechanism of hemoglobin-facilitated oxygen diffusion," *J. Bio. Chem.,* 1966.

[187] A. Cupane. (2014, 8/22). *Table of Extinction Coefficients*. Available: http://www.fisica.unipa.it/~emoglobina/epsilon.html

[188] H. White. (2014, 5/22). *Concerning a Biologically Important Relationship-The Influence of the Carbon Dioxide Content of Blood on its Oxygen Binding*. Available: http://www.udel.edu/chem/white/C342/Bohr%281904%29.html

[189] E. Lee, K. Suhr, J. Lee, J. Park, C. Jin, J. Youm, *et al.*, "The clinical efficacy of multi-lamellar emulsion containing pseudoceramide in childhood atopic dermatitis: an open crossover study," *Annal Dermatol,* vol. 15, 2003.

[190] S. Friberg, "Micelles, microemulsions, liquid-crystals, and the structure of stratum–corneum lipids," *J. Soc. Cosmet. Chem.* , vol. 41, 1990.

[191] A. Liu, "Acid-base Equilibria Between the Lipid Membrane and Electrolyte Solution," in *Advances in Planar Lipid Bilayers and Liposomes*, vol. 3, A. Liu, Ed., ed San Diego, CA: Elsevier, 2006, p. 180.

[192] A. Pullman, J. Jortner, and B. Pullman, *Biomolecular Structures and Mechanism*. Netherlans: Kluwer Academic Publishers, 1994.

[193] D. Lide, *CRC Handbook of Chemistry and Physics*. Boca Raton, FL: Chemical Rubber Co., 1999.

[194] dellamary.angelfire.com. (2014, 5/14). *Perfluorooctylbromide*. Available: http://dellamary.angelfire.com/pfob.htm

[195] convertunits.com. (2014, 5/14). *Molecular Weight of Calcium Phosphate*. Available: http://www.convertunits.com/molarmass/Calcium+Phosphate

[196] webmineral.com. (2014, 5/14). *Brushite Mineral Data*. Available: http://webmineral.com/data/Brushite.shtml - .U3MCXV54E0g

[197] C. Zimmer. (2013, 7/12). *Earth's Oxygen: A Mystery Easy to Take for Granted*. Available: http://www.nytimes.com/2013/10/03/science/earths-oxygen-a-mystery-easy-to-take-for-granted.html?_r=0

[198] B. Rubin and C. Lawrence, "The solubility of gases in liquids," *Chemical Rev.,* vol. 66, 1966.

[199] INPHAZE. (2014, 3/21). *High Resolution Characterisation*. Available: http://www.inphaze.com/pubs/INPHAZE_LBLApp_RevB_4pages.pdf

[200] P. Atkins, *Physical Chemistry*. New York, NY: Freeman, 1998.

[201] D. Brogioli and A. Vailati, "Diffusive mass transfer by nonequilibrium fluctuations: Fick's law revisited," *Phys, Rev. E,* vol. 63, 2001.

[202] A. Maton, J. Hopkins, S. JOhnson, D. LaHart, M. Warner, and J. Wright, *Cells Building Blocks of Life*. New Jersey: Prentice Hall, 1997.

[203] B. Mahat, "Mathematical models used in the drug release studies," Master, Pharmacy, Kathmandu University, Dhulikhel, Nepal, 2009.

[204] F. Roughton, "Diffusion and simultaneous chemical reaction velocity in hemoglobin solutions and red cell suspensions," *Prog. Biophys. Biochem.*, vol. 9, 1959.

[205] H. Mizukami and S. Rice, "Transient effects on the initial rate of oxygenation of red blood cells," *Bull. Math. Biol.*, vol. 44, 1982.

[206] S. Fischkoff and J. Vanderkooi, "Oxygen diffusion in biological and artificial membranes determined by the fluorochrome pyrene," *J. Gen. Physiol.*, vol. 65, 1975.

[207] E. Cussler, *Diffusion: Mass Transfer in Fluid Systems*. Cambridge, England: Cambridge University Press, 1997.

[208] F. Moolman, H. Rolfes, A. van der Merwe, and W. CFocke, "Optimization of perfluorocarbon emulsion properties for enhancing oxygen mass transfer in a bio-artificial liver support system," *Biochem. Eng. J.*, vol. 19, 2004.

[209] Aminco-Morrow, *Manual of Aminco-Morrow Stopped-Flow Apparatus*, Aminco-Morrow, Ed., ed. Mountain View, CA, 1973.

[210] P. Ahlstrom and H. Berendsen, "A molecular dynamics study of lecithin monolayers," *J. Phys. Chem.*, vol. 97, 1993.

[211] A. Robinson, W. Richards, P. Thomas, and M. Hann, "Head group and chain behavior in biological membranes: a molecular dinamics computer simulation," *Biophys. J.*, vol. 67, 1994.

[212] R. Morison and R. Boyd, *Organic Chemistry*, 3rd ed. Boston, MA: Allyn and Bacon, Inc., 1985.

[213] C. Stace, *A Guide to Subcellular Botany*. London, UK: Creen & Co. Ltd., 1965.

[214] F. Gutter, H. Sober, and E. Peterson, "The effect of mercaptoethanol and urea on the molecular weight of hemoglobin," *Arch. Biochem. Biophys.*, vol. 62, 1956.

[215] F. Smith and A. Harvey. (2014, 5/22). Avoid common pitfalls when using Henry's law. *Environmental Management*. Available: http://www.chemengr.ucsb.edu/~ceweb/courses/che128/pdf/090733 Avoid Common Pitfalls.pdf

[216]   R. Sander. (2014, 5/22). *Henry's Law Constants (Solubilities).* Available: http://www.henrys-law.org